Synthesis and Manipulation of Semiconductor Nanocrystals in Microfluidic Reactors

by

Emory Ming-Yue Chan

B. S. (Stanford University) 2000

A dissertation submitted in partial satisfaction of
the requirements for the degree of

Doctor of Philosophy

in

Chemistry

in the

GRADUATE DIVISION

of the

UNIVERSITY OF CALIFORNIA, BERKELEY

Committee in charge:

Professor A. Paul Alivisatos, Chair
Professor Richard Mathies
Professor Luke Lee

Fall 2006

The dissertation of Emory Ming-Yue Chan is approved:

Chair	Date
	Date
	Date

University of California, Berkeley

Fall 2006

Synthesis and Manipulation of Semiconductor Nanocrystals in Microfluidic Reactors

by

Emory Ming-Yue Chan

ABSTRACT

Synthesis and Manipulation of Semiconductor Nanocrystals in Microfluidic Reactors

by

Emory Ming-Yue Chan

Doctor of Philosophy in Chemistry

University of California, Berkeley

Professor A. Paul Alivisatos, Chair

Microfluidic reactors are investigated as a mechanism to control the growth of semiconductor nanocrystals and characterize the structural evolution of colloidal quantum dots. Due to their short diffusion lengths, low thermal masses, and predictable fluid dynamics, microfluidic devices can be used to quickly and reproducibly alter reaction conditions such as concentration, temperature, and reaction time, while allowing for rapid reagent mixing and product characterization. These features are particularly useful for colloidal nanocrystal reactions, which scale poorly and are difficult to control and characterize in bulk fluids.

To demonstrate the capabilities of nanoparticle microreactors, a size series of spherical CdSe nanocrystals was synthesized at high temperature in a continuous-flow, microfabricated glass reactor. Nanocrystal diameters are reproducibly controlled by systematically altering reaction parameters such as the temperature, concentration, and reaction time. Microreactors with finer control over temperature and reagent mixing were designed to synthesize nanoparticles of different shapes, such as rods, tetrapods, and hollow shells.

The two major challenges observed with continuous flow reactors are the deposition of particles on channel walls and the broad distribution of residence times that result from laminar flow. To alleviate these problems, I designed and fabricated liquid-liquid segmented flow microreactors in which the reaction precursors are encapsulated in flowing droplets suspended in an immiscible carrier fluid. The synthesis of CdSe nanocrystals in such microreactors exhibited reduced deposition and residence time distributions while enabling the rapid screening a series of samples isolated in nL droplets.

Microfluidic reactors were also designed to modify the composition of existing nanocrystals and characterize the kinetics of such reactions. The millisecond kinetics of the CdSe-to-Ag_2Se nanocrystal cation exchange reaction are measured *in situ* with micro-X-ray Absorption Spectroscopy in silicon microreactors specifically designed for rapid mixing and time-resolved X-ray spectroscopy.

These results demonstrate that microreactors are valuable for controlling and characterizing a wide range of reactions in nL volumes even when nanoscale particles, high temperatures, caustic reagents, and rapid time scales are involved. These experiments provide the foundation for future microfluidic investigations into the mechanisms of nanocrystal growth, crystal phase evolution, and heterostructure assembly.

Professor A. Paul Alivisatos

Dissertation Committee Chair

For my parents,

Lai-Him and Lui-Heung,

the original Drs. Chan.

TABLE OF CONTENTS

LIST OF FIGURES ..... **v**

ACKNOWLEDGEMENTS ..... **vii**

CHAPTER 1 NANOCRYSTALS **1**

1.1 INTRODUCTION 1
1.2 MOTIVATION 2
1.3 BASIC PHYSICAL THEORY OF NANOCRYSTALS 3
1.3.1 Quantum confinement and semiconductors *3*
1.3.2 Thermodynamics *6*
1.4 BASIC SYNTHETIC METHODS FOR NANOCRYSTALS 7
1.4.1 Pyrolytic synthesis *8*
1.4.2 Current synthetic challenges *10*
1.5 REFERENCES 12

CHAPTER 2 MICROFLUIDIC REACTORS **14**

2.1 INTRODUCTION 14
2.2 THE HYDRODYNAMICS OF MICROFLUIDIC DEVICES 14
2.2.1 Laminar flow *14*
2.2.2 Transport of chemical species in microchannels *17*
2.2.3 Residence Time Distribution *18*
2.3 MICROFLUIDIC DEVICES FOR CHEMICAL SYNTHESIS AND ANALYSIS 21
2.3.1 General advantages *21*
2.3.2 Examples *22*
2.4 MICROFLUIDIC REACTORS FOR NANOSCALE MATERIALS 23
2.4.1 Advantages of microfluidic nanocrystal synthesis *24*
2.4.2 Challenges of nanoscale microreactors *25*
2.5 REFERENCES 27

CHAPTER 3 MICROFABRICATION AND EXPERIMENTAL PROTOCOLS **30**

3.1 INTRODUCTION 30
3.2 SUBSTRATES 30
3.3 BASIC GLASS MICROFABRICATION 32
3.4 CHANNEL SURFACE PASSIVATION 34
3.5 TEMPERATURE CONTROL 35
3.5.1 Microheater fabrication *37*
3.5.2 Heater control *38*
3.6 EXPERIMENTAL SCHEME & APPARATUS 39
3.7 REFERENCES 41

CHAPTER 4 SIZE-CONTROLLED GROWTH OF CDSE NANOCRYSTALS IN MICROFLUIDIC REACTORS **42**

4.1 INTRODUCTION 42
4.2 EXPERIMENTAL 44
4.3 RESULTS & DISCUSSION 46
4.4 CONCLUSION 49
4.5 REFERENCES 50

CHAPTER 5 SHAPE CONTROL OF NANOPARTICLES IN CONTINUOUS FLOW MICROREACTORS 52

5.1 INTRODUCTION 52
5.1.1 Examples of anisotropic nanocrystal synthesis 53
General theory of shape control 53
Rods 54
Tetrapods 56
Hollow shells 56
5.2 EXPERIMENTAL 57
5.2.1 Improvements over previous chips and protocols 57
Improved reagents 57
Mixing control 59
Temperature control 60
5.2.2 Microreactor chips 61
Sheath injection chip (*THD5c*) 61
Tetrapod rapid evolution chip (*T4EV1*) 64
5.2.3 Synthesis conditions 64
CdSe nanorods 64
CdTe nanocrystals 65
Hollow spheres 67
5.3 RESULTS & DISCUSSION 67
5.3.1 CdSe nanorods 67
5.3.2 CdSe spheres in oleic acid 72
5.3.3 CdTe nanocrystals in oleic acid 73
CdTe spheres 73
CdTe tetrapods 74
Short time evolution of CdTe tetrapod morphology 78
5.3.4 Cobalt Sulfide Hollow Shells 82
5.4 CONCLUSION 84
5.5 REFERENCES 86

CHAPTER 6 PROBLEMS WITH CONTINUOUS FLOW MICROREACTORS 88

6.1 INTRODUCTION 88
6.2 ATTEMPTS TO PREVENT PARTICLE DEPOSITION 88
6.2.1 Increasing particle solubility 89
6.2.2 Surface passivation 90
6.3 ATTEMPTS TO REDUCE RESIDENCE TIME DISTRIBUTION 90
6.3.1 Internal convection with staggered herringbone mixers 92
6.4 CONCLUSION 96
6.5 REFERENCES 96

CHAPTER 7 HIGH-TEMPERATURE MICROFLUIDIC SYNTHESIS OF CDSE NANOCRYSTALS IN NANOLITER DROPLETS 97

7.1 INTRODUCTION 97
7.2 EXPERIMENTAL 100
7.2.1 Microreactor design and fabrication 100
Microfabrication 102
Silanization 103
7.2.2 Droplet production & characterization. 103
7.2.3 Nanocrystal Synthesis 104
Reagents 104
Stock solution preparation 105
Synthesis apparatus & procedure. 105
Cleaning & characterization 106

7.3 RESULTS & DISCUSSION 107
7.3.1 Droplet formation at ambient temperature. *107*
7.3.2 High temperature droplet formation. *112*
7.3.3 High temperature nanocrystal synthesis *113*
7.4 CONCLUSION 119
7.5 REFERENCES 121

CHAPTER 8 MILLISECOND KINETICS OF NANOCRYSTAL CATION EXCHANGE USING MICROFLUIDIC X-RAY ABSORPTION SPECTROSCOPY 125

8.1 INTRODUCTION 125
8.2 EXPERIMENTAL 128
8.2.1 Device Design & Usage *128*
8.2.2 Fabrication *130*
8.2.3 Bonding *131*
8.2.4 Passivation *132*
8.2.5 Reagents/Solutions *132*
8.2.6 X-ray absorption spectroscopy *133*
8.2.7 Stopped-flow absorption experiments *135*
8.3 RESULTS & DISCUSSION 135
8.4 CONCLUSION 146
8.5 REFERENCES 148

CHAPTER 9 SUMMARY & OUTLOOK 151

9.1 SUMMARY OF RESEARCH 151
9.2 PERSPECTIVE 152
9.3 REALIZING THE UNFULFILLED POTENTIAL OF NANOPARTICLE MICROREACTORS 153
9.3.1 Improving existing syntheses and developing novel structures. *153*
9.3.2 Rapid screening, optimization, and characterization of nanocrystal reactions *156*
9.3.3 Parallel synthesis and scale-out of nanocrystal reactions *158*
9.4 THE IDEAL NANOCRYSTAL MICROREACTOR 159
9.5 FUTURE NANOCRYSTAL RESEARCH IN MICROFLUIDIC DEVICES 161
9.5.1 Droplet-based experiments *161*
9.5.2 Microfluidic X-ray characterization of nanoparticles *161*
9.5.3 Environmental manipulation and stimulation of nanoscale reactions *164*
9.6 CONCLUSION 165
9.7 REFERENCES 166

LIST OF FIGURES

Figure 1.1. The density of states in a molecule, small cluster, nanocrystal, and a bulk semiconductor. 3

Figure 1.2. Photoluminescence spectra of CdSe nanocrystals. 5

Figure 1.3. Typical apparatus and procedure for the synthesis of CdSe nanocrystals. 8

Figure 1.4. Idealized time-dependent concentration curve illustrating the four phases in the growth of colloids 8

Figure 2.1. Examples of laminar flow. 15

Figure 2.2. The parabolic velocity profile of laminar flow. 18

Figure 3.1. Basic glass microchip fabrication process flow. 32

Figure 3.2. Microfabricated heater process flow and control loop diagram 36

Figure 3.3. Schematic of the external apparatus and chip-to-world interface.. 39

Figure 4.1. Schematic of microreactor channels for CdSe sphere growth. 44

Figure 4.2. Size control of nanocrystal synthesis via temperature. 47

Figure 4.3. Size control of nanocrystal synthesis via flow rate and concentration.. 48

Figure 5.1. Wurzite CdSe nanorod model. 54

Figure 5.2. Sheath injection chip design.. 62

Figure 5.3. T4EV1 tetrapod rapid evolution chip 63

Figure 5.4. Transmission electron micrographs of nanorods grown at four different temperatures for 1 min 68

Figure 5.5. TEM image and powder X-ray diffraction pattern of 26 nm x 6 nm nanorods using Co Kα radiation.. 69

Figure 5.6. Size control of nanorod synthesis via temperature and flow rate/concentration in a 6-μL sheath injection reactor.. 70

Figure 5.7. Aggregated and overgrown particles collected during nanorod growth. 71

Figure 5.8. Online absorption spectra of CdSe nanospheres. 73

Figure 5.9. TEM micrograph and online fluorescence spectrum of 5.6 nm-diameter CdTe dots synthesized in a single injection reactor at 280 °C. 74

Figure 5.10. TEM images of CdTe tetrapods synthesized 77

Figure 5.11. Off-line fluorescence spectra for CdTe tetrapods collected from the sheath injection reactor at four different conditions 78

Figure 5.12. Time evolution of CdTe tetrapod growth at 260 °C. 80

Figure 5.13. TEM micrographs of overgrown CdTe tetrapod aggregates. 81

Figure 5.14. Cobalt sulfide hollow shells. 84
Figure 6.1. Staggered herringbone mixer schematic. 92
Figure 6.2. Fluorescence micrographs and cross-sectional intensity profiles of the staggered herringbone mixing of CdSe spheres in toluene. 93
Figure 6.3. Online absorption spectrum and TEM image of CdTe tetrapods synthesized with 25 μm-deep staggered herringbone mixers. 95
Figure 6.4. Two-phase plug flow for narrow residence time distribution and rapid mixing. 95
Figure 7.1. Microreactor channel design with droplet jet injector. 107
Figure 7.3. Optical micrographs of droplet formation. 108
Figure 7.4. Phase diagrams showing the location of droplet separation. 110
Figure 7.5. Transmission electron micrographs of CdSe nanocrystals synthesized in droplets. 113
Figure 7.6. On-line photoluminescence spectrum and off-line absorption spectrum of nanocrystals grown in droplets. 114
Figure 7.7. Photoluminescence wavelength of nanocrystal drops. 114
Figure 7.8. Photoluminescence time traces vs. flow rate and temperature 117
Figure 8.1. Channel schematics and micrographs of the XAS microreactor chip 128
Figure 8.2. XAS Chip fabrication process flow. 129
Figure 8.3. X-ray beam paths through the microreactor channel. 133
Figure 8.4. Time-resolved Se K-edge XAS spectra acquired *in situ* during the CdSe→Ag_2Se nanocrystal cation exchange reaction. 136
Figure 8.5. Fractional conversion vs. time using fit parameters extracted from XAS fits and stopped flow experiments. 138
Figure 8.6. Powder X-ray diffraction patterns of unreacted and reacted nanocrystals. 139
Figure 8.7. Comparison of the stopped flow kinetic curve with theoretical diffusion and 2^{nd} order kinetics curves 142
Figure 8.8. Fraction reacted vs. time with various volume fractions of methanol. 144
Figure 8.9. Stopped flow absorption curves at various dodecylamine concentrations 144
Figure 9.1. CdTe tetrapod cores synthesized in droplets. 154
Figure 9.2. Pinched-flow fission and sorting of droplets. 155
Figure 9.3. Two-phase counter-flow extractor for cleaning nanoparticles. 158
Figure 9.4. Horizontal sheath microreactor for X-ray fluorescence studies. 163

ACKNOWLEDGEMENTS

Graduate school has been a long, strange journey that I would not have survived without the support of my mentors, labmates, friends, and family.

I am grateful to my advisors, Prof. Paul Alivisatos and Prof. Richard Mathies, for providing the inspiration for this research and allowing me to pursue such a risky project. They gave me the independence and funding to wander into uncharted territory, and reminded me to keep a positive outlook even when prospects seemed bleak.

My research and sanity would not have been possible without the assistance and camaraderie of my extended family in the Alivisatos and Mathies groups. Liberato Manna, Maria Casula, Donghee Son, and Richard Robinson provided me with technical help, ideas, and stimulating conversation. Deborah Aruguete was there for me from my first year to our days as the old guard of Alivisatos Nation. I will never forget the wisdom and friendship of my fellow Baton Rouge native and Alivisatoid, Benjamin Boussert, who perished tragically before our nascent project together could take flight. If not for his passing, there might have been another chapter in this dissertation.

On the Mathies DNAside, I am grateful for the assistance and offbeat humor of Charlie Emrich, Brian Paegel, Eric Lagally, Teris Liu, Nick Toriello, Palani Kumaresan, and Mariam Elnaggar.

My research efforts would not have been possible without the superhuman efforts of my group administrators, Mary Hammond, Rita Tidwell, and Helen Cameron. Deborah Aruguete, Haitao Liu, and Lien Chau reviewed this manuscript for me when I could not bear to read it any more.

At the Advanced Light Source at Lawrence Berkeley National Lab, I thank beamline scientists Matthew Marcus and Sirine Fakra for their invaluable help during marathon synchrotron experiments. Microfabrication was performed at the U.C. Berkeley Microfabrication Laboratory, and I am grateful to all of the staff members who maintained the equipment and to the users who provided tips and training.

Outside of Berkeley, I am indebted to Prof. Xiaogang Peng at the University of Arkansas and Dr. J. Wallace Parce at Nanosys, Inc., for conversations that turned out to be important junctures in my research. I thank Prof. Justin Cooper-White and his Tissue Engineering and Microfluidics lab at the University of Queensland, Australia, along with the National Science Foundation's *East Asia Pacific Summer Institutes*, for granting me the once-in-a-lifetime chance to perform microfluidics research in Australia in the summer of 2006.

I also thank Temba Maqubela, my high school chemistry teacher at Phillips Academy, for inspiring me to pursue chemistry in college, and I thank my teachers at Andover for giving me the skills to clearly and confidently present my ideas. I am grateful to Prof. Hongjie Dai at Stanford University and Dr. Robert D. Miller at IBM Almaden Research Center for giving me my first undergraduate research experiences in nanotechnology and materials science.

Finally, I would like to thank my parents, Dr. Lai-Him Chan and Dr. Lui-Heung Chan, for providing me with the best education and upbringing that anyone could desire. I thank my sister, Dr. Clara Chan, for ensuring that I will be the last remaining person in my family to receive a Ph. D.

This research was funded by the Department of Energy, by the U.C. Berkeley Center for Analytical Biotechnology, and by a National Defense Science and Engineering Graduate Fellowship.

Chapter 1 Nanocrystals

1.1 INTRODUCTION

Nanoscale materials exhibit unique size-dependent properties due to quantum confinement and surface effects at nanometer (10^{-9} m) dimensions. Reproducibly synthesizing, characterizing, and performing reactions with such materials is a challenge due to their small size. My dissertation investigates the use of microfluidic reactors for the controlled synthesis, reaction, and manipulation of semiconductor nanocrystals. In this chapter, I discuss the physical properties and traditional pyrolytic synthesis of colloidal quantum dots, and in the following chapter, I introduce microfluidic devices and their relevant hydrodynamic theory. The practical integration of nanocrystal reactions with microfluidics is presented in the protocols in Chapter 3. I demonstrate the high-temperature synthesis of spherical CdSe nanocrystals in continuous flow microreactors in Chapter 4 and extend such research to the synthesis of different shapes and materials in Chapter 5. Chapter 6 presents the disadvantages of these continuous flow approaches and describes my attempts to overcome these obstacles. In Chapter 7, I introduce the use of droplet-based microreactors as a solution to the challenges of high-temperature growth. In Chapter 8, I characterize the cation exchange of existing nanocrystals by probing them *in situ* with X-ray Absorption Spectroscopy. Finally, I evaluate microfluidic nanoparticle research and provide a bright outlook for future directions in the field.

1.2 MOTIVATION

Nanocrystals are crystalline particles with all three of their dimensions on the nanometer scale (1-100 nm). In this size regime, nanocrystals are large enough to exhibit the defined lattices of bulk crystals but are small enough to exhibit unique size-dependent properties due to quantum confinement and high surface-area-to-volume ratios (SA:V).[1] Such size-dependent phenomena include altered charging energies,[2] melting temperatures,[1] phase transition pressures,[3] magnetism,[4] and catalytic activity.[5-7] In semiconductor nanocrystals such as CdS, CdSe, ZnSe, InP, and GaAs, quantum size effects increase the effective band gaps of the materials. This phenomenon is most evident in the blue shifts of the nanoparticle emission peaks as particle diameters are decreased.[1]

The ability to tune material properties via particle size without altering chemical composition has led to the incorporation of semiconductor nanocrystals in a wide range applications, including biological labeling,[8] photovoltaic cells,[9] catalysts,[5-7] light-emitting diodes,[10], lasers[11]and single-nanoparticle transistors.[12] Nanoscale materials also represent model systems for systematically studying chemical reactivity, thermodynamics, and quantum phenomena in confined geometries.

In order to fully exploit such applications, however, nanocrystals must be reproducibly synthesized with high yield and crystallinity and with narrow distribution in size and shape. Currently, high temperature pyrolytic injection schemes can achieve single crystal colloidal quantum dots with ~5% size distribution,[13] making such techniques the most effective for synthesizing colloidal nanocrystals. Such methods, however, are highly user- and condition-dependent and result in variations in size and shape distributions across batches. Clearly, this lack of systematic control and reproducibility is undesirable for physical

characterization and industrial production. The goal of this research is to control and characterize nanocrystal synthesis and post-synthetic reactions using microfluidic devices.

1.3 BASIC PHYSICAL THEORY OF NANOCRYSTALS

1.3.1 Quantum confinement and semiconductors

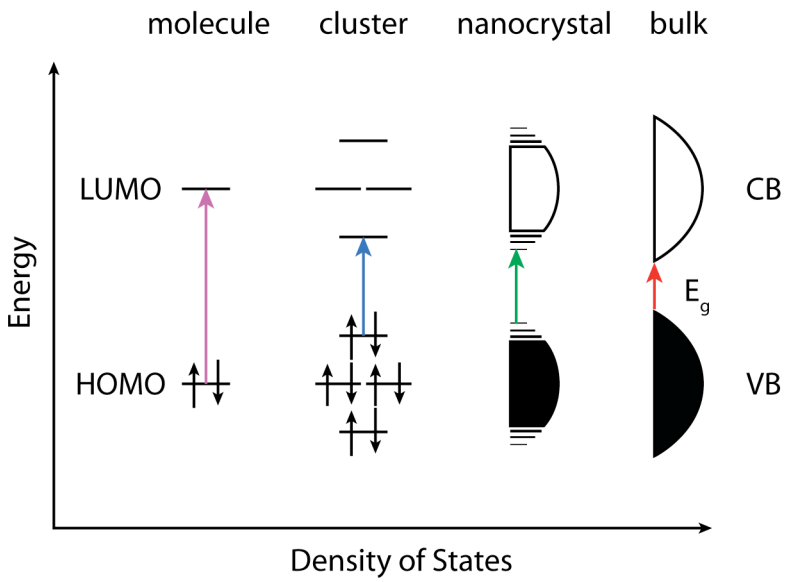

Figure 1.1. Illustration of the density of states in a molecule, small cluster, nanocrystal, and a bulk semiconductor. The discrete, highest occupied and lowest unoccupied molecular orbitals (HOMO & LUMO) are shown for the molecule, while the valence band (VB), conduction band (CB), and band gap (E_g) are shown for the bulk semiconductor. The transitions between these band-edge states illustrate the size-dependence of the band gap.

Molecules exhibit discrete energy levels, while bulk crystals do not (Figure 1.1). Due to the wave-like behavior of quantum objects, electrons in a molecule are tightly confined to their nuclei in well-defined molecular orbitals, while electrons in a bulk semiconductor are delocalized over the entire crystal in continuous bands. As molecules are assembled into clusters, the molecular orbitals interfere such that the clusters' energy levels are more densely packed and degenerate near the center of the distribution of states. When the energy difference between adjacent states, ΔE, is much less than the thermal energy kT, as in bulk crystals, the energy levels are considered to be continuous rather than discrete. Nanocrystals occupy the mesoscopic region between the molecular and bulk regimes. While the dense centers of nanocrystal bands are continuous, the sparse band edges have discrete, molecular-like energy levels.

In semiconductor crystals, the Fermi energy lies in the band gap (E_g) between the mostly filled valence band (VB) and the largely unfilled conduction band (CB). The band-edge states that bound the band gap are analogous to the highest occupied and lowest unoccupied molecular orbitals (HOMO and LUMO), respectively, of an individual molecule. In semiconductor nanocrystals, the energies of these discrete band-edge states vary with their level of quantum confinement, and thus the magnitude of band-edge electronic transitions vary strongly with particle size, as shown in Figure 1.1. This increase in the effective band gap with decreased size is most evident in the shifting photoluminescence spectra of semiconductor nanocrystals, as shown in Figure 1.2. The size dependence of the peak positions means that optical spectra can be used to extract the size and size distributions of nanocrystals.

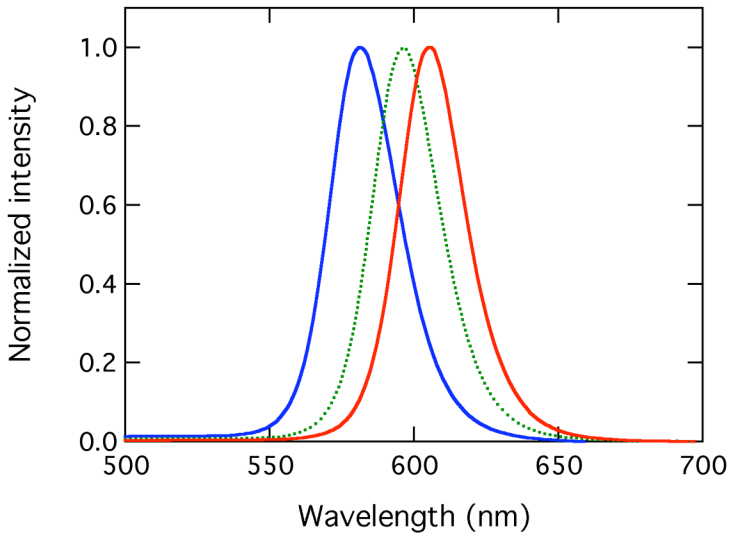

Figure 1.2. Photoluminescence spectra of CdSe nanocrystals with diameters of (left to right) 3.6, 4.0, and 4.2 nm.

Quantum size effects are only significant when crystal sizes are comparable to the wavelength of the relevant quantum object. In semiconductor crystals, the relevant quantum object is the "exciton," the electron-hole pair created when an electron is excited from the valence band to the conduction band.[14] The relevant length scale for quantum confinement is the Bohr radius of the exciton, a_B, which is given by:

$$a_B = \frac{4\pi\varepsilon_o\varepsilon\hbar^2}{e^2 m_o}\left(\frac{1}{m_e^*} + \frac{1}{m_h^*}\right)$$

where ε is the dielectric constant of the semiconductor, m_o is the mass of an electron, and m_e^* and m_e^* are the effective masses of the electron and hole, respectively.[15] In semiconductors, these effective masses are much smaller than the actual electron mass, resulting in large Bohr radii. For CdSe, $m_e^* = 0.13$, and $m_h^* = 0.8$, resulting in $a_B = 5.5$ nm.[14] Because the Bohr radii of semiconductors are typically in the 1-10 nm regime, quantum size

effects figure prominently in nanoscale semiconductors. Particles with radius $r << a_B$ are considered to be strongly confined, and the exciton energy is largely a function of the independent confinement energies of the electron and hole.[15] This is the case for the model system of CdSe, where typical radii range from 1 to 5 nm.

While the actual energies of the band-edge states in semiconductor nanocrystals are complex to calculate, the canonical "particle in a box" model can be used to understand the size-dependence of the exciton energy. In the strongly confined regime, the ground state exciton energy can be approximated with the expression:

$$E(1s_e 1s_h) = E_g + \frac{\pi^2 \hbar^2}{2m_o R^2}\left(\frac{1}{m_e^*} + \frac{1}{m_h^*}\right) - 1.8\frac{e^2}{4\pi\varepsilon_o \varepsilon R}$$

where R is the radius of the nanocrystal.[16] The $1/R^2$ dependence of the second term describes the spherical particle-in-a-box type quantum confinement of the electron and hole, while the $1/R$ dependence of the third term describes their Coulombic attraction. While this modified particle-in-a-box equation does not predict the exact exciton energies of nanocrystals, it provides an accessible model for understanding the increase in exciton energy with decreasing R.

1.3.2 Thermodynamics

The thermodynamics of nanocrystals are dominated by their surface energies due to scaling laws that extend from bulk to nanoscale materials. With the high SA:V of nanocrystals, a large percentage of their 10^2-10^7 atoms are at or near the surface, and this value varies significantly with nanocrystal diameter, which typically ranges from 5 to 200 unit cells.[13] For example, one mole of bulk CdSe has 0.00001% of its atoms on the surface, while

a 6 nm-diameter sphere of CdSe consists of 30% surface atoms, and a 3 nm CdSe sphere has 60%, or a majority, of its atoms on the surface. Surface atoms have higher free energies due to their lower coordination ("dangling bonds"), their inhomogeneous charge distributions, and their interactions with solvent or surfactant molecules. In quantitative terms, the free energy of a crystal is the sum of its bulk free energy, which scales as R^3, and its surface energy, which scales as R^2. As R is decreased, the surface contribution increases. The size dependence of these surface contributions to the overall free energy of a crystal leads to size-dependent thermodynamic properties, from equilibrium constants and electrochemical potentials to phase transition temperatures and pressures.

Nanocrystals also feature fewer point defects than bulk materials, due to the lower configurational entropy of defects in confined materials. Furthermore, such defects can rapidly diffuse out of nanocrystals due to their high SA:V.

1.4 BASIC SYNTHETIC METHODS FOR NANOCRYSTALS

Nanoparticles and quantum dots can be synthesized using a variety of physical methods, including molecular beam epitaxy, metal-organic chemical vapor deposition, pulsed laser deposition, and "top-down" lithographic techniques.[14] This dissertation, however, focuses on the "bottom-up" solution phase synthesis of colloidal quantum dots, which has the advantages of higher throughput and processability without the need for expensive equipment and time-consuming fabrication.

The ideal solution-phase colloidal synthesis would consistently produce a population of defect-free crystals of identical lattice structure, shape, orientation, and surface functionality, and would be tunable across a wide range of sizes. Such a synthetic scheme

would require an infinitely short nucleation phase, followed by a temporally distinct growth phase in which all particles grow controllably at the same rate.

1.4.1 Pyrolytic synthesis

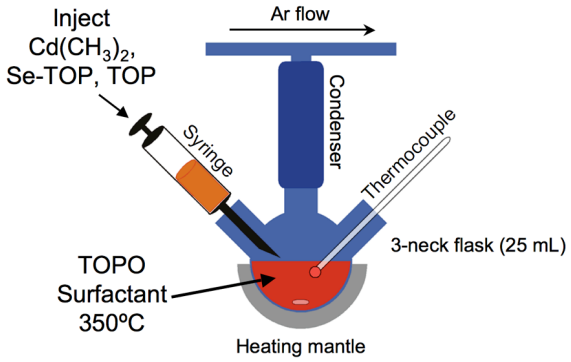

Figure 1.3. Typical apparatus and procedure for the pyrolytic synthesis of CdSe nanocrystals.

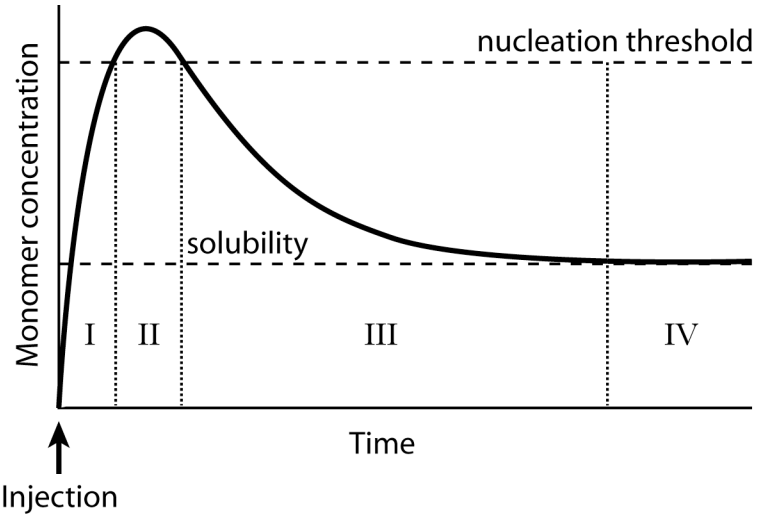

Figure 1.4. Idealized time-dependent concentration curve illustrating the four phases in the growth of colloids: (I) monomer accumulation, (II) nucleation, (III) growth, and (IV) ripening. Adapted from La Mer and Dinegar.[17]

The most widely accepted method for synthesizing monodisperse and highly crystalline semiconductor particles is via pyrolytic decomposition in hot liquid surfactant.[13] In this method, organometallic precursors such as $Cd(CH_3)_2$ and Se-tri-*n*-octylphosphine (Se-TOP) are injected into a flask of hot surfactant such as tri-*n*-octylphosphine oxide (TOPO) in an inert atmosphere, as shown schematically in Figure 1.3.[18] This simple technique yields distributions in nanocrystal diameter as low as 5% relative standard deviation.[13]

The nucleation and growth of particles in this technique can be explained with theory derived from La Mer and Dinegar for the growth of sols.[17] Colloidal growth occurs in four phases, as depicted in Figure 1.4, and depends on the solubility of the bulk material, monomer diffusion constants, the number of nuclei, and the temperature. During Phase I, the reactive precursors are injected into the solution, producing a supersaturated plume of monomers. After the concentration exceeds a certain nucleation threshold, the monomers precipitate rapidly into small clusters. This nucleation phase (II) can also be instigated by altering the solubility or chemical potential via other mechanisms, such as suddenly changing the temperature or pH of the solution. For the injection technique, the nucleation phase terminates quickly as the supersaturation decreases due to the rapid consumption of monomer, the homogenization of monomer concentration, and the drop in temperature caused by the injection. Subsequently, no new nuclei are formed, and the existing nuclei grow (Phase III) through the controlled addition of monomers, which is mediated by the reversible binding of surfactants to the nanocrystal surfaces. Surfactants are critical to controlled growth because their long, flexible chains sterically prevent aggregation and confer solubility by increasing the entropy of the particles.[1] The high-temperature growth encourages the growth of single domains by increasing the rates of monomer adsorption and

desorption onto lattice sites, while surfactants prevent uncontrolled monomer addition that leads to defective, bulk crystals.

During the growth phase (III), the monomer concentration is consumed continuously until the solution is no longer supersaturated. When monomer is sufficiently depleted, Ostwald ripening (Phase IV) can occur via the dissolution of smaller particles, whose material contributes to the growth of larger particles. This ripening is undesirable because it increases the particle size distribution. To facilitate the monodisperse growth of larger particles, additional monomer can be introduced to the system to maintain the overall concentration between the nucleation threshold and ripening thresholds.[19]

1.4.2 Current synthetic challenges

Injection-based pyrolysis is currently being used to synthesize nanocrystals with various shapes[20] and materials in various solvents and surfactants.[21,22] The secondary addition of reactants after initial particle growth can be used to form hollow nanoparticles,[23] to exchange cations,[24] and to produce complex heterostructures such as core-shell, bar-code, and dendritic nanoparticles.[25]

Despite the success of the pyrolytic injection method, however, existing synthetic techniques can be improved. Nucleation and growth are not entirely separate, and ripening can also broaden size and shape distributions. Scaling pyrolytic injection schemes from 25 mL to ~1 L for large-scale production results in different kinetics and poor size distributions, due to the slow injection and mixing times for such large volumes.

Most significantly, injection-based syntheses can be fairly irreproducible, especially across personnel and laboratories. The injection of reactive precursors, essential for inducing a precise nucleation event, results in chaotic hydrodynamics and temperature profiles that cause unpredictable nucleation and growth rates. According to homogenous nucleation theory, the exponential term of the nucleation rate is proportional to $1/T^3[\ln(C/C_s)]^2$, where C is the monomer concentration and C_s is the monomer solubility.[26] Thus, drastic changes in the nucleation rate alter the monomer population available for the growth of each particle. As a result, the nanocrystal size and distribution cannot be predicted precisely for a given set of conditions, which is inconvenient for systematic scientific investigation and for application-based production.

While *in situ* absorption spectroscopy[27] can be used to estimate the particle size during reactions, the finite (~1 minute) time required to thermally quench a reaction is significant compared to typical reaction times (~5 minutes). Other characterization methods, such as photoluminescence, cannot be performed *in situ* due to the high temperatures and harsh synthesis conditions, making it difficult to perform kinetic measurements or quickly optimize new synthesis conditions.

Peng *et al.* have suggested that automating the synthesis procedure with feedback from *in situ* monitoring devices may provide the level of control necessary to improve reproducibility, monodispersity, and physical properties.[19] Dushkin *et al.* have also proposed flow reactor schemes for more reproducible syntheses for kinetic studies, optimization, and industrial-production.[28] While such automated control and characterization would be advantageous, the caustic reagents and extreme conditions for high quality nanoparticle synthesis make such apparatuses very difficult to build and operate.

In light of the challenges to improving current synthetic methods in bulk liquids, I hypothesize that microfluidic reactors can more reproducibly control the synthesis and further reactions of semiconductor nanocrystals. In the next chapter, I will introduce the unique hydrodynamic properties of microfluidic reactors and discuss the advantages of performing nanocrystal reactions in microscale fluid flows.

1.5 REFERENCES

(1) Alivisatos, A. P. *J. Phys. Chem.* **1996**, *100*, 13226.

(2) Alivisatos, A. P. *Science* **1996**, *271*, 933.

(3) Tolbert, S. H.; Alivisatos, A. P. *Annu. Rev. Phys. Chem.* **1995**, *46*, 595.

(4) Puntes, V. F.; Krishnan, K. M.; Alivisatos, P. *Appl. Phys. Lett.* **2001**, *78*, 2187.

(5) Zhang, Z. B.; Wang, C. C.; Zakaria, R.; Ying, J. Y. *J. Phys. Chem. B* **1998**, *102*, 10871.

(6) Somorjai, G. A.; Rioux, R. M. *Catal. Today* **2005**, *100*, 201.

(7) Zarur, A. J.; Ying, J. Y. *Nature* **2000**, *403*, 65.

(8) Bruchez, M.; Moronne, M.; Gin, P.; Weiss, S.; Alivisatos, A. P. *Science* **1998**, *281*, 2013.

(9) Huynh, W. U.; Dittmer, J. J.; Alivisatos, A. P. *Science* **2002**, *295*, 2425.

(10) Colvin, V. L.; Schlamp, M. C.; Alivisatos, A. P. *Nature* **1994**, *370*, 354.

(11) Klimov, V. I.; Mikhailovsky, A. A.; Xu, S.; Malko, A.; Hollingsworth, J. A.; Leatherdale, C. A.; Eisler, H. J.; Bawendi, M. G. *Science* **2000**, *290*, 314.

(12) Klein, D. L.; Roth, R.; Lim, A. K. L.; Alivisatos, A. P.; McEuen, P. L. *Nature* **1997**, *389*, 699.

(13) Murray, C. B.; Kagan, C. R.; Bawendi, M. G. *Annu. Rev. Mater. Sci.* **2000**, *30*, 545.

(14) Bukowski, T. J.; Simmons, J. H. *Crit. Rev. Solid State Mater. Sci.* **2002**, *27*, 119.

(15) Efros, A. L.; Rosen, M. *Annu. Rev. Mater. Sci.* **2000**, *30*, 475.

(16) Brus, L. E. *J. Chem. Phys.* **1983**, *79*, 5566.

(17) Lamer, V. K.; Dinegar, R. H. *J. Am. Chem. Soc.* **1950**, *72*, 4847.

(18) Murray, C. B.; Norris, D. J.; Bawendi, M. G. *J. Am. Chem. Soc.* **1993**, *115*, 8706.

(19) Peng, X. G.; Wickham, J.; Alivisatos, A. P. *J. Am. Chem. Soc.* **1998**, *120*, 5343.

(20) Manna, L.; Scher, E. C.; Alivisatos, A. P. *J. Am. Chem. Soc.* **2000**, *122*, 12700.

(21) Qu, L.; Peng, Z. A.; Peng, X. *Nano Lett.* **2001**, *1*, 333.

(22) Yu, M. W.; Peng, X. G. *Angew. Chem. Int. Ed.* **2002**, *41*, 2368.

(23) Yin, Y. D.; Rioux, R. M.; Erdonmez, C. K.; Hughes, S.; Somorjai, G. A.; Alivisatos, A. P. *Science* **2004**, *304*, 711.

(24) Son, D. H.; Hughes, S. M.; Yin, Y. D.; Alivisatos, A. P. *Science* **2004**, *306*, 1009.

(25) Milliron, D. J.; Hughes, S. M.; Cui, Y.; Manna, L.; Li, J. B.; Wang, L. W.; Alivisatos, A. P. *Nature* **2004**, *430*, 190.

(26) Abraham, F. *Homogeneous Nucleation Theory*; Academic Press: New York, 1974.

(27) Qu, L. H.; Yu, W. W.; Peng, X. P. *Nano Lett.* **2004**, *4*, 465.

(28) Dushkin, C. D.; Saita, S.; Yoshie, K.; Yamaguchi, Y. *Adv. Colloid Interface Sci.* **2000**, *88*, 37.

Chapter 2 Microfluidic Reactors

2.1 INTRODUCTION

Much as reducing the size of materials to nanometer dimensions enhances quantum and thermodynamic phenomena that are insignificant in bulk materials, reducing the dimensions of fluid flows to micrometer dimensions enhances hydrodynamic and transport phenomena relative to bulk fluids. Unlike quantum confinement in nanoparticles, however, the enhanced phenomena in microscale flows are purely a result of scaling laws that extend from the macroscale. Microfluidic devices, which are typically microfabricated networks of channels, take advantage of these scaling laws to manipulate fluids in a controllable fashion and perform tasks such as biological analysis,[1] chemical synthesis,[2] sorting and separation,[3] and fluidic or optical switching.[4] In this chapter, we will describe the theory and advantages of microfluidic devices and their application as microscale chemical reactors.

2.2 THE HYDRODYNAMICS OF MICROFLUIDIC DEVICES

2.2.1 Laminar flow

The significance of viscous forces is enhanced in microfluidic devices due to their small length scales and high surface area-to-volume ratios (SA:V). The viscosity, the propensity of a fluid to resist shear, is the determining factor for fluid velocities in small

channels due to the large shear rates near channel walls. In bulk fluids, where wall effects are insignificant, fluid velocities are determined more by inertial, or convective, forces.

The ratio of the inertial forces to the viscous forces in a fluid is described by the dimensionless Reynolds number (*Re*), which is defined as:

$$\mathrm{Re} = \frac{\rho \cdot u \cdot d}{\eta}$$

where ρ is the fluid density, u is the average linear velocity, η is the viscosity, and d is the characteristic length.[5] In microchannels, d is the hydraulic diameter of the channel, d_h, which can be approximated as $4A/P$, where A is the cross sectional area, and P is the perimeter. In channels with d ~100 μm, *Re* values are typically <1, which on the macroscale is typically observed only with viscous or slow-moving fluids. When *Re* < 2000, fluid flows are laminar, meaning that fluid particles tend to travel along well-defined streamlines with no turbulence.

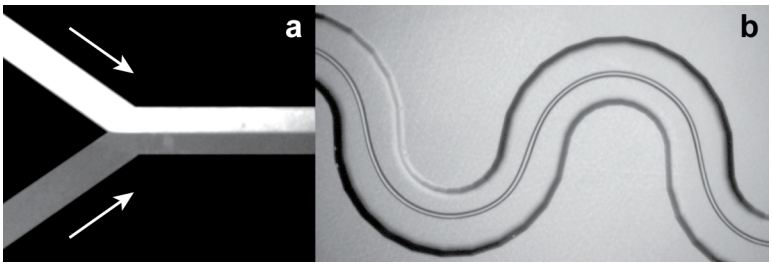

Figure 2.1. Examples of laminar flow. Micrographs of (a) fluorescent streams joining in a Y-junction, and (b) the sheath flow of two immiscible fluids in a serpentine microchannel. Channel widths are ~200 μm.

Because flow in microfluidic devices is laminar, streamlines can be precisely defined by the channel geometries and flow rates, as shown in Figure 2.1. Mass, heat, and momentum transfer can be solved analytically for simple but often sufficient models such as laminar flow in 2-D slots and cylindrical pipes.

For laminar flow in a cylindrical pipe of radius r_o, the solution of the Navier-Stokes equation shows that the velocity profile across the channel has a parabolic dependence with the radial coordinate r,[5] as illustrated by Figure 2.2a:

$$u(r) = 2u_{avg}\left[1 - \left(\frac{r}{r_o}\right)^2\right]$$

Due to the viscosity of the fluid and the assumed no-slip boundary condition, fluid near the walls is barely moving, while the fluid in the center of the channel has the maximum velocity, $u_{max} = 2u_{avg}$. 2D slot flow exhibits a similar parabolic velocity profile, with $u_{max} = 1.5u_{avg}$ at the midpoint between two parallel plates.

Laminar flow also allows the straightforward calculation of the pressure drop ΔP_{cyl} required to flow a fluid at volumetric flow rate Q through a pipe of radius r and length L:

$$\Delta P_{cyl} = \frac{8Q\eta L}{\pi r^4}$$

For laminar flow in rectangular channels with height h, width w, and $h/w \leq 0.7$, ΔP_{rect} can be approximated to within 10% using the following expression:[4]

$$\Delta P_{rect} \cong \frac{12Q\eta L}{wh^3}\left[1-6\left(\frac{2}{\pi}\right)^5\left(\frac{h}{w}\right)\right]^{-1}$$

These velocity and pressure relations have a profound impact on the design of microfluidic experiments and devices. For example, reducing the radius of a cylindrical channel by a factor of 2 will increase the pressure by a factor of 16 due to its $1/r^4$ dependence, whereas halving h in a rectangular channel with small h/w results in a ~8x increase in the pressure due to the $1/h^3$ dependence on ΔP.

2.2.2 Transport of chemical species in microchannels

Because transverse mixing in laminar flow occurs strictly through diffusion,[4] chemical transport and gradients are reproducible and tunable in microfluidic devices. Relative to bulk fluids, mixing times in microchannels are rapid because the diffusion time is proportional to l^2/D_{diff}, where l is the average diffusion length and D_{diff} is the diffusion constant. Relative to the short residence times (<1 s) commonly observed with microchannels, however, diffusion can be comparatively slow.

The ratio between convective and diffusive transport is described by the Péclet number (*Pe*) such that:

$$Pe = \frac{ud_h}{D_{diff}}$$

At high *Pe*, particles move rapidly through microchannels without substantial mixing, while at low *Pe*, species diffuse rapidly without substantial convection.

The wide range of *Pe* observed with microfluidic devices can be exploited for chemical production and analysis. In laminar flow at high *Pe*, little mixing occurs between adjacent streams, as shown in Figure 2.1a, and the slow diffusive mixing is generally confined to the interface. Kamholz, *et al.*[6] have used such diffusive T-mixers to perform biological assays in which small fluorophores diffuse rapidly into the streams of larger proteins, which do not diffuse significantly due to their high *Pe*. Pollack, *et al.*[7] used similar concepts to rapidly (<1 ms) mix reagents over small d_h and induce protein folding. Kenis, *et al.*[8] have utilized the precision of laminar flow and slow diffusion to reduce silver(I) ions and pattern silver wires in microchannels.

2.2.3 Residence Time Distribution

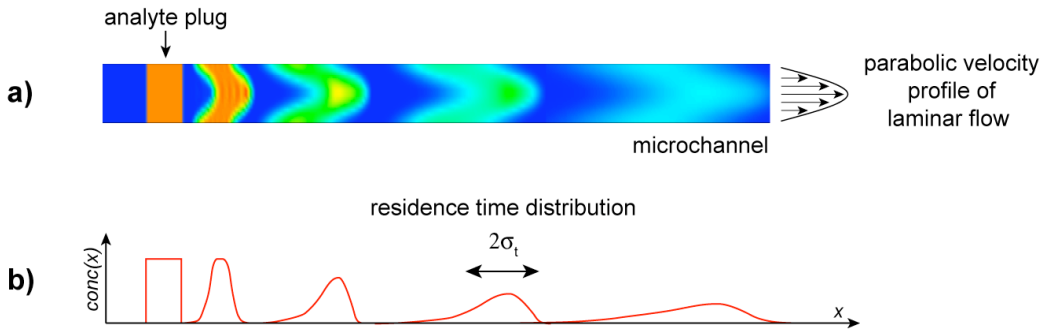

Figure 2.2. (a) Condensed simulation showing the effect of the parabolic velocity profile of laminar flow on an analyte plug. The vertical dimension has been stretched for visibility. (b) Schematic concentration profiles for the plugs in (a).

An important design consideration when transporting chemical species in laminar flows is that a population of reagents entering a microchannel at time t=0 will exit the channel with a distribution of residence times about τ, the average residence time.[9,10] This residence time distribution (RTD) is a result of the complex interplay between the convective forces that carry particles along the channel at different velocities and the molecular diffusion that transports species radially across the channel. At the high *Pe* and low *Re* typically observed in microchannels, axial diffusion is negligible compared to the length of the channel, *L*. Instead, a homogeneous plug of analytes is distorted in a parabolic profile such that, after a time Δt, the analytes in the center of the channel will have traveled farther than the analytes near the walls of the channel (Figure 2.2a). In the absence of diffusion (*Pe* >> 1), such convective dispersion results in an extremely broad and asymmetric concentration profile with a spike in concentration at the head of the plug, and a long, gradually decreasing tail with a longer residence time (Figure 2.2b).

In a microfluidic channel, the radial dimensions are very small, resulting in the rapid diffusion of analytes between the center and edges of the channel. This radial diffusion redistributes the analytes such that each particle experiences a distribution of velocities and such that the plug becomes more homogeneous in concentration. By giving slow-moving particles near the walls of a channel the chance to diffuse into the fast-moving center, radial diffusion reduces both the asymmetry and magnitude of the dispersion in the axial direction.

The dispersion profile for laminar flow in microchannels can be calculated using Taylor dispersion theory.[9,11,12] The RTD is expressed as the standard deviation of the residence time, σ_t, such that:

$$\frac{\sigma_t^2}{\tau^2} = 2\left(\frac{D_{disp}}{uL}\right) + 8\left(\frac{D_{disp}}{uL}\right)^2$$

where D_{disp} is the time-dependent dispersion coefficient.[11] For a channel of circular cross section,

$$D_{disp} = D_{diff} + \frac{u^2 d_h^2}{192 D_{diff}}$$

where D_{diff} is the molecular or particle diffusion constant, and d_h is the hydraulic diameter of the channel. Expressions for D_{disp} for other cross-sectional geometries[11] give similar results within a factor of two.

D_{disp}/uL is the ratio between the spreading of the dispersion and the rate of transport down the channel, and values >0.01 indicate that convective forces skew the distribution such that it is not Gaussian, as would be the case for pure diffusion in plug flow.

Although axial dispersion is reduced significantly in microfluidic devices as compared to macroscopic flow reactors, Taylor theory demonstrates that dispersion still plays a significant role in species transport at short residence times. For example, for a plug with τ = 3.3 s and u_{avg} = 3 mm/s flowing in a reactor with L = 20 mm and d_h = 100 μm, the ratio D_{disp}/uL is 0.03 when D_{diff} ~5×10^{-6} cm^2/s, indicating that there is substantial deviation from a Gaussian distribution. As a result, the dispersion constant, D_{disp} = 4×10^{-2} cm^2/s, is far greater than the diffusion constant, and the RTD is ~27% relative standard deviation.

2.3 MICROFLUIDIC DEVICES FOR CHEMICAL SYNTHESIS AND ANALYSIS

2.3.1 General advantages

Applying the unique transport phenomena on the microscale, microfluidic devices can precisely specify parameters such as concentration and temperature reproducibly in time and space, making them particularly attractive for performing chemical reactions and analysis.

The laminar flow in microscale channels leads to predictable hydrodynamics, chemical gradients, and heat transport that can be easily specified and modeled. The high SA:V of microfluidic channels results in rapid thermal transport between the relatively large thermal mass of the substrate, enabling the isothermal control of highly exothermic chemical reactions or temperature sensitive applications such as capillary electrophoresis. Exquisite thermal control can be performed by flowing fluids through a sequence of precisely defined heat zones or by rapidly cycling heaters that take advantage of the small substrate dimensions.[13]

Complex reaction schemes can be programmed into the geometries of the microchannels, and components such as switches, pumps, and valves can shuttle pL and nL volumes to specific locations at high frequencies.[14] Such small volumes can also be encapsulated and transported in droplets[15] and between gas bubbles,[16] both of which can be generated controllably due to the relative enhancement of surface tension and the reduced effects of buoyancy in microfluidic devices.

Predictable fluid velocities allow for sensitive *in situ* or on-line analysis in microfluidic devices. High SA:V allows small but representative volumes to be stimulated and probed with techniques such as fluorescence, absorption, chemoluminescence, electrochemical detection,[17,18] and nuclear magnetic resonance.[19] In devices where the average linear velocity is constant, the residence time can be extrapolated from the distance traveled down the channel. Due to the steady state nature of such devices, the time resolution is decoupled from acquisition time, enabling the detection at low signal and with rapid kinetics. Due to low sample volumes and the ease of fabricating parallel arrays of devices, massively multiplexed detection enables the rapid screening of numerous samples or conditions in a single microfluidic chip.[20,21]

From a practical perspective, these scientific advantages make microfluidic operations more cost effective, environmentally friendly,[22] and less hazardous.[23] Microfluidic reactors are particularly valuable for mass-transfer limited reactions and those that can have runaway conditions or explosive concerns.[24] The integrated, monolithic, and automated nature of microfluidic devices makes them attractive as microscale chemical factories that can be easily prototyped and then scaled "out" in parallel. This feature is particularly important for industrial production and for transport-dependent reactions that do not scale with volume.[2]

2.3.2 Examples

With such advantages in mind, microfluidic devices have been used for a variety of chemical applications. The most successful scientific and commercial applications of microfluidics have been for biochemical analyses due to their mild conditions, low sample

sizes, and need for parallel screening.[1] Such applications include DNA sequencing,[25] clinical analysis,[26] amplification via polymerase chain reaction (PCR),[13] protein and amino acid analysis,[27] and sample preparation.[28]

Microfluidic reactors have performed synthetic reactions in the organic and aqueous solvents[29] as well as in ionic liquids.[30] Organic reactions ranging from peptide synthesis[31] and Aldol condensation[32] to Wittig reactions[33] and Baeyer-Villiger oxidation[34] have been performed in microfluidic devices,[29] demonstrating increased reaction rates, yields,[35] and selectivities, which are attributed to the precise control over mixing, concentration, and temperature in microenvironments.[36]

The high SA:V of microchannels and multiphase flows have enhanced transfer rates for microfluidic heterogeneous reactions such gas-liquid fluorination,[37] gas-solid catalytic oxidation,[38] and extractions and acid/base titrations in liquid-liquid segmented flow.[24]

Finally, microfluidic reactors have been utilized as miniature chemical factories for the on-demand production of unstable or expensive reagents, such as bioradiological labels.[39]

2.4 MICROFLUIDIC REACTORS FOR NANOSCALE MATERIALS

The hypothesis of this dissertation research is that, by utilizing the unique capabilities of microscale reactors, we can tune and characterize the unique properties of nanoscale materials. Although there are a wide variety of nanoscale reactions, we use the case study of pyrolytic nanocrystal synthesis to discuss the advantages and disadvantages of microfluidics.

2.4.1 Advantages of microfluidic nanocrystal synthesis

Although nanoparticles can be synthesized with various materials, shapes, and properties, the control and understanding of such reactions is still rudimentary. Microfluidic reactors offer a method to reduce the variability in such reactions and characterize them systematically. The precise thermal, concentration, and temporal control of microreactors may provide avenues for refining existing nanocrystal syntheses and developing novel shapes and heterostructures.

In particular, microfluidic devices allow for the more reproducible injection and mixing of precursors compared to the violent and unpredictable injections used in pyrolytic nanocrystal syntheses. Such flask injections often lead to chaotic fluctuations in temperature and concentration, which can be avoided with the thermal and hydrodynamic stability of microreactors. Such control is attractive for nanocrystal growth because the nucleation rate is extremely sensitive to temperature and concentration.

In addition, growth conditions can be altered rapidly by the addition of new precursors from intersection channels or by flowing reactants through zones of different temperature. And unlike in bulk liquids, which take minutes to cool, reactions in microfluidic devices can be quenched rapidly by cooling or dilution to ensure precise reaction times.

Microfluidic reactors also allow for *in situ* or online characterization of the nanocrystal growth. Due to the optical size effects in semiconductor nanocrystals and metal nanoparticles, online spectra can be used to extract the size, size distribution, and even aspect ratio of particles in real time. The ability to quickly establish reaction conditions and characterize products allows reaction conditions to be screened and optimized rapidly

without needing to set up numerous flask reactions and generate large quantities of potentially toxic products, of which only a tiny amount is needed for characterization.

Because the rapid injection and mixing of precursors is a irreproducible but necessary procedure for the precise nucleation and monodisperse growth of nanocrystals, the industrial scale-up of traditional nanocrystal syntheses from ~25 mL flasks to 1 L batch reactors is not straightforward. While 40 flask reactions could be run in parallel, the nanocrystals from each batch could have different properties. On the other hand, a fully automated lab operating 20 identical microfluidic chips in parallel with 25 channels/chip, 20 hours/day at a rate of 100 μL of product/hour per channel could produce 1 L of solution of tightly controlled nanocrystals per day, which is comparable to the industrial output for many specialty chemicals.[40]

2.4.2 Challenges of nanoscale microreactors

While microfluidic reactors are attractive platforms for nanocrystal synthesis, such reactions present many challenges for integration in microfluidic devices. At the outset of this dissertation research, there were few reported studies relating to the use of nanoparticles in microfluidic devices, and none specifically pertaining to the microfluidic synthesis of nanoparticles.

A possible reason for this dearth of research is that the harsh conditions for high quality nanocrystal synthesis contrast dramatically with the mild temperatures and aqueous solutions typically used in microfluidic reactors. High quality nanocrystal synthesis requires

high temperatures (~300 °C) to ensure good crystallinity and requires volatile, pyrophoric, and caustic reagents to encourage rapid kinetics. In addition, traditional surfactants, such as tri-*n*-octylphosphine oxide, are solid at room temperature, and even when melted, their high viscosity results in large back pressures. As such, much of the expertise developed for microfluidic reactors is inapplicable to microfluidic nanocrystal synthesis.

In the next chapter we will discuss how we addressed these issues in the design of our microchips, apparatus, and experimental protocols.

2.5 REFERENCES

(1) Lagally, E. T.; Mathies, R. A. J. Phys. D-Appl. Phys. 2004, 37, R245.

(2) deMello, A. J. Nature 2006, 442, 394.

(3) Huang, L. R.; Cox, E. C.; Austin, R. H.; Sturm, J. C. Science 2004, 304, 987.

(4) Stone, H. A.; Stroock, A. D.; Ajdari, A. *Annu. Rev. Fluid Mech.* **2004**, *36*, 381.

(5) Welty, J. R.; Wicks, C. E.; Wilson, R. E. Fundamentals of Momentum, Heat, and Mass Transfer, 3rd ed.; Wiley: New York, 1984.

(6) Kamholz, A. E.; Weigl, B. H.; Finlayson, B. A.; Yager, P. Anal. Chem. 1999, 71, 5340.

(7) Pollack, L.; Tate, M. W.; Finnefrock, A. C.; Kalidas, C.; Trotter, S.; Darnton, N. C.; Lurio, L.; Austin, R. H.; Batt, C. A.; Gruner, S. M.; Mochrie, S. G. J. *Phys. Rev. Lett.* **2001**, *86*, 4962.

(8) Kenis, P. J. A.; Ismagilov, R. F.; Whitesides, G. M. *Science* **1999**, *285*, 83.

(9) Taylor, G. I. *Proc. R. Soc. London, A* **1953**, *219*, 186.

(10) Dutta, D.; Ramachandran, A.; Leighton, D. T. *Microfluid. Nanofluid.* **2006**, *2*, 275.

(11) Levenspiel, O. *The Chemical Reactor Omnibook*; OSU Book Stores: Corvallis, OR, 1979; Vol. 1.

(12) Beard, D. A. *J. Appl. Phys.* **2001**, *89*, 4667.

(13) Lagally, E. T.; Emrich, C. A.; Mathies, R. A. *Lab Chip* **2001**, *1*, 102.

(14) Grover, W. H.; Mathies, R. A. *Lab Chip* **2005**, *5*, 1033.

(15) Song, H.; Tice, J. D.; Ismagilov, R. F. *Angew. Chem. Int. Ed.* **2003**, *42*, 768.

(16) Gunther, A.; Khan, S. A.; Thalmann, M.; Trachsel, F.; Jensen, K. F. *Lab Chip* **2004**, *4*, 278.

(17) Viskari, P. J.; Landers, J. P. *Electrophoresis* **2006**, *27*, 1797.

(18) Willauer, H. D.; Collins, G. E. *Electrophoresis* **2003**, *24*, 2193.

(19) Trumbull, J. D.; Glasgow, I. K.; Beebe, D. J.; Magin, R. L. *IEEE Trans. Biomed. Eng.* **2000**, *47*, 3.

(20) Emrich, C. A.; Tian, H. J.; Medintz, I. L.; Mathies, R. A. *Anal. Chem.* **2002**, *74*, 5076.

(21) Shi, Y. N.; Simpson, P. C.; Scherer, J. R.; Wexler, D.; Skibola, C.; Smith, M. T.; Mathies, R. A. *Anal. Chem.* **1999**, *71*, 5354.

(22) Haswell, S. J.; Watts, P. *Green Chem.* **2003**, *5*, 240.

(23) Janasek, D.; Franzke, J.; Manz, A. *Nature* **2006**, *442*, 374.

(24) Burns, J. R.; Ramshaw, C. *Lab Chip* **2001**, *1*, 10.

(25) Paegel, B. M.; Blazej, R. G.; Mathies, R. A. *Curr. Opin. Biotechnol.* **2003**, *14*, 42.

(26) Lagally, E. T.; Scherer, J. R.; Blazej, R. G.; Toriello, N. M.; Diep, B. A.; Ramchandani, M.; Sensabaugh, G. F.; Riley, L. W.; Mathies, R. A. *Anal. Chem.* **2004**, *76*, 3162.

(27) Skelley, A. M.; Scherer, J. R.; Aubrey, A. D.; Grover, W. H.; Ivester, R. H. C.; Ehrenfreund, P.; Grunthaner, F. J.; Bada, J. L.; Mathies, R. A. *Proc. Natl. Acad. Sci. U. S. A.* **2005**, *102*, 1041.

(28) Paegel, B. M.; Yeung, S. H. I.; Mathies, R. A. *Anal. Chem.* **2002**, *74*, 5092.

(29) Haswell, S. J.; Middleton, R. J.; O'Sullivan, B.; Skelton, V.; Watts, P.; Styring, P. *Chem. Commun.* **2001**, 391.

(30) Dubois, P.; Marchand, G.; Fouillet, Y.; Berthier, J.; Douki, T.; Hassine, F.; Gmouh, S.; Vaultier, M. *Anal. Chem.* **2006**, *78*, 4909.

(31) Watts, P.; Wiles, C.; Haswell, S. J.; Pombo-Villar, E. *Tetrahedron* **2002**, *58*, 5427.

(32) Wiles, C.; Watts, P.; Haswell, S. J.; Pombo-Villar, E. *Lab Chip* **2001**, *1*, 100.

(33) Skelton, V.; Greenway, G. M.; Haswell, S. J.; Styring, P.; Morgan, D. O.; Warrington, B. H.; Wong, S. Y. F. *Analyst* **2001**, *126*, 11.

(34) Mikami, K.; Yamanaka, M.; Islam, M. N.; Tonoi, T.; Itoh, Y.; Shinoda, M.; Kudo, K. *J. Fluorine Chem.* **2006**, *127*, 592.

(35) Greenway, G. M.; Haswell, S. J.; Morgan, D. O.; Skelton, V.; Styring, P. *Sens. Actuator. B-Chem.* **2000**, *63*, 153.

(36) Pennemann, H.; Watts, P.; Haswell, S. J.; Hessel, V.; Lowe, H. *Org. Process Res. Dev.* **2004**, *8*, 422.

(37) de Mas, N.; Gunther, A.; Schmidt, M. A.; Jensen, K. F. *Ind. Eng. Chem. Res.* **2003**, *42*, 698.

(38) Srinivasan, R.; Hsing, I. M.; Berger, P. E.; Jensen, K. F.; Firebaugh, S. L.; Schmidt, M. A.; Harold, M. P.; Lerou, J. J.; Ryley, J. F. *AIChE J.* **1997**, *43*, 3059.

(39) Lee, C. C.; Sui, G. D.; Elizarov, A.; Shu, C. Y. J.; Shin, Y. S.; Dooley, A. N.; Huang, J.; Daridon, A.; Wyatt, P.; Stout, D.; Kolb, H. C.; Witte, O. N.; Satyamurthy, N.; Heath, J. R.; Phelps, M. E.; Quake, S. R.; Tseng, H. R. *Science* **2005**, *310*, 1793.

(40) deMello, J.; deMello, A. *Lab Chip* **2004**, *4*, 11N.

Chapter 3 Microfabrication and Experimental Protocols

3.1 INTRODUCTION

While microfluidic reactors have been demonstrated for a variety of chemical and biological systems, designing a microreactor for performing nanocrystal reactions poses unique challenges. Nanocrystal syntheses frequently use caustic reagents, organic solvents, solid surfactants, and high temperatures. Consequently, much microfluidic technology, such as soft lithography, elastomer valves, and electro-osmotic pumping, is not immediately transferable to microscale nanocrystal synthesis. In this chapter, we describe the design decisions, microfabrication techniques, and experimental protocols that were essential for performing nanocrystal reactions in microfluidic reactors.

3.2 SUBSTRATES

Microfluidic reactors can be fabricated using standard clean room photolithographic techniques on inorganic substrates such as silicon and glass, by molding elastomers such as polydimethylsiloxane (PDMS), by micromachining polymers such as polycarbonate, and even by patterning channels out of thick photoresist. The substrate choice determines geometrical limitations such as wall angle, aspect ratio, and resolution as well as the mechanical and chemical resistance of the microreactor.

Most similar to the flasks used for traditional reactions, glass was chosen as the substrate for nanocrystal synthesis due to its thermal, mechanical, and chemical stability.

Unlike polymer substrates, glass microchips are chemically resistant, withstand high temperatures and large thermal gradients, and will not leak or deform at high pressure. Unlike silicon, glass is inexpensive to purchase and process, etches cleanly and rapidly, and is straightforward to drill. In addition, glass is a thermal and electrical insulator, simplifying the isolation of temperature zones and electrical heater elements. Finally, borofloat glass is valuable for *in situ* visual and spectroscopic characterization because it is optically transparent down to the near-ultraviolet region (350 nm), and features very little autofluorescence. Taking advantage of these properties, the Mathies group has developed a large amount of expertise in the fabrication of glass microchips.[1,2]

Microfluidic devices are fabricated from a wide variety of glasses, including borofloat, Pyrex 7740, D263, and soda lime. These glasses differ in their chemical composition and processing, both of which determine the physical properties of the materials. For example, borofloat and Pyrex 7740 both consist of 81% SiO_2, 13% B_2O_3, 4% Na_2O/K_2O, and 2% Al_2O_3.[3] The high concentration of B_2O_3 gives these borosilicate glasses a large resistance to thermal shock, one of the reasons why Pyrex is used for chemical glassware. Borofloat and Pyrex differ mainly in their processing and surface properties. Sheets of borofloat are formed by floating the glass melt on molten tin, resulting in intrinsically smooth surfaces that have slight metal contamination.[3] In contrast, Pyrex is more homogeneous in composition because it is formed by rolling and casting, but subsequent polishing leaves surfaces more strained, resulting in less uniform etching. Due to its smoother channel etching, we chose to use the less expensive borofloat for nanocrystal synthesis microreactors.

3.3 BASIC GLASS MICROFABRICATION

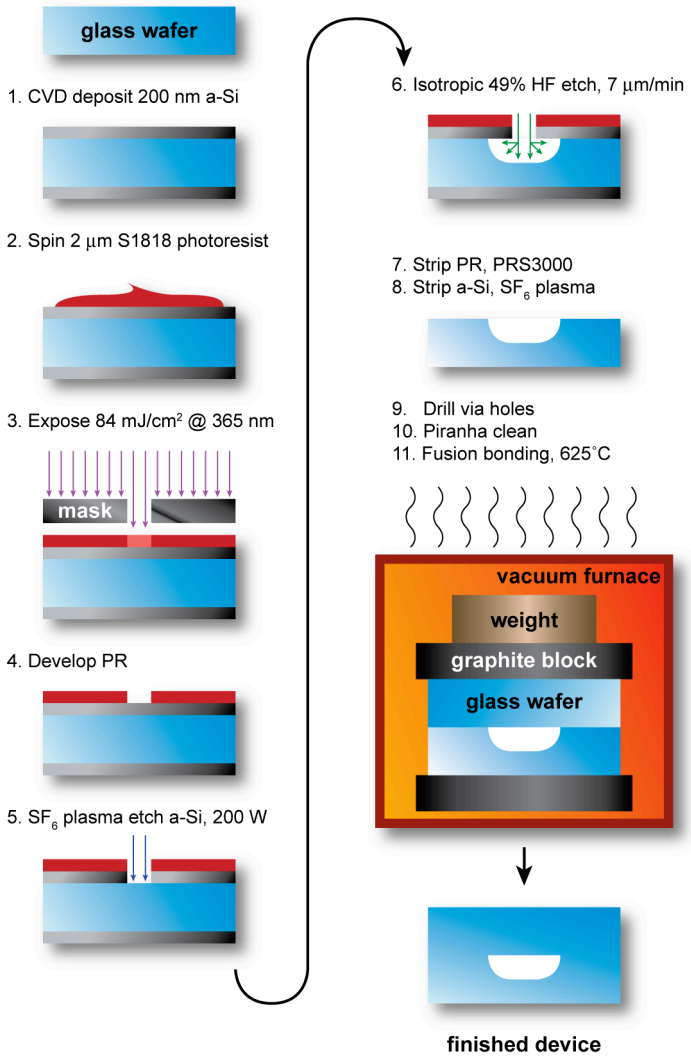

Figure 3.1. Basic glass microchip fabrication process flow.

Glass microfluidic reactors are fabricated in the UC Berkeley Microfabrication Laboratory according to the process flow shown in Figure 3.1 and following detailed protocols that can be found in the Mathies lab protocols website.[4]

A layer of amorphous silicon (*a*-Si) is deposited on the surface of 1.1 mm-thick glass wafers via low pressure chemical vapor deposition (LP-CVD) at 300 mTorr and 525 °C with 100 sccm SiH_4. Borofloat glass (Precision Glass & Optical) was used predominantly, although D263 (PG&O) and Pyrex 7740 (Alpha Precision) have also been tested. Shipley S1818 photoresist is spun to 2 μm-thickness on the Si-coated glass wafers and soft-baked at 120 °C. The photoresist is exposed through a chrome mask on a commercial mask aligner with a dose of 84 mJ/cm^2 at 365 nm (I-line). The channel pattern in the photoresist is transferred to the *a*-Si film by etching the Si film with a 200 W SF_6 plasma. The glass is then isotropically etched through the *a*-Si hard mask with 49% HF to a depth of ~50 microns at a rate of ~7 microns/min. Etching glass with HF results in isotropically etched, "D"-shaped channels that laterally undercut the a-Si layer and the photoresist by a distance equal to the etch depth. Because undercut photoresist has poor mechanical stability and adheres poorly to glass, the more resilient *a*-Si hard mask is used to retain smooth channel walls during HF etching.

After stripping the photoresist in a PRS3000 bath and removing the *a*-Si hard mask with the SF_6 plasma, the chip is prepared for drilling by bonding it at 200 °C to a dummy wafer using a thin layer of pine resin. Fluidic access holes (diameter = 500 μm) and thermocouple wells are mechanically drilled according to the pattern specified by an AutoCAD DXF file using a computer-controlled CNC mill equipped with diamond drill bits (Amplex). The pine resin is removed with acetone, and the wafers are cleaned in a 120 °C piranha bath immediately prior to bonding to a plain borofloat wafer. Wafers are thermally

bonded between two polished graphite blocks and underneath a ~5 kg stainless steel weight in a vacuum furnace for 6 h at a temperature slightly above the annealing point of the glass (625 °C for borofloat). This fabrication and bonding procedure results in a single, monolithic glass chip with buried channels and no voids.

3.4 CHANNEL SURFACE PASSIVATION

Channel surface modification is performed in certain microchips in order to passivate or alter the wetting properties of the reactor walls. The glass surface of the microreactor channels is silanized with 1H,1H,2H,2H-perfluorodecyltrichlorosilane (FDTS, Lancaster) based on a procedure published by Srinivasan, *et al.*[5] The stability and effectiveness of this silane coating at high temperatures is especially sensitive to deviations from the following silanization procedure. After bonding, microchannels are cleaned and oxidized with piranha (3:1 vol/vol H_2SO_4/H_2O_2) at 80 °C, then rinsed sequentially with Millipore water, isopropanol, and isooctane, and dried with a stream of filtered nitrogen. The silanization is performed under argon atmosphere, because FDTS reacts readily with water to form insoluble sol-gel aggregates. In a glovebox, 1.5 mL of a 0.66 mM FDTS/isooctane solution is pumped through the channels over the course of 1 hour. The channels are then rinsed with isooctane, isopropanol, and water, then purged with nitrogen. Finally, the surface of the channels was dehydrated in a 120 °C oven for 12 h in order to drive cross-linking between adjacent siloxyl groups. Flat borofloat substrates silanized using this procedure have typical static water/air contact angles of 115° as measured by a Kruss Contact Angle Measuring System.

Contact angle experiments and microreactor syntheses demonstrated that, while the contact angle of the FDTS coating decreases steadily when exposed to organic solvents at high temperature, it retains its hydrophobicity for up to 4 h at 260 °C if silanization procedures are performed properly. The presence of surface water, which promotes silane cross-linking, was found to be a critical component in the stability of the FDTS coating. Exposing the coating to fluorinated solvents at temperatures ≥ 290 °C was found to rapidly degrade the contact angle, possibly due to the evolution of HF as decomposition product or due to the less stable, unfluorinated C_1-C_2 bond in the silane.

3.5 TEMPERATURE CONTROL

Three types of heaters can be used to heat the reaction channels: (1) a macroscopic aluminum block fitted with cartridge heaters, (2) a thin film Kapton heater (Minco), and (3) aluminum thin film heaters microfabricated directly on the glass chips. Microfabricated heaters heat the substrate by Joule heating, where the thermal power dissipated is $P = V^2/R$, where V is the input voltage, and R is the heater resistance. Microfabricated heaters are superior to the Kapton and block heaters due to the microheaters' low power requirements, precise local heating, and intimate thermal contact with the glass substrate.

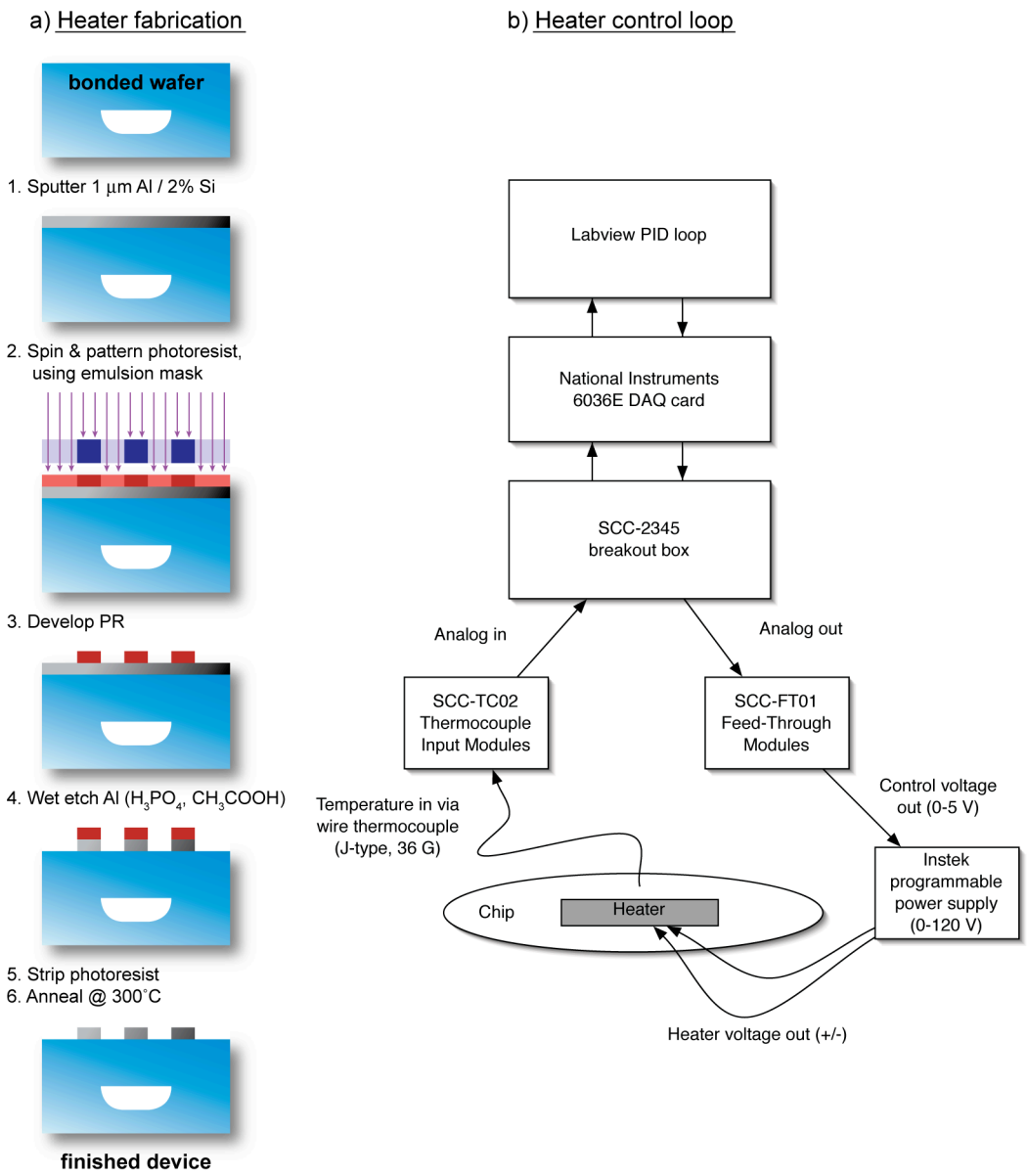

Figure 3.2. Microfabricated heater process flow and control loop diagram

3.5.1 Microheater fabrication

Microheaters are fabricated from Al films rather than the more traditional Ti/Pt films[6] because aluminum has substantially lower resistance and is more convenient to deposit and etch. Since aluminum is low-melting, relatively soft, and easily oxidized, Al microheaters are fabricated on glass microchips after they have been thermally bonded, as shown in the process flow in Figure 3.2a. Using a DC magnetron sputterer (CPA, 3 kW, 8 mTorr, 140 sccm Ar), a ~1-μm film of aluminum with 2% silicon (Al / 2% Si) is deposited onto the back side of the piranha-cleaned wafers, whose surfaces are slightly rough (~200 nm) due to the imprinting from the polished graphite blocks used for bonding. Microfabricated resistive heater geometries are lithographically patterned into 2 μm-thick S1818 photoresist using an emulsion mask, and the metal film is patterned by wet etching for 5 minutes at 50 °C in commercially available aluminum etchant (phosphoric acid, acetic acid, and surfactant). Chips are then mechanically diced, and the channels are flushed with acetone, isopropanol, and water to clean out any debris from the previous fabrication steps. Finally, the microfabricated heaters are annealed in air overnight (~12 h) in a 300 °C oven, which reduces their resistance (5-100 Ω) by as much as 20% while increasing their stability and uniformity by relieving strain and preemptively oxidizing the surface.

3.5.2 Heater control

As shown in Figure 3.2b, the microfabricated, Kapton, and block heaters are controlled via a computer-controlled PID (Proportional, Integral, Differential) loop consisting of thermocouples, the master LabView program, and several programmable power supplies.

Temperatures over the chip are recorded using up to 12 separate thermocouple wires (J type, 36 G, Omega) that are imbedded into silicone thermal paste-filled holes (500 μm-diameter) drilled to channel depth. The thermocouples are connected to the analog inputs of a National Instruments data acquisition (DAQ) card. Using the LabView PID toolkit, the temperatures are converted to the appropriate control voltages, which vary with time according to the differential between the set and measured temperatures. Because the DAQ cards do not have enough current or voltage range to power the heaters, these control voltages are transmitted through the analog outputs of two DAQ cards to a maximum of four corresponding power supplies. A combination of custom-built and commercially available power supplies (Instek) are configured to output voltages proportional to the control voltages. To maintain reaction temperatures at ~300 °C, small Al heaters (10 Ω, 1 cm^2 area) typically require ~10 W (10 V @ 1 A), while large heaters (100 Ω, ~20 cm^2 area) require ~100 W (100V @ 1A). The power supplies are connected to the chips using copper wiring and either alligator clips or custom-machined clamps with spring-loaded gold-plated "pogo" pins. Using the control loop in this manner, the power to the microheaters can be adjusted nearly instantaneously (~100 ms), resulting in excellent thermal stability (±1 °C) and responsiveness.

3.6 EXPERIMENTAL SCHEME & APPARATUS

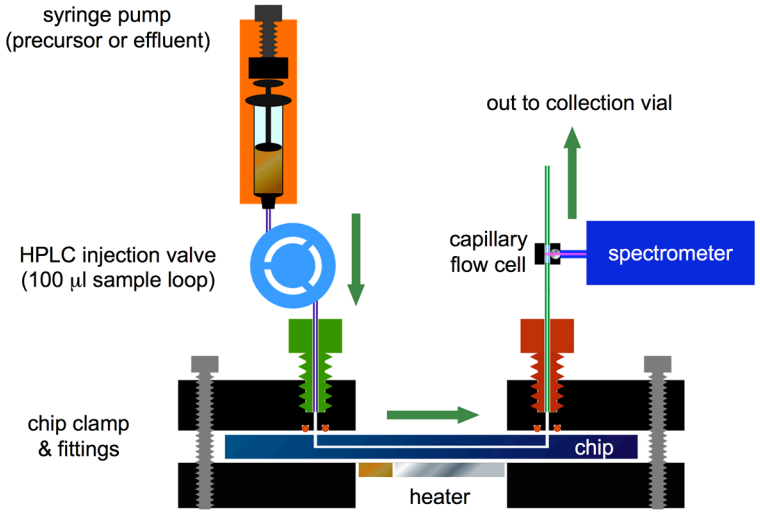

Figure 3.3. Schematic of the external apparatus and chip-to-world interface. Precursor loaded in the injection valve is pumped into the chip via PEEK HPLC tubing and fittings. The external tubing is connected to the chip via an aluminum screw clamp and silicone O-rings. The heaters induce the pyrolytic synthesis of nanocrystals, which flow out of the chip into a capillary flow cell connected to absorption or fluorescence spectrometers. The product is then collected in a vial under nitrogen.

Figure 3.3 illustrates the complete apparatus used to perform, monitor, and control on-chip nanocrystal synthesis. The different experiments described in the following chapters use variations on this general experimental scheme.

Before experiments, all solutions are degassed to prevent bubbles and clogging, respectively. In a typical experiment, the Cd and Se stock solutions are dispensed into 500 µL Hamilton gastight syringes and pumped with individual Harvard Apparatus PHD2000 and Pump 11 syringe pumps. Alternatively, the stock solutions can be loaded into the 100 µL sample loop of a stainless steel HPLC injection valve, and pure octadecene effluent is

used to pump the plug into the chip. The flowing of reactant plugs was observed to reduce clogging, sample volume, and allowed for the heating of precursors. Pumping and all other chip functions are computer-controlled through a master LabView (National Instruments) virtual instrument.

A custom-built PEEK or aluminum manifold is used to interface the glass chip with PEEK tubing and fittings (Upchurch) that deliver reaction solutions from the injection valve and syringes. The manifold was machined with tapped holes corresponding to the outlets on the chip and is mechanically clamped on the chip using screws. PEEK fittings (Upchurch) on the ends of the 0.020" inner-diameter, 1/16" outer-diameter PEEK tubing are screwed into these ports. A small portion of the tubing extended beyond the PEEK ferrule, and a Dash#002 silicone or Viton O-ring (McMaster Carr) is fitted on the end. When the fitting is screwed down flush to the chip, the O-ring compresses to form a tight seal. Although the silicone O-rings are less chemically resistant than Viton and tend to swell over time, their lower durometer produces better seals with less normal force, as long as fresh silicone O-rings are used for every set of experiments. This reversible combination of mechanical clamping and O-ring seals has proven to be more convenient and more thermally, chemically, and mechanically robust than epoxy or solder-based interfacing methods, such as Upchurch's Nanoport fittings.

The reaction channels are heated from below using the heaters and control loop described in Section 3.4. As the reactants are injected into the heated microchannels, the precursors decompose and react to form nanocrystals. The product solution is output into a short length of 0.010"-diameter PEEK tubing, which interfaces with a 20-cm length of 250 um-inner-diameter fused silica capillary (PolyMicro), which leads into a custom-built spectral flow cell. Light from an UV LED lamp (380 nm, Ocean Optics LS-450) is passed through a

bifurcated fiber optic assembly and focused by a ball lens onto a portion of the capillary where the polyimide cladding has been thermally stripped. Nanocrystal fluorescence is collected with the same ball lens-fiber optic assembly and is detected with a CCD spectrometer (USB-2000, Ocean Optics). The reaction product is collected from the end of the capillary in septa-capped vial under constant nitrogen flow.

3.7 REFERENCES

(1) Grover, W. H.; Ivester, R. H. C.; Jensen, E. C.; Mathies, R. A. *Lab Chip* **2006**, *6*, 623.

(2) Simpson, P. C.; Roach, D.; Woolley, A. T.; Thorsen, T.; Johnston, R.; Sensabaugh, G. F.; Mathies, R. A. *Proc. Natl. Acad. Sci. U. S. A.* **1998**, *95*, 2256.

(3) *Schott Borofloat product properties.* http://www.us.schott.com/hometech/english/products/borofloat/attribute/ (accessed on 10/23/2006).

(4) Ivester, R. H. C.; Grover, W. H.; Emrich, C. A.; Mathies, R. A. *Mathies Lab Protocols Website.* http://zinc.cchem.berkeley.edu/protocols/ (accessed on 10/10/2006).

(5) Srinivasan, U.; Houston, M. R.; Howe, R. T.; Maboudian, R. *J. Microelectromech. Syst.* **1998**, *7*, 252.

(6) Lagally, E. T.; Emrich, C. A.; Mathies, R. A. *Lab Chip* **2001**, *1*, 102.

Chapter 4 Size-Controlled Growth of CdSe Nanocrystals in Microfluidic Reactors

4.1 INTRODUCTION

Nanocrystals exhibit a variety of size- and shape-dependent physical and chemical properties that present a unique opportunity for creating materials with tailored characteristics.[1] Synthesizing such nanostructures poses a significant challenge, since robust methods for preparing ensembles of nanoparticles of homogeneous and predictable size and shape are required. Current synthetic methods rely on a convoluted interplay of kinetic and thermodynamic factors. The most successful and widely adopted nanocrystal syntheses involve rapid nucleation by injection of a precursor into a hot bulk liquid, followed by growth at a lower temperature in the presence of stabilizing surfactants.[1] Specifying the precise conditions of such reactions is difficult, as the kinetics depend on such details as the rate and volume of precursor injection, the dimensions of the flask, and the rate of mixing.[2] Here we demonstrate an alternate synthetic approach, based upon microfluidics, that promises to yield more precise and sophisticated control over nanocrystal growth parameters and kinetics.

The intrinsic advantage of microfluidic reaction systems[3,4] is that temperature and concentration can be changed rapidly and reproducibly on the scale of micrometers and

milliseconds, as desired for nanocrystal synthesis. Microfluidic approaches have been employed to perform a variety of chemical processes, including organic syntheses, biochemical reactions, and heterogeneous catalysis.[5] Recently, several experiments have investigated the applicability of controlling nanoparticle growth in microchannel reactors by adjusting flow parameters. CdS and TiO_2 nanoparticles have been synthesized at room temperature using micromixers[6] and insoluble phase interfaces[7] in microchannels. In addition, CdSe nanoparticles of more definite crystallinity have been synthesized in capillary tubing[8] using high temperatures and surfactants similar to those used for pyrolytic preparations in bulk solutions. Chip-based microreactors, however, are advantageous since microfabricated systems can be designed to make rapid and complex changes in reaction conditions while retaining superior scalability.

In this study, we demonstrate the use of microfabricated chip-based reactors for the continuous, high-temperature synthesis, control, and characterization of high-quality CdSe nanocrystals. While previous studies relied on the manual characterization of sample aliquots, we focus on the model CdSe system because the strong and well-calibrated size dependence of CdSe nanocrystals' luminescence energy allows for rapid on-line spectroscopic analysis and sizing.

4.2 EXPERIMENTAL

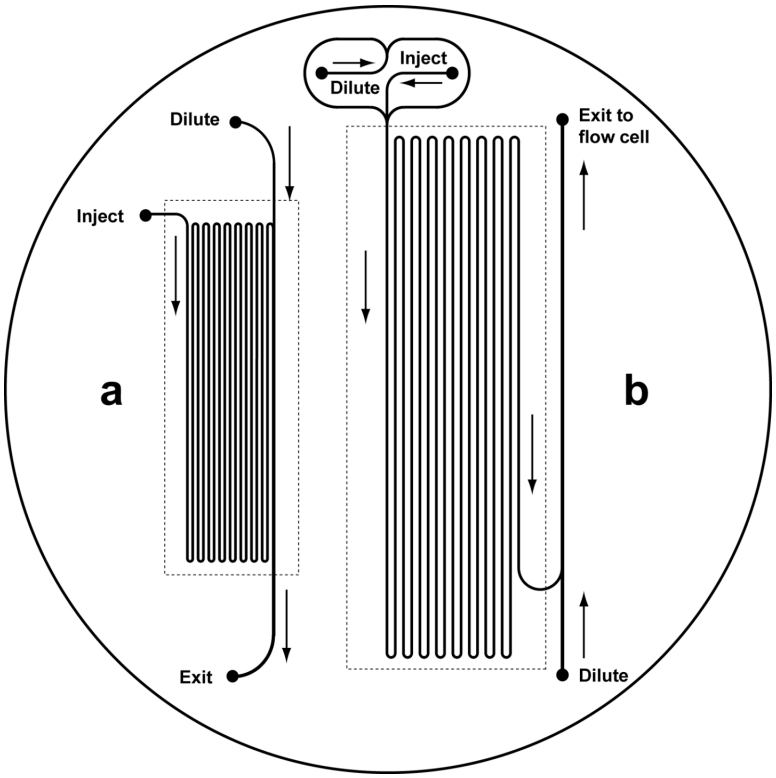

Figure 4.1. Schematic of microreactor channels in a 100 mm-diameter glass wafer sandwich. Dotted lines indicate boundaries of heated reactor regions. Filled circles represent vias drilled for access to the channels. Precursor enters through the inject vias and can (a) react directly in a serpentine 65 cm-long, 150 μm-wide, 47 μm-deep, 4.7-μl channel, or (b) be diluted before reacting in a 105 cm-long, 200 μm-wide, 57 μm-deep, 12.5-μl channel. Nanocrystal product is diluted and quenched before exiting to a capillary flow cell.

Two types of microreactors (Figure 4.1) were isotropically etched into borosilicate glass wafers using standard microfabrication techniques and enclosed by thermally bonding blank wafers onto the etched surfaces.[9] We synthesized CdSe nanocrystals by flowing a 100 μl plug of precursor[10] through a heated microreactor channel using syringe-pumped octadecene (ODE).[11,12]

The precursor was prepared by slowly adding 0.3 ml of stock solution [2:5:100 Se:$Cd(CH_3)_2$:tributylphosphine molar ratio] to a surfactant mixture containing 1.1 g dodecylamine, 0.7 g tri-octylphosphine oxide, and 0.6 g 1-octadecene (ODE) at 60 °C in an N_2-filled flask. After degassing under vacuum for 2 hr, the stock/surfactant precursor mixture was loaded into the 100 μl sample loop of an HPLC injection valve.

A syringe pump filled with ODE (typical flow rate = 2 μl/min) injected the precursor plug into the chip, after which a second ODE pump optionally diluted the plug before it entered the main reaction channel. The precursor plug reacted to form CdSe nanocrystals as it flowed continuously through the reaction channel, which was heated from below using a silicone heater. Typical reaction temperatures of 180 ± 0.5 °C were measured by embedding a thermocouple into a hole drilled to microchannel depth. After a typical reaction time of 300 s, a third ODE syringe pump was used to dilute the nanocrystal solution and pump it into an external fused silica capillary flow cell, where fluorescence spectra (370 nm excitation) were measured continuously using a fiber optic CCD spectrometer approximately 110 s after the nanocrystals exited the heated reaction channel. Photoluminescence (PL) peaks provided a method for sizing synthesized nanocrystals, because quantum confinement effects dictate that peak wavelength (λ_{max}) and full width at half maximum intensity (FWHM) increase monotonically with nanocrystal diameter and size distribution, respectively.[1]

4.3 RESULTS & DISCUSSION

In a typical experiment, narrow fluorescence peaks characteristic of CdSe nanocrystals were observed when the front of the nanocrystal plug passed through the microreactor and into the flow cell. The use of plug volumes much larger than reactor volumes allowed λ_{max} and FWHM values to stabilize 2000 seconds after flow was initiated. After equilibration, λ_{max} values were stable within ±0.5 nm over a given plug and reproducible within ±1 nm across different plugs. The stabilized FWHM values, observed as low as 28 nm, were comparable to those for nanocrystals synthesized in an equivalent flask reaction. Such data indicate that microreactors are able to continuously and reproducibly synthesize nanocrystals of good quality and size distribution, allowing reaction conditions to be varied precisely within a single plug. Here we demonstrate the tuning of CdSe nanocrystal size in microreactors as a function of temperature, flow rate, and precursor concentration.

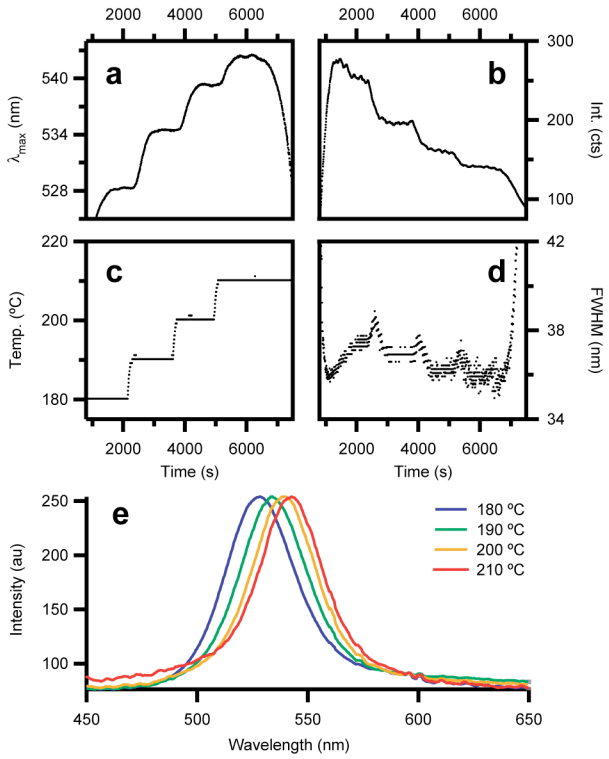

Figure 4.2. Size control of nanocrystal synthesis via temperature. Continuous fluorescence traces recorded vs. time demonstrate the use of a 4.7-μl reactor (Figure 4.1a) to grow nanocrystals of four different sizes at four different temperatures and a flow rate of 1.0 μl/min. Above curves represent (a) peak emission wavelength, (b) peak intensity, (c) reaction temperature, and (d) peak width at half maximum intensity as a single reactant plug passes through the flow cell at the end of the reactor. (e) Normalized fluorescence spectra are shown for each temperature, corresponding to 2102, 3135, 4807, and 6121 s.

Figure 4.2 illustrates four different sizes of nanocrystals of increasing average diameter (2.44, 2.54, 2.64, and 2.69 ± 0.06 nm)[13] that were synthesized by increasing the temperature in 10 °C increments from 180 to 210 °C. The direct correlation between temperature and increased size is supported by the distinct steps in λ_{max} and intensity, as well as by the peaks in FWHM during size transitions. These data agree with temperature-dependent kinetic studies and also indicate greater focusing of size distribution at higher temperature. The decrease in intensity with increasing temperature could be attributed to the same amount of monomer forming a smaller concentration of larger nanocrystals.

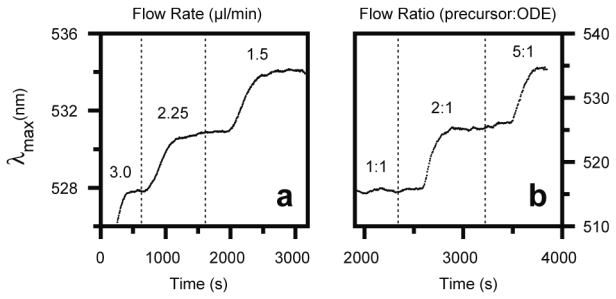

Figure 4.3. Size control of nanocrystal synthesis via flow rate and concentration. Continuous fluorescence data demonstrate the use of the 12.5-µl reactor (Figure 4.1b) to grow three different nanocrystal sizes by varying flow rate and initial precursor concentration. (a) Peak emission wavelength for total flow rates of 3.0, 2.25, and 1.5 µl/min with constant 2:1 precursor:octadecene (ODE) flow ratio at 190 °C. (b) Peak emission wavelength for 1:1, 2:1, and 5:1 precursor:ODE flow ratios with constant total flow rate of 3.0 µl/min at 180 °C reaction temperature.

A second kinetic parameter, reaction time, was controlled in the microreactor via flow rate. Figure 4.3a illustrates the growth of three sets of nanocrystals of increasing λ_{max} and diameter (2.43, 2.48, and 2.54 ± 0.06 nm) synthesized as the flow rate was decreased and residence times in the heated reaction zone increased to 250, 333, and 500 seconds, respectively. The limited growth after 250 second residence times is characteristic of the slow kinetics observed after monomers have been depleted by incorporation into nanocrystals.[2,14] While reaction time can be controlled by varying overall flow rate, initial precursor concentration can be controlled by varying relative flow rates of the precursor and ODE in a mixing microreactor (Figure 4.1b). Since flow in these microchannels is laminar, precursor solution will initially flow inside a sheath of ODE fluid without convective mixing. Due to short characteristic diffusion times (< 1 s), precursor is diluted less than 3 mm after entering the heated reaction zone.[4,15] As shown in Figure 4.3b, microreactor syntheses applying such mixing in precursor:ODE flow rate ratios of 1:1, 2:1, and 5:1 with constant total flow rate

resulted in nanocrystal diameters of 2.23, 2.39, and 2.55 ± 0.06 nm, respectively. The increasing growth rates with concentration indicate clearly concentration-dependent kinetics.

4.4 CONCLUSION

In summary, chip-based microfluidic reactors were used to control the high-temperature growth of CdSe nanocrystals on three independent levels – reaction time, temperature, and precursor concentration. While similar data could have been collected through a tedious series of flask syntheses, microreactor results highlight the flexibility of such microfluidic systems for efficiently collecting kinetic data and fine-tuning desired physical properties. More significantly, these chip-based experiments lay the foundation for future experiments that would be macroscopically infeasible. For example, microscopic control of temperature, concentration and flow could be utilized to fine-tune anisotropic shapes[16] and distinctly separate nanocrystal nucleation and growth.[1] In conjunction with recent advances in nanocrystal synthesis,[17] such lab-on-a-chip technology allows for rapid, cost-effective, and environmentally-friendly prototyping that will accelerate the rational development and production of novel nanostructures.

4.5 REFERENCES

(1) Murray, C. B.; Kagan, C. R.; Bawendi, M. G. *Annu. Rev. Mater. Sci.* **2000**, *30*, 545-610, and references therein.

(2) Dushkin, C. D.; Saita, S.; Yoshie, K.; Yamaguchi, Y. *Adv. Colloid Interface Sci.* **2000**, *88*, 37-78.

(3) Lagally, E. T.; Emrich, C. A.; Mathies, R. A. *Lab on a Chip* **2001**, *1*, 102-107.

(4) Erbacher, C.; Bessoth, F. G.; Busch, M.; Verpoorte, E.; Manz, A. *Mikrochim. Acta* **1999**, *131*, 19-24.

(5) Jensen, K. F. *Chem. Eng. Sci.* **2001**, *56*, 293-303, and refs. therein.

(6) Edel, J. B.; Fortt, R.; deMello, J. C.; deMello, A. J. *Chem. Commun.* **2002**, 1136-1137.

(7) Wang, H. Z.; Nakamura, H.; Uehara, M.; Miyazaki, M.; Maeda, H. *Chem. Commun.* **2002**, 1462-1463.

(8) Nakamura, H.; Yamaguchi, Y.; Miyazaki, M.; Uehara, M.; Maeda, H.; Mulvaney, P. *Chem. Lett.* **2002**, 1072-1073.

(9) Simpson, P. C.; Roach, D.; Woolley, A. T.; Thorsen, T.; Johnston, R.; Sensabaugh, G. F.; Mathies, R. A. *Proc. Natl. Acad. Sci. U. S. A.* **1998**, *95*, 2256-2261.

(10) Since the plug volume is much greater than the reactor volume, flow can be assumed to be continuous for the large majority of the plug.

(11) Qu, L.; Peng, Z. A.; Peng, X. *Nano Lett.* **2001**, *1*, 333-337.

(12) Yu, W. W.; Peng, X. *Angew. Chem. Int. Ed.* **2002**, *41*, 2368-2371.

(13) Diameters and uncertainties were determined from empirical sizing functions based on exponential fits of TEM and PL measurements from Ref. 14.

(14) Peng, X. G.; Wickham, J.; Alivisatos, A. P. *J. Am. Chem. Soc.* **1998**, *120*, 5343-5344.

(15) Characteristic diffusion times were calculated by assuming precursor complex Stokes radii of 1 nm and using a 1:1 precursor:ODE flow ratio with total flow rate of 3 μl/min.

(16) Manna, L.; Scher, E. C.; Alivisatos, A. P. *J. Am. Chem. Soc.* **2000**, *122*, 12700-12706.

(17) Reiss, P.; Bleuse, J.; Pron, A. *Nano Lett.* **2002**, *2*, 781-784.

Chapter 5 Shape Control of Nanoparticles in Continuous Flow Microreactors

5.1 INTRODUCTION

After demonstrating the size-controlled growth of spherical CdSe nanocrystals in microreactors, I modified my devices and procedures to synthesize nanoparticles of different materials and different shapes. The motivation for studying and synthesizing anisotropic nanocrystals lies in their anisotropic physical properties. Anisotropic shapes have lower symmetry and therefore have wide appeal for applications in which orientation or self-alignment is desirable. Rod-shaped nanoparticles[1] can align to form liquid crystals,[2] while tetrapods[3,4] – particles in which four rod-shaped arms extend from a central core with tetrahedral symmetry – naturally orient one arm normal to the surface upon which they are deposited. Such self-alignment may be valuable for directing the conduction of carriers in photovoltaic cells,[5,6] nanoscale wires, and transistors.[7,8] Nanorods also absorb and emit polarized light[9] and exhibit reduced electron-hole overlap.[10] Due to their higher surface area:volume ratio (SA:V) with respect to spheres, anisotropic nanocrystals have different thermodynamic properties, as seen in their surface chemistry,[11] melting,[12] and phase transitions.[13]

The growth of anisotropic shapes presents a synthetic challenge that encourages a more fundamental understanding of crystal growth. Since nanoparticles ultimately equilibrate into rounded spheroids to minimize surface energy, the growth of highly anisotropic or low-symmetry shapes requires a deeper knowledge of the complex interplay between kinetically- and thermodynamically driven growth. Coupled with the fact that synthetic parameters for

anisotropic crystals are less optimized than their spherical counterparts, these large gaps in the understanding of anisotropic growth mechanisms are issues that could be addressed through the use of microfluidic reactors.

Microfluidic devices are particularly intriguing tools for shape control because such reactors can rapidly alter shape-determining nucleation and phase-determining parameters such as temperature and concentration. A far-reaching goal of such microfluidic devices would be to use such advantages to synthesize shapes that are difficult or impossible to grow in bulk fluids.

5.1.1 Examples of anisotropic nanocrystal synthesis

General theory of shape control

The shape of crystals traditionally has been described in thermodynamic terms by Wulff's theorem, which states that, at equilibrium, the distance of a crystal face from a particle's center of mass is proportional to the surface energy of that face.[14] The lowest-energy crystal faces are stabilized, with the high-energy faces either eroding or growing until they eliminate themselves. For the zinc blende phase of CdSe (Figure 5.1c), the {111} faces are the most stable because they are close-packed planes and feature only one dangling bond per atom.

Nanoparticles, however, are inherently far from equilibrium, and shapes created by rapid nucleation and growth may not be described adequately by Wulff constructions. Nano-sized colloids feature truncated corners and equilibrate into "spherical" dots in order to minimize surface energy. In order to form anisotropic crystals via kinetic control, a method

to promote preferential monomer addition to the desired growth faces must be combined with methods to discourage relaxation to equilibrium states.

Rods

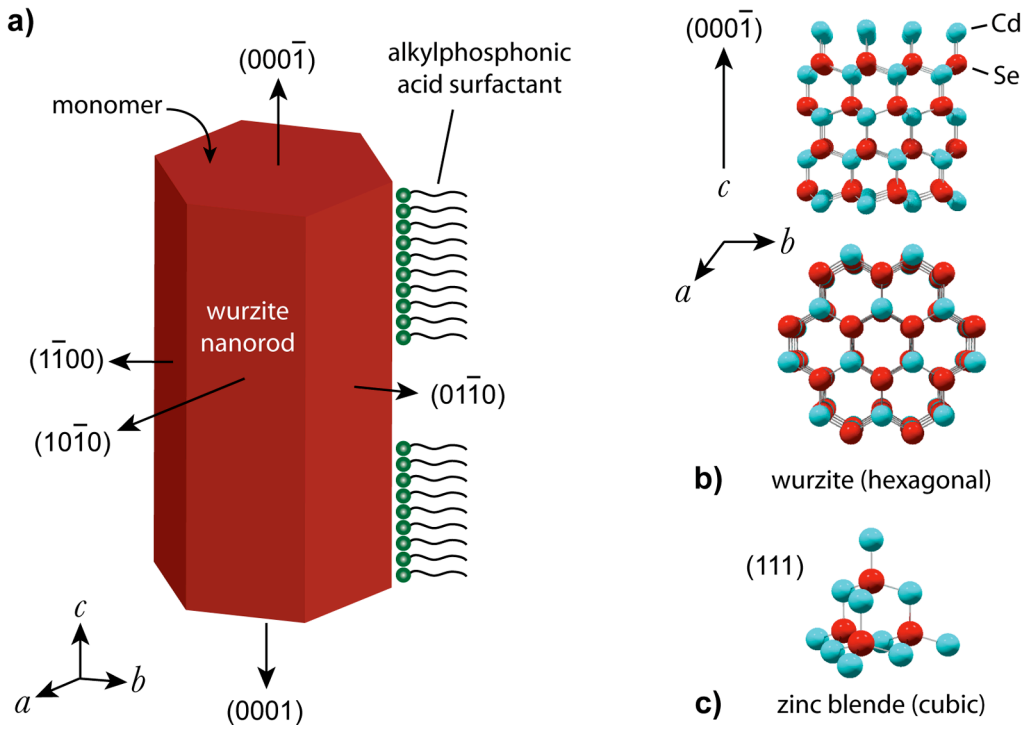

Figure 5.1. (a) Wurzite CdSe nanorod model illustrating the various crystal faces. Alkylphosphonic acids bind preferentially to the lateral surfaces, leaving the higher-energy ±(0001) faces to react with monomer in solution and promoting anisotropic growth along the c axis. (b) Wurzite crystal structure, shown in side and bottom projections (top & bottom frames). (c) Zinc blende crystal structure, highlighting the tetrahedral {111} faces, which are equivalent to the wurzite (000$\bar{1}$) faces.

The most basic extension of CdSe nanocrystal growth beyond spheres is the synthesis of CdSe nanorods.[1] Given the anisotropy of the wurtzite crystal structure, it is not surprising that elongated particles can form – most likely due to differing surface energies between the $(000\bar{1})$ end face and the non-polar $\{1\bar{1}00\}$ and $\{10\bar{1}0\}$ side faces (Figure 5.1). Peng *et al.* noted that the preferential binding of phosphonic acid surfactants onto the non-polar side faces resulted in faster growth along the *c*-axis of the crystal, thus leading to rod-shaped particles.[1] In addition to their selective adhesion on CdSe facets, phosphonic acids form very stable complexes with cadmium atoms, reducing nucleation and encouraging the high monomer concentrations required to drive the rapid, kinetically driven anisotropic growth.[15] At depleted monomer concentrations, Ostwald ripening[16] results in the transport of ions to the sides of the nanorods from the high energy (0001) and $(000\bar{1})$ faces,[15] ultimately equilibrating the particles into large, polydisperse spheres. Nucleation is therefore a key parameter for anisotropic growth, since the number of nuclei influences the monomer concentration remaining after nucleation as well as the rate of consumption for the total population of growing particles. Thus, an effective strategy for the synthesis of highly anisotropic structures is to (1) minimize nucleation by tuning the reactivity of surfactants and precursors, (2) temporally separate the muted nucleation stage from the rapid growth stage, and (3) maintain rapid, selective growth by preventing monomer concentrations from decreasing below the thresholds for inter- and intraparticle ripening.

Tetrapods

Another method of controlling shape is to modulate the crystal structure within a nanoparticle. While CdSe dots and rods synthesized at high temperature typically have the hexagonal wurtzite structure (Figure 5.1b), an accumulation of stacking faults can lead to domains of the cubic zinc blende phase (Figure 5.1c). Because zinc blende has four {111} faces that are equivalent to the $(000\overline{1})$ face of the wurtzite lattice, zinc blende domains can induce tetrahedral branching in nanorods. Such phenomena are hypothesized to be the reason for the formation of CdSe and CdTe tetrapods from zinc blende cores.[3,4] The effectiveness of any deliberate strategy to induce branching would be dependent on the thermodynamic stability of wurtzite and zinc blende at various temperatures, with various surfactants, and at various monomer concentrations. Recent studies by the Alivisatos group also suggest that the preferential growth of zinc blende in tetrapod cores may be encouraged by high initial monomer concentrations.[17]

Hollow shells

The shapes and composition of particles can be changed using post-synthetic steps. For example, cobalt spheres can be rendered hollow by sulfidation or oxidation via the nanoscale-Kirkendall effect.[18] Due to the large disparity between the diffusion constants of Co and S ions in cobalt sulfide, voids are formed in the original Co nanoparticle as the more mobile Co cations diffuse towards the outer surface of the crystal. This reaction is extremely rapid (~5 s) at 160 °C, but takes hours at room temperature. The final product, Co_3S_4 or Co_9S_8, is determined by the stoichiometry of the reagents.

The anisotropic synthesis of the rods, tetrapods, and hollow shells are all extremely sensitive to the reaction conditions. Continuous flow microreactors, as previously described, are hypothesized to be beneficial both in terms of localized control and reproducibility and in terms of rapidly scanning for the optimal growth conditions.

5.2 EXPERIMENTAL

5.2.1 Improvements over previous chips and protocols

The goal of anisotropic nanoparticle growth prompted major modifications to my microreactor and protocols in order to address shortcomings in my first-generation device. The previous device used low temperatures and concentrations, had bulky temperature control, pre-mixed precursors that could nucleate prematurely, was limited to diffusive mixing, and incorporated unorthodox surfactants. These limitations discourage anisotropic nanocrystal growth, because shape control requires high monomer concentrations, temperatures, and precise control over nucleation. In the following sections, I will describe the improvements in the microreactors and procedures used to grow anisotropic nanoparticles.

Improved reagents

The TOPO/dodecylamine/octadecene surfactant mixture used for growing spherical nanocrystals cannot be used to synthesize anisotropic nanoparticles. The synthesis of high quality nanorods traditionally uses long-chain alkylphosphonic acids (xPAs), which have high

melting points and low solubilities in hydrocarbon solvents such as ODE. To synthesize CdSe nanorods in microfluidic reactors, shorter-chain octyl- and decylphosphonic acid surfactants are dissolved in tri-*n*-octylphosphine (TOP), a viscous liquid at room temperature. Because these phosphonic acids are not completely soluble in TOP at room temperature, the Cd/xPA/TOP precursor plug is heated to 80 °C in the sample loop of the HPLC injection valve using heating tape and glass wool insulation. The short (~10 cm) distance between the loop and the heated chip is also insulated in order to prevent significant cooling of the Cd precursor. This heating system allows us to use a surfactant system that can synthesize anisotropic particles over a wider temperature range and that is more similar to those found in flask preparations.

The precursors chosen for the synthesis of spheres, dimethylcadmium and Se-TBP, while historically used for pyrolytic nanocrystal growth, are volatile, pyrophoric, toxic, and corrosive to the syringes and O-rings used in the microfluidic apparatus. Concurrently with the development of the first generation microfluidic reactor, Xiaogang Peng's group demonstrated that Cd precursors can be prepared by complexing CdO powder with various ligands, such as phosphonic acids, carboxylic acids, and amines.[19] Such Cd-phosphonate, -carboxylate, and -amine complexes are much less reactive than dimethylcadmium, resulting in more reproducible syntheses. These Cd-xPA complexes naturally form when CdO decomposes at >160 °C in the presence of phosphonic acids and are used in conjunction with the xPA/TOP surfactant system to synthesize CdSe nanorods. Peng's group also pioneered the synthesis of nanocrystals, including CdTe tetrapods, in octadecene solvent instead of using the TOPO surfactant as the solvent. Using this approach, CdTe tetrapods are synthesized from $Cd(oleate)_2$ complexes in octadecene.[20]

For the anion precursors, Se-TOP and Te-TOP are used rather than the analogous TBP complexes. These TOP complexes are not pyrophoric and are more chemically and thermally stable than TBP.

Mixing control

In addition to growth-mediating surfactants and precursors, the rapid nature of anisotropic growth requires a very precisely controlled nucleation event that does not create too many nuclei. The microfluidic synthesis of spherical nanocrystals combined the Cd and Se precursors into a single reagent solution, meaning that the Cd and Se precursors could gradually form nuclei before entering the chip. To counter this, the second-generation chip separates the precursor streams such that the Se precursor is injected in between two outer sheaths of the Cd precursor. Because purely diffusive mixing across the laminar streams of viscous TOP solution would require ~16 s, I attempt to accelerate mixing by incorporating three dimensional "staggered herringbone mixers" after the precursor intersection.[21] The function of such ridged structures is to induce lateral convection in the fluid flow that folds the reagent streams, increases the interfacial area, and reduces diffusion lengths.

The initial separation and rapid mixing of precursors are especially important when performing rapid reactions, such as the sulfidation of Co nanoparticles to create hollow cobalt sulfide nanoshells.

Temperature control

The primary method for inducing nucleation in my microreactors is to rapidly increase the temperature of the precursor solution. The previously used aluminum block heaters had large thermal masses that produced broad thermal gradients at the boundaries of the block. To counter this, I microfabricated aluminum thin film heaters directly on the glass chips. These microheaters allow for more precise and rapid temperature control over small zones and residence times. For example, with separate power supplies and temperature sensors, short lengths of the reaction channel can be heated at different temperatures to create more complex thermal profiles than allowed by previous devices or in flask syntheses. One conceivable profile would be to have a small heater to promote a short burst of nucleation and a longer heater optimized for a lower-temperature but longer growth period. Microfabricated heaters can also be designed to generate sharp thermal gradients that can ramp temperatures up or down on the order of milliseconds, rather than the minutes required for bulk fluids.

Microfabricated heaters also allow for higher growth temperatures, because the heaters' direct thermal contact, small footprints, and lower power consumption result in much less excess heat being transferred to heat-sensitive parts of the apparatus, such as the silicone O-rings.

While the insulating properties of glass wafers allow large gradients to be created, glass is poor at distributing heat uniformly over large surface areas. Factors such as convection and variability in heater resistances can lead to significant variations in temperatures across the wafer. Therefore, the larger heaters are split into several independently controlled zones, and ceramic fiber insulating tape is used to thermally isolate

the chip from its surroundings. Finite element simulations with FEMlab were also performed to optimize the heater geometries.

5.2.2 Microreactor chips

Nanocrystal microreactors are fabricated from borofloat glass wafers using the procedures outlined in Chapter 3. Several different channel geometries are used for the synthesis of anisotropic nanocrystals.

Sheath injection chip (*THD5c*)

The 6.9 μL sheath injection chip shown in Figure 5.2 is designed to mimic the traditional injection pyrolysis scheme used in bulk fluids. Se precursor is injected into the microreactor between two Cd precursor sheaths, after which the solution is heated by a small nucleation heater fabricated underneath the channel with 1 μm-thick Al/2% Si. Before and during the nucleation heating, the channel is mixed by several cycles of staggered herringbone mixers that protrude down from the roof of the channels. These 5 μm-high ridges are etched concurrently with the channel, utilizing the undercutting properties of isotropic HF etching. After a short nucleation residence time, the solution enters a long, serpentine growth region, which is heated from below using two growth heaters, which are independently controlled to maintain a more uniform (±10 °C) temperature profile. After the nanocrystal product exits the heated region, it is diluted by another solvent, such as octadecene or toluene, in order to kinetically quench the reaction. This dilution loop is

substantially colder (T = 50 °C) than the heated region due to the steep gradients generated by microfabricated heaters and due to the large thermal mass of the aluminum/PEEK manifolds clamped over this loop.

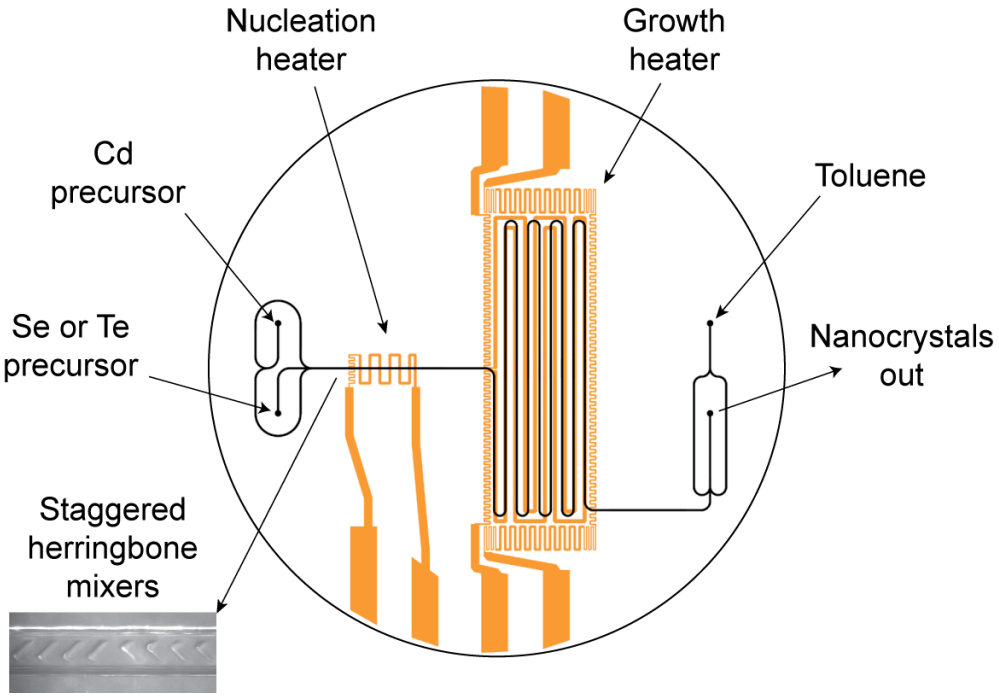

Figure 5.2. Sheath injection chip design. The 100 mm-diameter borofloat chip is fabricated with 307 μm-wide, 58 μm-deep microchannels (black lines). Two thermal zones are controlled by three separate Al/2% Si microfabricated heaters (orange), which are patterned to promote a more homogeneous thermal profile in each zone. The inset photograph shows the 5 μm-high staggered herringbone mixers designed to mix the Cd and Se streams before and during nucleation heating.

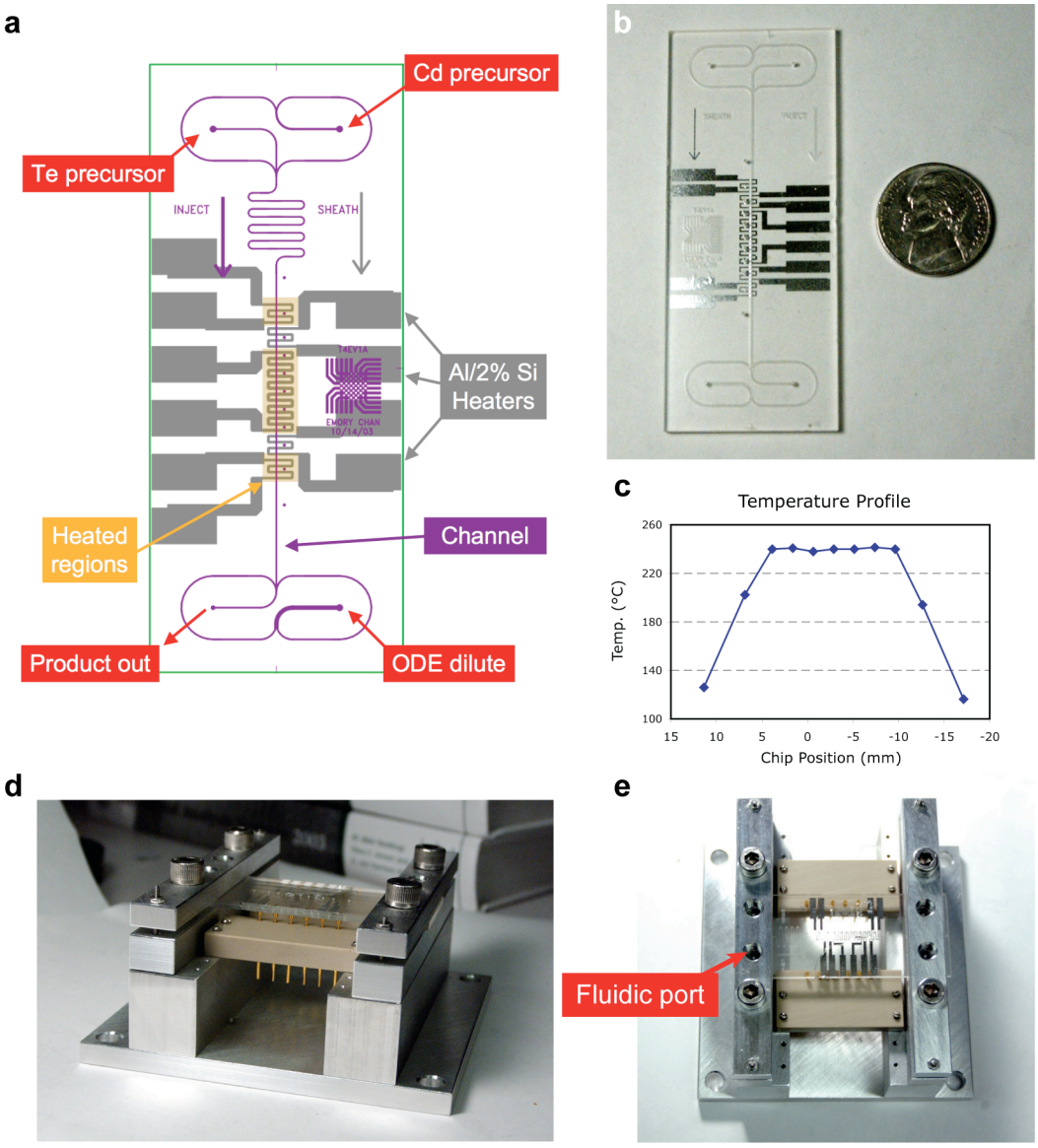

Figure 5.3. T4EV1 tetrapod rapid evolution chip. (a) T4EV1a schematic, showing the 63 μm-deep, 304 μm-wide reaction channel with a serpentine mixing region and 5 independent heaters made from 1 μm-thick, 300 μm-wide aluminium/2% silicon lines. (b) Photograph of a straight channel T4EV1b chip. (c) Thermal profile along the channel using three independent PID control zones. (d) & (e) Photographs of the T4EV1 chip loaded in its screw-in compression chuck, which includes ¼"-28 tapped holes for fluidic fittings and spring-loaded "pogo" pins for electrical connections.

Tetrapod rapid evolution chip (*T4EV1*)

A smaller chip was designed to measure the kinetics of CdTe tetrapod growth over short (<10 s) time periods. The mask pattern of this tetrapod evolution chip (T4EV1) is shown in Figure 5.3. Except for a drastically reduced channel length, T4EV1 is fluidically equivalent to sheath injection chip, with injection and dilution loops. Five aluminum heaters are fabricated across a 22-mm length of heated channel and are designed to generate sharp thermal gradients at the heater edges and flat thermal profiles within the 384-nL reactor region (Figure 5.3c). At a total flow rate of 3 μL/min (2:1 sheath:inject), the total residence time in the heated region is 7.7 s. Channels are silanized according to the procedure in Section 3.4 to reduce deposition on channel walls

5.2.3 Synthesis conditions

CdSe nanorods

Nanorods are synthesized in a sheath injection microreactor (Figure 5.2) by injecting a solution of selenium/tri-n-octylphosphine (Se/TOP) into a solution of cadmium alkylphosphonate (Cd-xPA), dodecylamine (DDA), and TOP. Due to the stability of Cd-xPA and Se-TOP, smaller rods can also be synthesized by injecting a combined Cd/Se precursor into a single injection chip.

For either reaction scheme, the 15% wt/wt Se/TOP solution is prepared by dissolving Se powder (Aldrich) in TOP (90%, Strem) under argon overnight. In a typical reaction, the Cd-alkylphosphonate solution is prepared by adding to a 25 mL flask 0.14 g CdO, 0.1 g DDA, 3.2 g TOP, and 0.5 g phosphonic acid (2.2:1 xPA:Cd mole ratio, where

xPA = octyl- or decylphosphonic acid, PolyCarbon Industries). Upon heating the flask to >250 °C under argon, the brown CdO powder decomposes and complexes with the alkylphosphonic acid to form $Cd(xPA)_2$ and water. To remove the water and oxygen, the solution is degassed under vacuum and purged with argon three times over a total of ~1 h at 120 °C. Solutions are often aged under argon at room temperature in the dark for ~12 h and degassed again before use.

Rods are cleaned by precipitating the nanoparticles with ethyl acetate, with the drop-wise addition methanol if needed. The solution is centrifuged, and the pellet is resuspended. This cycle is repeated four times, with the resuspension solvent alternating between tetrahydrofuran and toluene.

CdTe nanocrystals

Spheres

For the synthesis of spheres from Cd-oleate complexes, the Cd precursor is prepared from with 28 mg of CdO, 0.27 g of oleic acid (4.4:1 surfactant:Cd mole ratio), and 1.7 g of octadecene. Upon heating the flask to >250 °C under argon, the CdO decomposes and forms a clear yellow $Cd(oleate)_2$ complex. The solution is cooled to 120 °C and degassed for 1 h.

A "10%" wt/wt Te-TOP/TOP solution is prepared by stirring Te shot (99.999%) in TOP under argon at 250 °C for 40 minutes, after which the solution turns orange and mostly clear. After cooling, the yellow solution is transferred to an argon-filled vial and centrifuged at 3100 RPM for 2.5 hours. The clear yellow supernatant is decanted from the gray pellet and stored under argon. Due to this purification step, the actual Te concentration is <10% and is estimated to be ~9%.

A Te-TOP/ODE stock solution is prepared from 80 mg of 9% wt/wt Te/TOP and 2.8 mg of octadecene. 2.5 ml of this Te stock solution is added to the Cd-oleate solution, resulting in a 5:1 Cd:Te mole ratio.

A syringe filled with this Cd/Te solution is used to directly inject the combined precursor into a single injection chip (5 μl) mounted on an aluminum block heater or with a Kapton thin film heater. CdSe spheres are also synthesized with this method by substituting Se/TOP for Te/TOP.

Tetrapods

In a typical reaction, a 20 mM Cd-oleate, 4:1 oleic acid:Cd solution is prepared as described above for the CdTe sphere synthesis. The 20 mM Te-TOP solution injected into the chip typically consists of 0.077 g of 9% wt/wt Te/TOP, 0.68 g ODE, and 0.073 g oleic acid. The concentration of oleic acid is kept constant (~90 mM) to prevent gradients in surfactant concentration.

The Te/TOP/ODE solution is injected in the center inlet of the sheath injection chip at a typical flow rate of 2 μl/min, while the Cd-oleate is pumped at twice the Te flow rate into the inlet that supplies both sheaths. Using equimolar Cd/Te concentrations, a 2:1 Cd:Te flow rate ratio results in a 2:1 mole ratio. The chip is heated from below using the aluminum microfabricated heaters with a center temperature of 260 °C and no nucleation heating.

Tetrapods are cleaned by precipitating the tetrapods with acetone, centrifuging for ~5 min, and resuspending the nanocrystal pellet in a minimal amount of toluene. This cleaning cycle is repeated three times.

Hollow spheres

Co nanoparticles were synthesized by Andreu Cabot according to a preparation by Yin *et al.*[18,22] To synthesize cobalt sulfide hollow shells from Co nanoparticles, a solution of Co nanoparticles in oleic acid and dichlorobenzene (DCB) is injected into the center stream of the chip, while a solution of sulfur in DCB (S/DCB) is injected into the 2 outer sheaths. Typical flow rates are 2 μL/min for the Co/DCB solution in the center inlet and 2 μL total for the two S/DCB sheath solutions, for a total of 4 μl/min.

5.3 RESULTS & DISCUSSION

5.3.1 CdSe nanorods

CdSe nanorods were synthesized using the phosphonic acid/dodecylamine/ trioctylphosphine (xPA/DDA/TOP) surfactant system in both single-precursor and sheath injection chips. Figure 5.4 shows transmission electron microscopy (TEM) images of nanorods synthesized at four different temperatures and using two different surfactants. For the rods in Figure 5.4a & b, 0.214 M Cd-octylphosphonate precursor was injected into the 0.107 M Se-TOP precursor sheaths at a 1:3 Cd:Se flow rate ratio, resulting in a 2:3 Cd:Se mole ratio. 15 x 6 nm (length x diameter) nanorods (Figure 5.4a) were synthesized at 260 °C for 1 min, while 33 x 7 nm rods were synthesized at 270 °C.

Figure 5.4c & d show nanorods synthesized using decylphosphonic acid surfactant with a single precursor that was 0.21 mM in both Cd-decylphosphonate and Se-TOP. Figure

5.4c shows 28 x 7 nm nanorods synthesized with DPA at 280 °C for 1 min. Figure 5.4d shows longer (35 x 7 nm) nanorods grown at 290 °C. The combination of the higher growth temperature and longer chain surfactant resulted in longer, straighter, and more monodisperse rods. Phosphonic acids with even longer chains, such as tetradecyl- or octadecylphosphonic acid, have been shown by others to further reduce stacking faults in flask syntheses, but the high molecular weights of such surfactants make them insoluble in TOP at ≤80 °C. Decylphosphonic acid was thus found to be the best compromise between crystal quality and surfactant solubility.

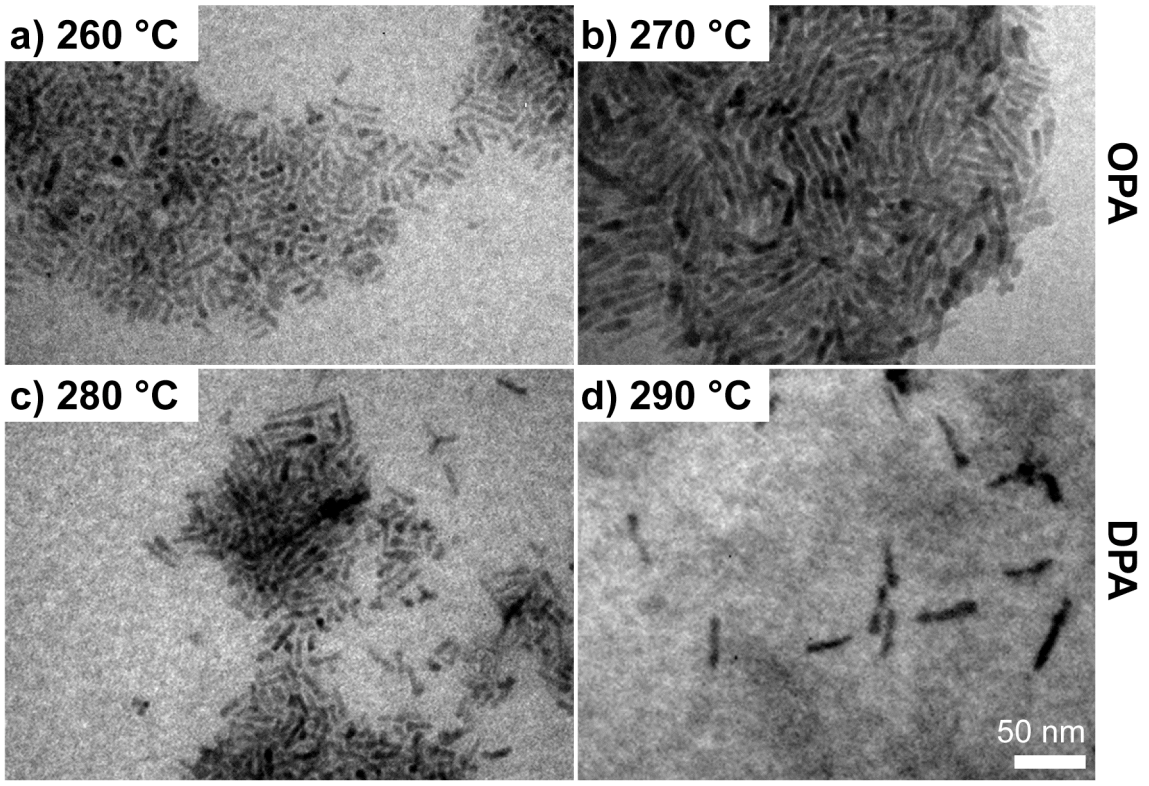

Figure 5.4. Transmission electron micrographs of nanorods grown at four different temperatures for 1 min. The nanorods grown at 260 °C (a) and 270 °C (b), were grown in octylphosphonic acid/TOP, while the rods grown at 280 °C (c) and 290 °C (d) were grown in decylphosphonic acid/TOP.

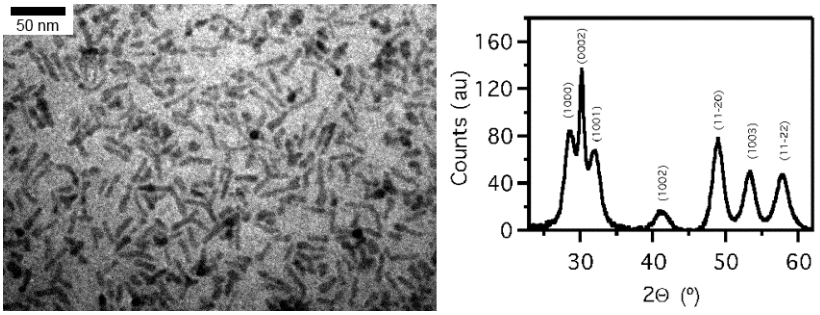

Figure 5.5. TEM image and powder X-ray diffraction pattern of 26 nm x 6 nm nanorods using Co Kα radiation. XRD peak assignments correspond to wurzite crystallographic indices.

The structure and crystallinity of the chip-synthesized nanorods were also characterized by powder X-ray diffraction. A TEM micrograph and X-ray diffraction (XRD) pattern of 26 x 6 nm nanorods grown at 290 °C with OPA are shown in Figure 5.5. The diffraction pattern displays the characteristic peaks of the hexagonal wurzite crystal structure. The sharp, intense (0002) peak at $2\Theta = 30°$ confirms that the long axis of the nanorods is parallel to the wurzite *c*-axis, since the peak width decreases with the number of diffracting crystal planes. Although the aggregate XRD data verifies the high crystallinity of the nanorods grown at high temperature, the extensive branching and broad size distribution displayed in the TEM images demonstrate that microreactor-synthesized CdSe nanorods are generally poor in quality compared to their flask-synthesized counterparts.

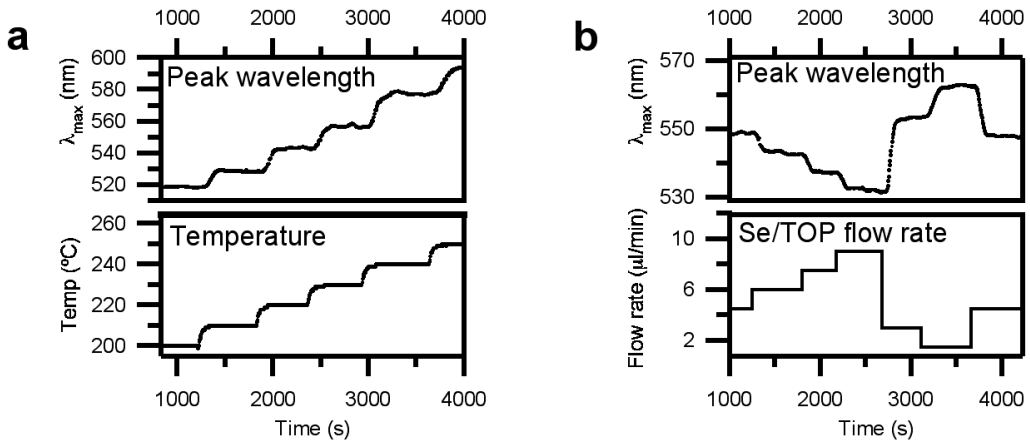

Figure 5.6. Size control of nanorod synthesis via temperature and flow rate/concentration in a 6-μL sheath injection reactor. (a) Peak emission wavelengths of nanorods at various temperatures with a total flow rate of 4 μL/min and 2:3 Cd:Se mole ratio. (b) Peak emission wavelengths of nanorods grown at 230 °C with constant Cd-OPA flow rate of 1.5 μL/min and variable Se/TOP flow rate (initial and final flows mix in 1:1 Cd:Se mole ratios).

The TEM data at various temperatures (Figure 5.4) demonstrate that the growth at 1 min occurs primarily along the axial direction of the nanorods due to the presence of the phosphonic acids on their non-polar side faces. Consequently, using fluorescence spectroscopy, I can monitor the growth of the nanorods with their fluorescence peak wavelength, which generally increases with nanorod length.[23] Figure 5.6a shows how the λ_{max} increases in distinct steps corresponding to 10 °C increases in the growth temperature from 200-260 °C. I can also control the size of nanorods by varying the Se/TOP flow rate. As shown in Figure 5.6b, the λ_{max} increases as the Se/TOP flow rate decreases, while the Cd/TOP flow rate is kept constant. The fact that that the initial and final conditions, both at 4.5 μl/min flow rate, exhibit in the same λ_{max} demonstrates some level of reproducibility at the 230 °C growth temperature.

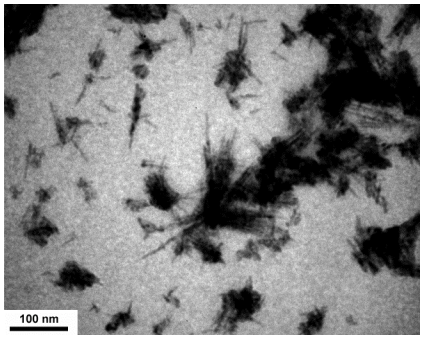

Figure 5.7. Aggregated and overgrown particles collected during nanorod growth in a 280 °C microreactor.

Unfortunately, the same reproducibility cannot be observed for the higher growth temperatures (280 °C) and higher concentrations required for rods of greater length, aspect ratio, crystallinity, and monodispersity. Such improvements are necessary given the poor shape and size distribution exhibited in the TEM images (Figure 5.4) for all conditions tested. Paradoxically, high temperatures and concentrations often result in deposition of nanorods on channel walls, particularly at the regions of steep thermal gradients where most nucleation takes place. Nanorods in particular were observed to be very susceptible to aggregation in the microchannels, because their shape lends them to being aligned by shear such that favorable van der Waals interactions can occur. Shear also increases the collision frequency of the nanorods, which have large collisional cross-sections[24] due to their rotation in shearing flows.[25] During high temperature growth, visible brown deposits were observed on the channel walls. Some deposits occasionally broke off, resulting in highly irreproducible flow as reflected in the fluctuating peak position and intensity of the optical spectra. As shown in Figure 5.7, collected product solution contained large quantities of insoluble aggregates and overgrown deposits that were difficult to clean and solubilize.

Besides high concentration and temperature, the limited solubility of the CdSe nanorods in the TOP solvent could have promoted aggregation and clogging. The addition of amines, such as dodecylamine, was shown to reduce the rate of aggregation and delay the onset of clogging. Oleylamine, used by Yen *et al.* for solubilizing spheres, was shown to solubilize nanorods better than dodecylamine while having the advantage of being liquid at both room temperature and growth temperatures. Unfortunately, oleylamine encourages rampant, uncontrolled branching and is also difficult to clean from the nanocrystals.

5.3.2 CdSe spheres in oleic acid

Despite the limited success in synthesizing CdSe rods in phosphonic acid/TOP surfactant, the poor solubility, high melting point, and high viscosity of the surfactant mixture made synthesis extremely inconvenient and unreliable. In contrast, oleic acid and octadecene are miscible and liquid from room temperature to 300 °C, and octadecene is much less viscous and more stable in air compared to TOP. Using an oleic acid/octadecene (OLA/ODE) surfactant solution, I synthesized CdSe spheres and CdTe nanoparticles with both spherical and tetrapod morphology.

CdSe spheres were synthesized in a 0.25 M OLA/ODE solution using a 6.9 μL sheath injection reactor (Figure 5.2). Absorption spectra for syntheses at 290 °C at four different Cd:Se ratios, shown in Figure 5.8, show sharp exciton peaks typical of monodisperse CdSe quantum dots. The increase in wavelength and decrease in signal as the Cd:Se ratio decreases indicate that lower Cd:Se ratios suppress nucleation. The OLA/ODE synthesis also reduced the amount of nanoparticle deposition on the channel walls.

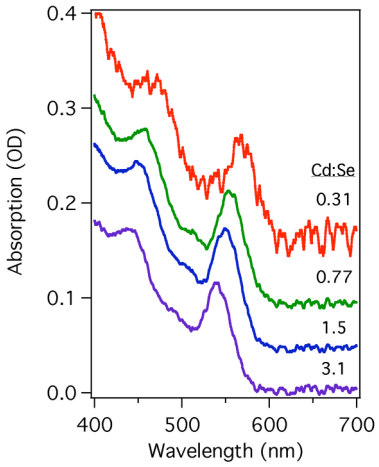

Figure 5.8. Online absorption spectra of CdSe nanospheres synthesized with $Cd(oleate)_2$ and Se-TOP at four different Cd:Se mole ratios. Nanocrystals were grown in 0.25 M oleic acid in octadecene for 3 min at 290 °C in a sheath injection reactor. At 0.31 Cd:Se, the final [Cd] = 46 mM.

5.3.3 CdTe nanocrystals in oleic acid

CdTe spheres

CdTe spheres were synthesized in a 5 μL single-injection microreactor (Figure 4.1a) with 44 mM Cd-oleate, 2.2:1 oleic acid, and 5:1 Cd:Te in octadecene at 280 °C for 25 s. As shown in the TEM images in Figure 5.9, the resulting CdTe nanocrystals are approximately spherical in shape with diameters of 5.6 ± 1.1 nm. Their fluorescence spectrum exhibits a narrow exciton peak at 611 nm with a fwhm of 37 nm. The dots do appear to exhibit some faceting, which is likely a result of the tendency of CdTe to form tetrapod-shaped particles due to the bistability of the zinc blende and wurtzite phases on the nanoscale.

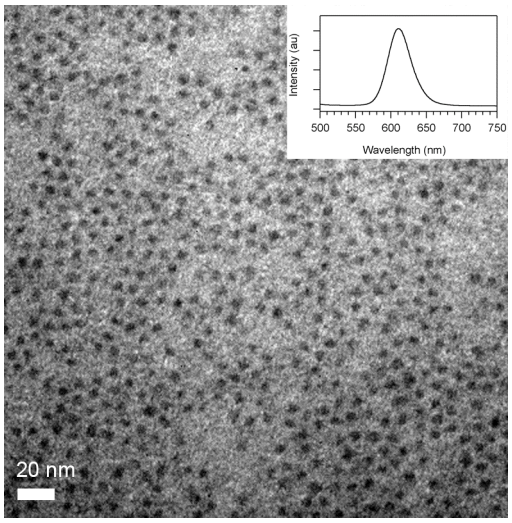

Figure 5.9. TEM micrograph and online fluorescence spectrum (inset) of 5.6 nm-diameter CdTe dots synthesized in a single injection reactor at 280 °C.

CdTe tetrapods

I used the tendency of CdTe to form zinc blende domains to synthesize CdTe tetrapods in a 6.9 μL sheath injection microreactor (Figure 5.2) using 59 mM Cd-oleate, 4:1 oleic acid, and a 1:1 Cd:Te mole ratio. Heating these precursors to 260 °C resulted in a high percentage of branched nanostructures, as shown in Figure 5.10. Most particles were observed to have three or four arms of varying length but with consistent arm diameter. The 12% relative standard deviation for the arm diameters at both residence times was reasonably monodisperse and was corroborated by the narrow fluorescence spectra (fwhm = 34 nm @ 645 nm) in Figure 5.11.

Although these tetrapods are small enough to be fluorescent, they are large enough to exhibit wurzite arm growth. A reaction time of 68 s resulted in arms lengths of 18±3 nm and arm diameters of 4±0.5 nm. Doubling the reaction time to 137 s only served to shorten and fatten the tetrapods to 15±3 x 4.5±0.5 nm (arm length x diameter). Although the average dimensions for the two residence times are within one standard deviation of each other, the TEM images in support the observation that doubling the reaction time actually *decreases* the tetrapod arm length and increases the diameter. This shortening and fattening of the arms indicates that the tetrapods are experiencing intraparticle ripening. High magnification TEM images at 137 s (Figure 5.10b) clearly show that the ends of the arms appear to be fatter and rounder than the portions of the arms near the center, clear evidence of ripening. Even longer reaction times would lead to the arms separating from the core and equilibrating into spheres. Evidence of such behavior is seen in the broken arms, tripods, and rounded dots in the TEM images at both residence times.

This fast ripening is likely a result of the labile nature of the oleic acid surfactants. Yu *et al.* have noted that the Cd-oleate precursors have much higher yields than their Cd-phosphonate analogues, which implies that both nucleation and growth are much faster.[20] The high oleic acid:Cd ratios (4.4:1) used have also been shown by Bullen *et al.* to encourage ripening.[26]

Due to the rapid onset of ripening, microreactors have difficulty in synthesizing CdTe tetrapods in OLA/ODE beyond a very narrow range of arm lengths. Changing precursor concentrations does not appear to reduce the ripening substantially, and high oleic acid:Cd ratios (>3:1) must be used to sufficiently coordinate and solubilize the Cd monomer.

The limitations of the oleic acid/octadecene surfactant/solvent system are unfortunate, since it is orders of magnitude more compatible with chip synthesis than the

phosphonic acid/TOP or TOPO/DDA/octadecene systems previously discussed. Particles are reasonably soluble in oleic acid/octadecene, and much lower concentrations of CdO can be used since the yield when using Cd-oleate precursors is much higher than that for Cd-phosphonate.[20] Lower concentrations and higher solubilities lead to less deposition on channel walls, although after ~2 hrs of synthesis, aggregates still accumulate near sharp thermal gradients, albeit with substantially less chance of clogging.

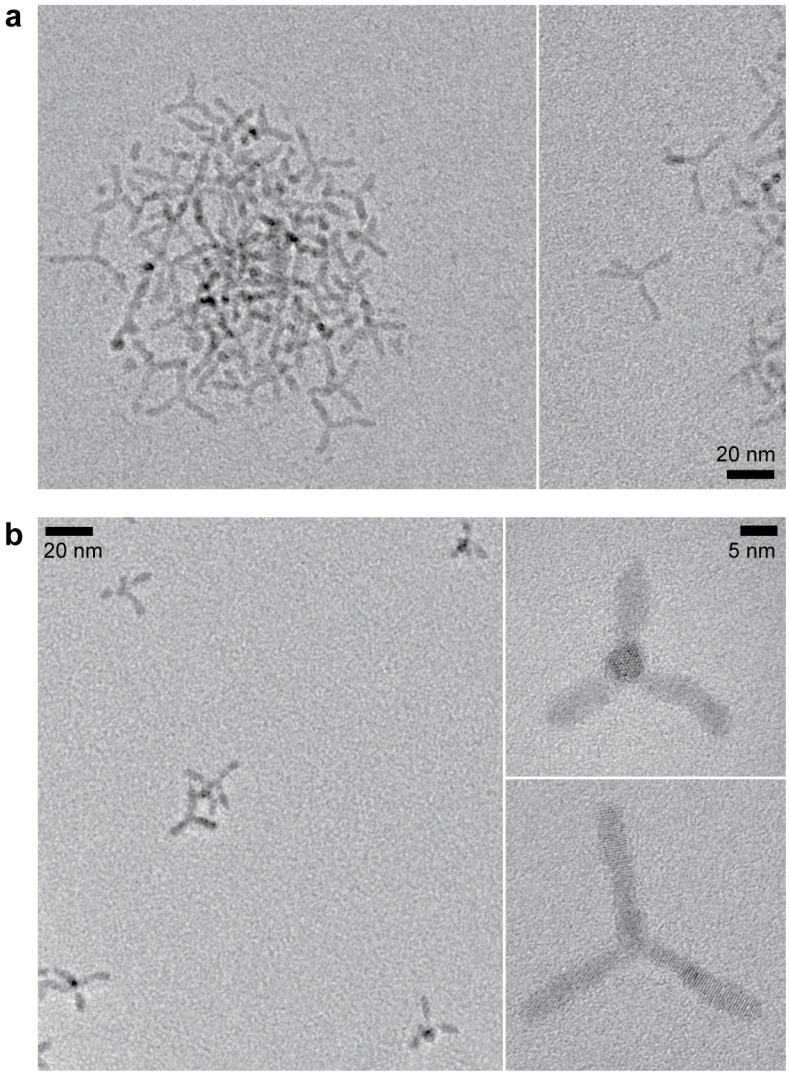

Figure 5.10. TEM images of CdTe tetrapods synthesized at 260 °C for (a) 69 s and (b) 137 s. The final Cd-oleate concentration was 13 mM in octadecene with 1.8:1 Cd:Te and 4.5:1 oleic acid:Cd mole ratios.

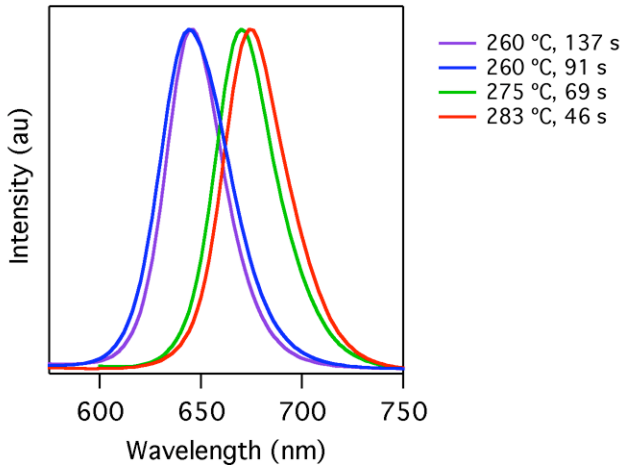

Figure 5.11. Off-line fluorescence spectra for CdTe tetrapods collected from the sheath injection reactor at four different conditions.

Short time evolution of CdTe tetrapod morphology

Without the ability to synthesize large tetrapods, I investigated the short-time evolution of tetrapods from their hypothesized origin as small, zinc blende nuclei. One of the advantages of microfluidics is that short reaction times can be specified due to the rapid heating and cooling necessary to start and stop reactions over short periods of time. I used short, 22 mm-long, 380 nL reactors that were heated by microfabricated heaters optimized to generate uniform thermal zones surrounded by steep thermal gradients. The average residence time of the particles in these short channels ranged from 2.6-15 s, although the precision of these values will be discussed later.

Figure 5.12a shows TEM micrographs of the tetrapods grown at 260 °C at four different residence times. As would be expected, the tetrapod arms grow longer at extended residence times, but their widths do not change significantly. Furthermore, branched particles are visible at even 2.6 s, meaning that the zinc blende "nuclei" from which the arms

extend must have been formed at a time well before 2.6 s. Some of these dot-shaped nuclei are visible in the 2.6 s micrograph, but particles from shorter residence times were not resolved by TEM.

Online absorption spectroscopy, however, did resolve nanocrystal exciton peaks for residence times as short as 0.4 s. Figure 5.12b displays the absorption spectra of these CdTe nanocrystals from 0.4 s to 137 s. The absorption spectra at early times (<6 s) are very noisy and broad due to the low volume fraction of CdTe in solution, but the spectra become much better defined as the particles are allowed to grow for longer times (>7 s). The exciton absorption peak, which is strongly correlated with the arm diameter in CdTe tetrapods,[4] shifts in the first 8 s of growth, but then requires another 130 s of growth to red-shift an equivalent amount. This suggests that the growth of the particles over this intermediate period (8-137 s) is predominantly in the anisotropic lengthening of the tetrapod arms, or "1-dimensional growth," rather than the simultaneous fattening and lengthening of the arms in "2-D" growth.

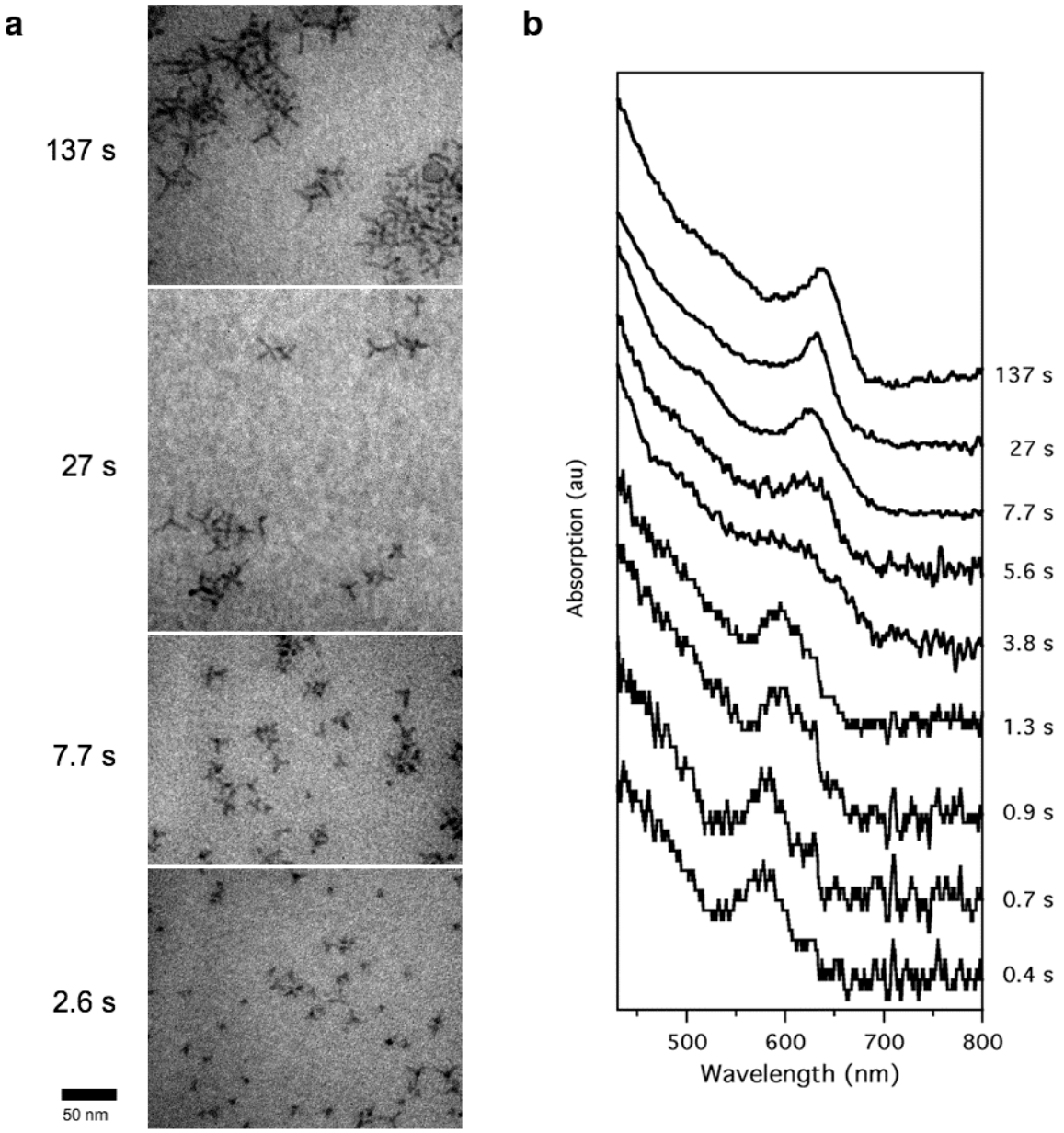

Figure 5.12. Time evolution of CdTe tetrapod growth at 260 °C. (a) TEM images at the labeled average residence times. The 27 s and 137 s times were synthesized using a 6.9 μL microreactor, while the 2.6 and 7.7 s times were synthesized in a 380 nL reactor. (b) Online absorption spectra at the times shown.

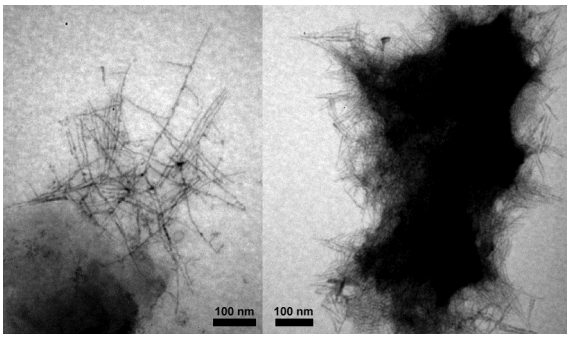

Figure 5.13. TEM micrographs of overgrown CdTe aggregates formed during "rapid" tetrapod synthesis at 260 °C.

Unfortunately, there are major problems with these rapid growth experiments that make any conclusions highly tenuous. TEM and absorption data show fairly large distributions in size and shape for these rapidly grown tetrapods – arm lengths vary significantly by TEM grid location, and there are many particles with 2, 3, 5, and even 6 arms. In addition, large amounts of aggregation and deposition, to the level of clogging, were observed in these short channels (Figure 5.13). Since particles could have been delayed in the reactor by temporary deposition or clogging, residence time estimates are highly unreliable and no conclusive kinetic analysis can be performed.

The observation that tetrapods are aggregating more in these short channels appears to contradict the fact that that significantly less deposition was observed for the longer microreactors. But the deposition is consistent with previous observations that (1) deposition appears to occur predominantly during thermally induced nucleation, and (2) that steeper thermal gradients exacerbate the deposition. While deposition during nucleation is logical given the lower barrier to heterogeneous nucleation, the link between the magnitude of the thermal gradient and aggregation is still unclear. Aggregation, rather than heterogeneous nucleation, appears to be the major issue with CdTe in OLA/ODE, since

easily dislodged aggregates still appeared even when passivating channel walls with the fluoroakylsilane FDTS.

Even if the deposition issue were addressed, these short-time reactions would still be inconclusive due to the broad residence time distributions (RTDs) of laminar flow in short channels.[27] Taylor dispersion theory (Section 2.2.3) can be used to calculate that, at a linear flow velocity of 8.6 mm/s in a 304 x 63 μm channel, and assuming each nucleus has an average hydrodynamic radius of 1.5 nm, the standard deviation of the 2.6 s residence time is 0.8 s, or 33 % relative standard deviation (RSD). This distribution implies that only 68% of the particles have residence times between 1.7 and 3.4 s. This effective resolution of 1.7 s is not desirable for residence times of only 2.6 s, and the resolution becomes worse as residence times decrease further.

In addition, with a 2.6 s residence time, $D_{disp}/uL = 0.045$, indicating a strong deviation from a Gaussian distribution. This means that a significant portion of the starting material is lingering in the channel for much longer than the intended residence time, where it can deposit on channel walls or alter growth conditions for incoming particles.

Given the uncertainty in both the residence time and channel conditions at the initial (<3 s) stages during which tetrapod evolution is most interesting, even the most ideal experiments in such continuous flow reactors are not reliable or precise enough to support meaningful conclusions.

5.3.4 Cobalt Sulfide Hollow Shells

Hollow cobalt sulfide nanoshells were synthesized by mixing a stream of previously synthesized ε-Co nanoparticles with a solution of sulfur/dichlorobenzene at 160 °C in a 50

μm-deep, 250 μm-wide straight channel with 25 μm-deep staggered herringbone mixers. TEM images in Figure 5.14 show the original Co particles and the resulting hollow cobalt sulfide shells formed after an average residence time of only 1.8 s. This short reaction time verifies casual bulk synthesis observations that the sulfidation of Co particles occurs very rapidly.

The RTDs of such short reaction times are very large, however, and as with other anisotropic nanoparticle syntheses in microreactors, this nanoshell reaction resulted in severe reactor fouling that soon led to complete clogging. Thick black deposits formed precisely in the regions that were heated, and deposition only occurred when both Co nanocrystals and sulfur were present. Due to the refluxing of DCB at 160 °C, bubbles occasionally formed, resulting in gas-liquid segmented flow that served to decrease the residence time distribution and clear out accumulating aggregates. This observation hinted at a solution for ameliorating the runaway nature of the deposition and velocity profile issues.

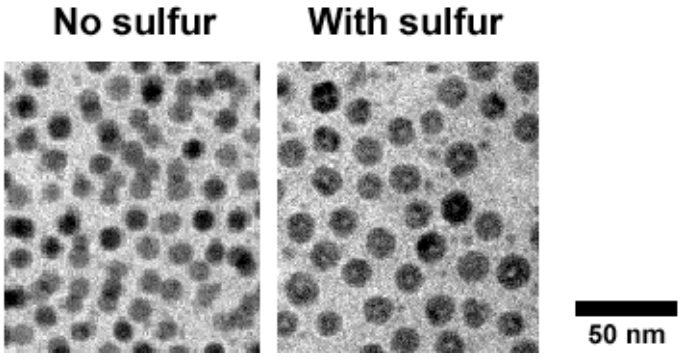

Figure 5.14. Original Co nanoparticles (left) and cobalt sulfide hollow shells (right) formed by reacting Co nanocrystals with sulfur at 160 °C in dichlorobenzene for 1.8 s.

5.4 CONCLUSION

I have demonstrated the high-temperature microfluidic synthesis of anisotropic nanocrystals with three different systems: CdSe nanorods, CdTe tetrapods, and cobalt sulfide hollow shells. In order to control the shape of nanoparticles, I selected surfactants and precursors that allowed kinetic control over the growth on specific crystal faces. A second generation of microreactors was designed to optimize the concentrations and temperatures during nucleation and growth. TEM micrographs and optical spectra illustrate control over particle dimensions by tuning parameters such as temperature and time. For example, the rapid evolution of CdTe tetrapod arm length in oleic acid/octadecene was observed from 2.6 to 137 s.

In general, microreactors were more successful at synthesizing high quality CdTe tetrapods than synthesizing CdSe nanorods or cobalt sulfide hollow shells. The CdSe nanorod synthesis in xPA/TOP was unwieldy, irreproducible, generated broad size distributions, and resulted in clogging. Microfluidic CdTe tetrapod synthesis in OLA/ODE,

however, was much more reliable and generated more monodisperse particles with more uniform shapes.

Serious concerns about the precision and reproducibility of such microfluidic syntheses exist due to extensive particle deposition in the microreactors and due to the large residence time distributions at short reaction times. While these problems were noted during the synthesis of spheres, the high concentrations, high temperatures, and rapid kinetics required for high quality anisotropic growth exacerbate the effects exponentially.

In the next chapter, I describe my attempts to solve the vexing problems of particle deposition and residence time distribution.

5.5 REFERENCES

(1) Peng, X. G.; Manna, L.; Yang, W. D.; Wickham, J.; Scher, E.; Kadavanich, A.; Alivisatos, A. P. *Nature* **2000**, *404*, 59.

(2) Akiyama, S.; Takahashi, S.; Kimura, T.; Ishimori, K.; Morishima, I.; Nishikawa, Y.; Fujisawa, T. *Proc. Natl. Acad. Sci. U. S. A.* **2002**, *99*, 1329.

(3) Manna, L.; Scher, E. C.; Alivisatos, A. P. *J. Am. Chem. Soc.* **2000**, *122*, 12700.

(4) Manna, L.; Milliron, D. J.; Meisel, A.; Scher, E. C.; Alivisatos, A. P. *Nat. Mater.* **2003**, *2*, 382.

(5) Milliron, D. J.; Gur, I.; Alivisatos, A. P. *MRS Bull.* **2005**, *30*, 41.

(6) Huynh, W. U.; Dittmer, J. J.; Alivisatos, A. P. *Science* **2002**, *295*, 2425.

(7) Klein, D. L.; Roth, R.; Lim, A. K. L.; Alivisatos, A. P.; McEuen, P. L. *Nature* **1997**, *389*, 699.

(8) Cui, Y.; Banin, U.; Bjork, M. T.; Alivisatos, A. P. *Nano Lett.* **2005**, *5*, 1519.

(9) Hu, J. T.; Li, L. S.; Yang, W. D.; Manna, L.; Wang, L. W.; Alivisatos, A. P. *Science* **2001**, *292*, 2060.

(10) Li, J. B.; Wang, L. W. *Nano Lett.* **2003**, *3*, 1357.

(11) Manna, L.; Scher, E. C.; Li, L. S.; Alivisatos, A. P. *J. Am. Chem. Soc.* **2002**, *124*, 7136.

(12) Link, S.; Wang, Z. L.; El-Sayed, M. A. *J. Phys. Chem. B* **2000**, *104*, 7867.

(13) Zaziski, D.; Prilliman, S.; Scher, E. C.; Casula, M.; Wickham, J.; Clark, S. M.; Alivisatos, A. P. *Nano Lett.* **2004**, *4*, 943.

(14) Cao, G. *Nanostructures and Nanomaterials: Synthesis, Properties, and Applications*; Imperial College Press: London, 2004.

(15) Peng, Z. A.; Peng, X. G. *J. Am. Chem. Soc.* **2002**, *123*, 3343.

(16) Peng, X. G.; Wickham, J.; Alivisatos, A. P. *J. Am. Chem. Soc.* **1998**, *120*, 5343.

(17) Milliron, D. J.; Hughes, S. M.; Cui, Y.; Manna, L.; Li, J. B.; Wang, L. W.; Alivisatos, A. P. *Nature* **2004**, *430*, 190.

(18) Yin, Y. D.; Rioux, R. M.; Erdonmez, C. K.; Hughes, S.; Somorjai, G. A.; Alivisatos, A. P. *Science* **2004**, *304*, 711.

(19) Qu, L.; Peng, Z. A.; Peng, X. *Nano Lett.* **2001**, *1*, 333.

(20) Yu, W. W.; Wang, Y. A.; Peng, X. G. *Chem. Mater.* **2003**, *15*, 4300.

(21) Stroock, A. D.; Dertinger, S. K. W.; Ajdari, A.; Mezic, I.; Stone, H. A.; Whitesides, G. M. *Science* **2002**, *295*, 647.

(22) Yin, Y. D.; Erdonmez, C. K.; Cabot, A.; Hughes, S.; Alivisatos, A. P. *Adv. Funct. Mater.* **2006**, *16*, 1389.

(23) Li, L. S.; Hu, J. T.; Yang, W. D.; Alivisatos, A. P. *Nano Lett.* **2001**, *1*, 349.

(24) Winkler, R. G.; Mussawisade, K.; Ripoll, M.; Gompper, G. *J. Phys.-Condens. Matter* **2004**, *16*, S3941.

(25) Wierenga, A. M.; Philipse, A. P. *Colloids Surf. A* **1998**, *137*, 355.

(26) Bullen, C. R.; Mulvaney, P. *Nano Lett.* **2004**, *4*, 2303.

(27) Levenspiel, O. *The Chemical Reactor Omnibook*; OSU Book Stores: Corvallis, OR, 1979; Vol. 1.

Chapter 6 Problems with Continuous Flow Microreactors

6.1 INTRODUCTION

The mixed experiences with anisotropic nanocrystal synthesis demonstrate that, although continuous flow microreactors can synthesize a wide variety of shapes and materials, such reactors will not be able to synthesize particles with the quality, range of sizes, and size distribution of particles grown in flask syntheses unless measures are taken to (1) eliminate particle deposition on channel walls and to (2) substantially reduce large residence time distributions. Nanoparticle deposits reduce the lifetime of reactors by encouraging clogging and introduce large uncertainty into the residence time and the rate of monomer consumption in the microreactor. Large residence time distributions, while predictable, are a serious problem because the spread of reaction times reduces the ability to precisely perform rapid reactions as well as the ability to rapidly switch concentrations and other reaction parameters. This chapter will discuss the various attempts to reduce both of these critical issues in the context of anisotropic nanoparticle synthesis.

6.2 ATTEMPTS TO PREVENT PARTICLE DEPOSITION

Particle deposition could be occurring due to two reasons: (1) limited solubility of particles and (2) heterogeneous nucleation on channel walls.

6.2.1 Increasing particle solubility

In order to increase particle solubility, I surveyed a variety of different additives to the surfactant mixtures to better coordinate the particle surfaces. Limited solubility suggests that the surfactants presently in the precursor mixtures are not binding adequately to the nanoparticles, or are not present in large enough concentrations. The concentration and chemical functionality of the surfactants play a significant role in the nucleation and growth of particles, however, and deviations from the finely optimized surfactant conditions are often detrimental.

For example, I determined that the use of amines such as dodecylamine and oleylamine reduced particle deposition and aggregation, although not without detrimental effects to the synthesis and convenience of processing. Oleylamine prohibits one-dimensional growth due to its tendency to induce high levels of branching. Amines have been known to stabilize the zinc-blende phase of II-VI crystals. Dodecylamine induces less branching, but its melting point is slightly above room temperature, making it slightly inconvenient.

Restricting the choice of surfactants and concentrations to a narrow range limits the utility of microreactors as tools for screening conditions during synthetic optimization and physical measurements. As described in the previous chapter, the oleic acid/octadecene system was observed to have less aggregation, but mostly due to the lower concentrations of monomer required. Because octadecene is non-coordinating, the solubility of particles in this system is purely dependent on the oleic acid concentration. Increasing the levels of the primary coordinating agent such as phosphonic acids and oleic acid is impractical due to the strong correlation between nanoparticle dimension and surfactant concentration.

Thus, no general method for completely solubilizing nanoparticles during high-temperature growth was found. Even if specific conditions were discovered, the continued departure of synthetic protocols from typical flask recipes is undesirable, since the two techniques should ideally compliment one another.

6.2.2 Surface passivation

Using the silanization protocol in Section 3.4, I attempted to passivate the channel walls by functionalizing them with a fluoroalkysilane, FDTS, which coats surfaces with a material similar to Teflon. Upon successful silanization, these long, fluorinated chains should cross-link with one another to form a robust, low-energy surface less prone to nucleation or adhesion. While I did notice reduced nanoparticle deposition with the FDTS coatings, particle aggregation was still observed over time, and the onset of visible deposition was highly dependent on the temperature, silanization conditions, heating history of the coating, and the concentrations of surfactant and precursors used.

6.3 ATTEMPTS TO REDUCE RESIDENCE TIME DISTRIBUTION

As discussed in Section 2.2.3, a finite distribution in residence times is a consequence of particle diffusion and laminar flow in enclosed channels. Diffusion can be prevented by imposing physical barriers. For example, valves and pumps similar to those developed by Grover *et al.*[1] could be used to shuttle discrete volumes of fluid through a sequence of isolated reaction zones, but few such mechanical components have been developed to withstand the harsh conditions of pyrolytic nanocrystal synthesis. As the scope of this chapter is limited to continuous flow schemes, which are the most common and convenient,

other physical methods for compartmentalizing microscale reaction volumes will not be discussed here.

The laminar flow profile that produces hydrodynamic dispersion can be altered to reduce the residence time distribution (RTD). In the simplest example, reducing the channel diameter will lower the RTD by enhancing radial diffusion. Because the effects of particle deposition and clogging are exacerbated in narrower channels, however, the microreactors are limited in practice to hydraulic diameters of >50 μm. Several groups have investigated various channel cross sectional geometries to reduce the distribution of velocities, but particles flowing laminarly near a wall will always have longer residence times than those in the center.

6.3.1 Internal convection with staggered herringbone mixers

Because radial diffusion is still relatively slow in microchannels with d_h > 50 μm, inducing convection in the channel's cross-sectional plane could narrow the distribution of particle velocities. Furthermore, by inducing internal convection within the microchannels, particles would be less likely to become overgrown and aggregate on channel walls. As a case study, I attempted to induce convection using the staggered herringbone mixers (SHMs) developed by Stroock *et al.*[2] over the entire length of the T4EV1a reaction channel for rapid CdTe tetrapod growth (Figure 5.3b).

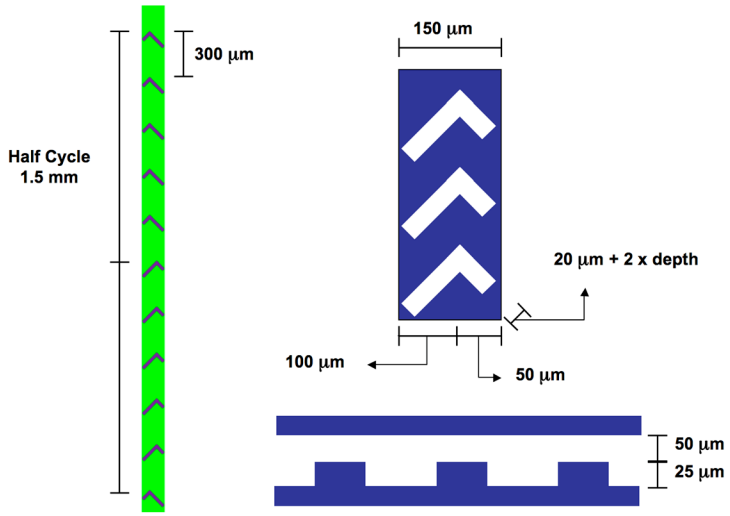

Figure 6.1. Staggered herringbone mixer schematic. Dimensions are shown for the mask pattern; due to isotropic etching, actual widths are increased by twice the etch depth (50 μm). The 25 μm-deep herringbones are fabricated on a separate wafer from the 50 μm channels, and the two wafers are aligned before bonding.

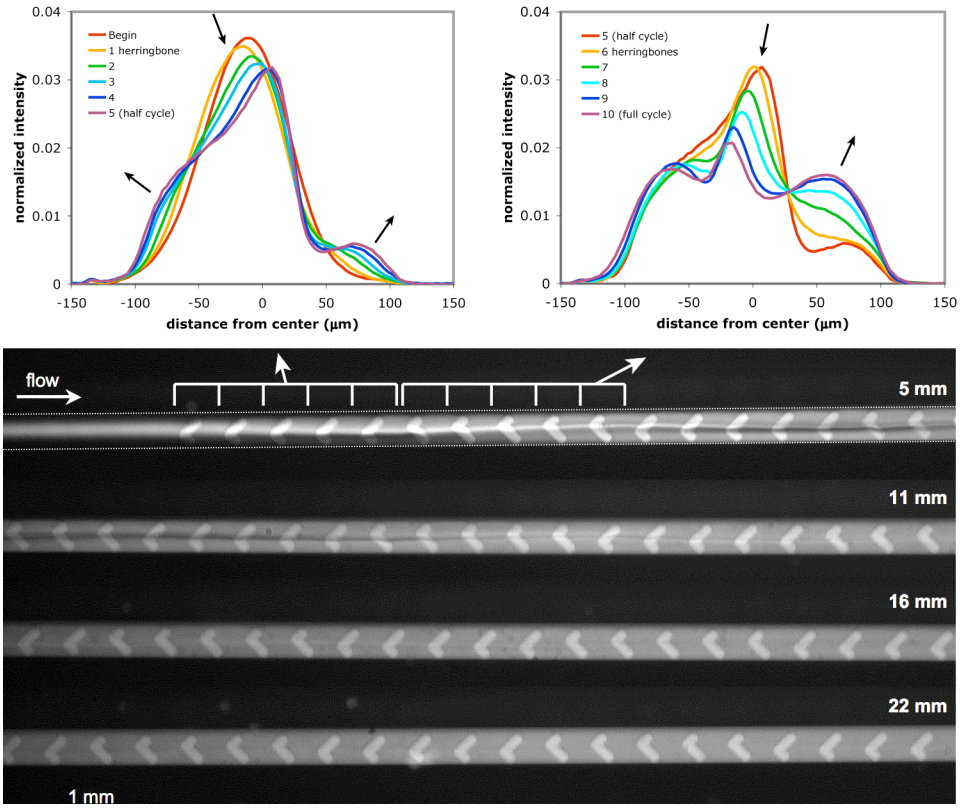

Figure 6.2. Fluorescence micrographs and cross-sectional intensity profiles of the staggered herringbone mixing of CdSe spheres in toluene at room temperature. The micrograph represents a single channel broken up into four segments, with the dotted lines marking the walls of the 0-5 mm channel. The channel is 250-μm wide and 50-μm deep with 25 μm-deep herringbones. The nanoparticle solution is injected in the center inlet of a sheath injector at 1 μL/min, and pure toluene is pumped in the two sheaths at 1 μL/min each, for a total flow rate is 3 μL/min.

Previously, I incorporated shallow (~5 μm) SHM structures at the head of the sheath injection microreactor, but I never characterized their effectiveness, which was most likely minimal. Deeper (25 μm) staggered herringbones, whose mask dimensions are shown in Figure 6.1, were fabricated using a two-wafer process, and fluorescence microscopy (λ_{3x} = 488 nm, Ar^+ laser) was used to characterize the efficiency of mixing a focused stream of nanoparticles. Figure 6.2 presents the fluorescence profiles of 3 nm-diameter CdSe nanoparticles in toluene mixing with pure toluene in a sheath injection reactor at room

temperature. In the presence of 25 μm-deep herringbones, the profiles clearly show induced convection across the channels after a single cycle of 10 herringbones. At 3 μL/min (3.7 mm/s), the laminar stream of CdSe nanocrystals is mixed substantially after 11 mm (3 s) and is completely homogenous after 22 mm (6 s). Longer mixing distances are required when using shallower herringbones or faster flow rates. The 6 s residence time and 22 mm channel length required for complete mixing, however, is the same length as a T4EV1a microreactor and is far too slow to substantially reduce hydrodynamic dispersion or deposition during growth.

Despite this inefficient mixing, I attempted to synthesize CdTe tetrapods in rapid tetrapod evolution chips equipped with SHMs, which were etched to 25-μm depth to maximize convection. Surprisingly, the resulting tetrapods were more polydisperse than the original syntheses. The absorption spectrum in Figure 6.3a displays a multiple exciton peaks, suggesting that particles were trapped in the large dead volumes of the herringbones for large periods of time. Such a bimodal distribution is not obvious in the TEM images (Figure 6.3b) of the products, but the quality of the tetrapods was not substantially improved compared to those produced without SHMs. The microchannels also clogged rapidly, and copious brown deposits were observed in the recessed herringbones, suggesting that the herringbones actually contributed to the reactor fouling rather than preventing it.

Due to their slow convection as well as the retention of particles in their dead volumes, SHMs in glass microchannels proved to be inadequate for reducing the RTD and particle deposition. At low *Re*, it is unlikely other micromixing and profile-shaping schemes will substantially reduce the RTD limitations in continuous flow reactors. An alternative method is to flow discontinuous plugs that mix rapidly due to internal convection, as shown in Figure 6.4.

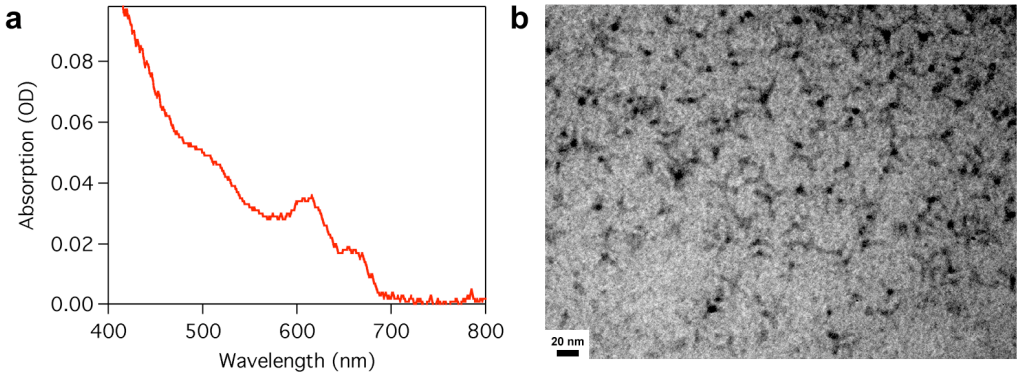

Figure 6.3. (a) Online absorption spectrum and (b) TEM image of CdTe tetrapods synthesized at 260 °C for 6 s (3 μL/min) in a micromixing T4EV1b chip fabricated with 25 μm-deep staggered herringbone mixers.

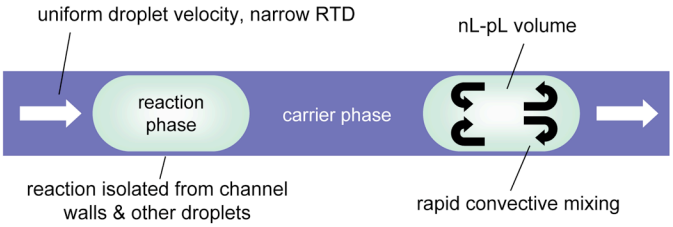

Figure 6.4. Two-phase plug flow for narrow residence time distribution and rapid mixing.

6.4 CONCLUSION

Efforts to prevent nanoparticles from adhering or nucleating on channel walls were unsuccessful, as were attempts to reduce the residence time distribution. The least deposition was observed when using oleic acid and octadecene in FDTS-silanized channels. Functionalizing channel walls did not completely eliminate particle aggregation, however, and no general additive was found to increase nanoparticle solubility without altering the syntheses. Attempts to reduce the residence time distribution were similarly fruitless, since diffusion and dispersion in the axial direction will occur in any continuously flowing liquid, regardless of the ingenuity of microfluidic structures.

I therefore conclude that the only robust method to avoid deposition is to prevent nanoparticles from contacting solid surfaces, and the only method to prevent dispersion is to physically isolate reaction volumes along the direction of flow. In the next chapter, I will discuss how segmented flow reactors were used to accomplish these strategies and successfully reduce both deposition and residence time distribution.

6.5 REFERENCES

(1) Grover, W. H.; Skelley, A. M.; Liu, C. N.; Lagally, E. T.; Mathies, R. A. *Sens. Actuator. B-Chem.* 2003, *89*, 315.

(2) Stroock, A. D.; Dertinger, S. K. W.; Ajdari, A.; Mezic, I.; Stone, H. A.; Whitesides, G. M. *Science* 2002, *295*, 647.

Chapter 7 High-Temperature Microfluidic Synthesis of CdSe Nanocrystals in Nanoliter Droplets

7.1 INTRODUCTION

The compartmentalization of reagents in nanoliter and sub-nanoliter volumes is valuable for enhancing and controlling chemical reactions.[1] Reactions in emulsions suspended in bulk fluid, however, are limited by dynamic exchange, phase diagram constraints, and by the inability to manipulate and monitor the individual nanoreactors. Microfabricated devices are now being used to perform reactions in microliter to nanoliter volumes, demonstrating enhanced reaction yield, selectivity, and kinetics.[2-6] Microfluidics have also been used to generate and control stable, isolated droplets and emulsions[7-9] for biological analysis,[10] crystallization,[11] and chemical synthesis.[5, 12] These systems commonly use water, mild temperatures, and polymeric substrates. Many reactions, however, such as the inorganic nanoparticle synthesis considered here, require organic solvents, elevated temperatures, and air- and water-sensitive reagents. A more general and robust method for performing reactions in nanoliter volumes under challenging conditions must be developed.

Continuous flow microreactors have been used to rapidly grow and characterize inorganic nanocrystals.[13-19] The synthesis of semiconductor nanocrystals in microfluidic systems provides a stringent test for advanced microfluidic techniques, because such

reactions are extremely sensitive to synthetic conditions, involve high temperatures, caustic precursors, and rapid kinetics, and because these reactions produce products that are continuously distributed in size.[15] In continuous flow microreactors, the particle size distribution is further broadened by the velocity and residence time distributions inherent to pressure-driven flow.[15, 20] Particles can also nucleate and deposit on channel walls, leading to runaway growth, clogging, and unstable reactor conditions, particularly at high temperatures and in small channels.[12, 17]

Segmented-flow microfluidics present a potential remedy for the dispersion and deposition challenges inherent to nanoparticle synthesis in microfluidic systems. Gas bubbles introduced in microreactor flows can reduce nanoparticle size distribution.[16, 21, 22] Gases, however, change volume significantly with pressure and temperature.[22] Moreover, liquid slugs in such systems still physically contact reactor walls and neighboring slugs, allowing for particle deposition and dispersion.[23] Alternatively, the encapsulation of precursor solutions in nanoliter-scale droplets flowing in a carrier fluid physically and temporally isolates reactants so that they do not interact with channel walls and so that they can be transported without cross-contamination.[24] Such droplets can be generated in microfluidic devices by shearing a stream of the droplet phase with the flow of the continuous phase via cross-flow[8, 25] or via flow-focusing[9, 26] geometries. While droplet-based microfluidics have been used to synthesize nanoparticles at room temperature in aqueous solutions,[12, 27] these systems are not compatible with the pyrolytic synthesis of high quality semiconductor nanocrystals. For high-temperature synthesis, the droplet and carrier fluids must be stable, non-interacting, non-volatile, liquid, and immiscible from ambient to reaction temperatures (~300 °C). Octadecene (ODE) has been used as a non-coordinating solvent for high-temperature semiconductor nanocrystal synthesis in bulk fluids,[28, 29] making it a suitable droplet phase.

Long-chain perfluorinated polyethers (PFPE's) are liquid, essentially inert, and immiscible with nearly all non-fluorous solvents under nanocrystal synthesis conditions, making them ideal carrier fluids.

To synthesize nanocrystals in droplets at high temperatures in this system, droplets must be generated despite the low interfacial tensions (5-25 mN/m) of the organic/fluorous solvent pair and the large viscosities (>100 mPa·s) of high-boiling PFPE's. The competition during droplet formation between viscous forces and interfacial tension can be expressed by the capillary number, $Ca = U\mu/\gamma$, where U is the linear flow velocity, μ is the viscosity of the carrier fluid, and γ is the interfacial tension between the two fluids. At high μ and low γ, relatively low flow rates result in high Ca (>0.1), which can promote the laminar flow of parallel, immiscible streams.[9, 30] Droplet formation is discouraged at high Ca because the capillary velocity (γ/μ) is not fast enough relative to U to relax the strained interface into droplets.[30] Droplet formation is also hindered when the viscosity ratio, $\lambda = \mu_{drop}/\mu_{carrier}$, is very low (<0.05).[31] To rupture the interface at low viscosity ratios, the shear rate can be increased by narrowing microchannel dimensions (<50 μm), but this can generate high pressures when viscous PFPE's are used as carrier fluids. Thus, to synthesize nanocrystals in droplets at high temperatures, a method to reproducibly generate droplets at high capillary numbers and low viscosity ratios must be developed.

In this work, we demonstrate successful droplet formation and flow in a high-temperature microreactor using solvents and conditions that are appropriate for the nanoliter-scale synthesis of CdSe nanocrystals. Using a stepped microstructure, controlled streams of octadecene droplets are reproducibly generated in perfluorinated polyether at low viscosity ratio and high Ca. CdSe nanocrystals are synthesized at high temperature in droplet-based microreactors to demonstrate the compatibility of our droplet fluids. The benefits of

performing high-temperature nanocrystal synthesis in self-contained nanoliter-scale reaction volumes are discussed in the context of other chemical and biochemical reactions where the physical, temporal, and thermal control and isolation of nanoliter-scale reaction volumes are critical elements.

7.2 EXPERIMENTAL

7.2.1 Microreactor design and fabrication

To make droplets of ODE in PFPE at high capillary numbers, we fabricated glass microreactors using the mask pattern shown in Figure 7.1a. Droplets of the dispersed reactant phase are produced in the cross-shaped nanojet droplet generator (magnified in Figure 7.1b), which is an extension of the designs developed by Tan *et al.*[26, 32] The perfluorinated polyether (PFPE) carrier fluid is injected into the side arms of the cross, while the dispersed reactant phase is injected at the top of the cross. The hydrodynamic focusing and shearing of the dispersed phase stream at the narrow, 160 μm-wide constriction, coupled with the equilibrating effects of surface tension as the jet nozzle expands, leads to droplet production. From the end of the 2.4 mm-long nozzle, the generated droplets then travel through a 200 μm-wide heated serpentine channel whose semi-circular turns are intended to induce mixing in the droplets.[33] The angled brackets in Figure 7.1a represent the boundaries of a 2.5 x 1 cm Kapton thin film heater (Minco) that heats the 107 mm-long, 1.7 μL reaction channel from the bottom of the chip.

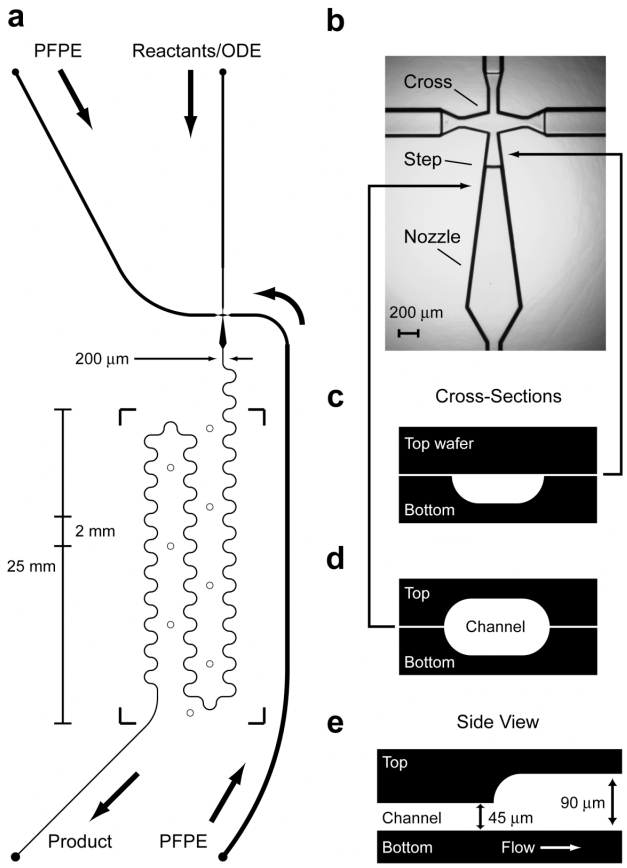

Figure 7.1. Microreactor channel design with droplet jet injector. (a) Channel schematic showing dimensions, inlets (●), thermocouple wells (○), and boundaries of Kapton heater (square brackets). (b) Optical micrograph of droplet injection cross. Octadecene is injected in the top channel, while the PFPE is injected in the side channels. The narrowest point is 160 μm wide. (c) Lateral "D"-shaped cross section of channel etched on the bottom wafer only. (d) Cross-section of ellipsoidal channel etched on both top and bottom wafers. (e) Axial cross-section showing the 45 μm step up in channel height.

To prevent continuous filaments of the dispersed phase from flowing laminarly through the entire channel at high *Ca*, a sharp increase in height is fabricated 400 μm after the beginning of the nozzle. Such an out-of-plane expansion has been shown to produce monodisperse emulsions in viscous carrier fluids,[7] analogous to the function of the in-pane expansion. The locations of these "steps" in channel height are clearly visible as black lines in the micrograph in Figure 7.1b. The cross-section illustrations in Figure 7.1c-e show the geometrical details of the step in the nozzle.

Microfabrication

To fabricate this multi-level structure, two masks were used to pattern two separate wafers following a protocol published previously.[34] The top mask is nearly identical to the continuous bottom mask (Figure 7.1a) except that the top pattern does not extend to the cross region. Concentrated (49%) HF was used to etch 1.1 mm-thick borofloat glass wafers (Precision Glass & Optics) to a depth of 45 μm using standard planar photolithographic methods. The etched surfaces of the top and bottom wafers were placed in contact, and the channels were aligned manually under a microscope to a precision of ±5 μm. The aligned wafers were thermally bonded to enclose the channels.

As seen in the axial cross-section (Figure 7.1e), this procedure produces a step increase in channel height from 45 to 90 μm after the cross. The isotropic wet etching results in channels with D-shaped cross sections in the single-etched cross region (Figure 7.1c) and channels with ellipsoidal cross sections where two D-shaped channels are aligned (Figure 7.1d). Channel widths refer to the maximum width.

Silanization

Stable droplet flow can only be obtained when the continuous phase (PFPE) preferentially wets the channel surface.[35] Therefore, the glass surface of the microchannels was silanized with a Teflon-like coating of 1H,1H,2H,2H-perfluorodecyltrichlorosilane (FDTS, Lancaster) using the procedure described in Section 3.4. Silanization of microreactor walls was verified by observing the preferential wetting of the fluorinated phase under a microscope.

7.2.2 Droplet production & characterization.

Droplets were generated by pumping filtered ODE and Fomblin Y 06/6 PFPE through a freshly silanized chip at rates from 0.1 to 20 μL/min using three, 500-μl Hamilton gastight syringes loaded in two syringe pumps (BAS). Syringes were interfaced to the chip via PEEK fittings (Upchurch) and a custom aluminum manifold.

Capillary numbers were calculated using the average linear fluid velocity at the nanojet constriction and the values of μ and γ at 20 °C. The viscosity of Fomblin Y 06/6 (avg. MW = 1800) at 20 °C is 113 mPa·s, compared to 4 mPa·s for octadecene, resulting in $\lambda = 0.035$.[37] The interfacial energy between ODE and Fomblin Y 06/6 at 20 °C is 8.3±0.3 mN/m, as measured with a KSV Sigma 701 tensiometer using the Du Nouy ring method.[38]

At high *Ca*, laminar flow was observed and, once established, remained stable even after conditions were returned to those known to favor droplet formation. To prevent such hysteresis, the ODE flow was stopped each time the flow rate was changed until the nanojet

was purged of ODE. After restarting the ODE flow, the system was allowed to equilibrate for 2 min before observations and images were recorded.

Droplet formation was observed at room temperature using a Nikon Eclipse E800 microscope. Images were captured with an Evolution MP CCD camera (MediaCybernetics) with an integration time of 1.6 ms. Image Pro Plus software (MediaCybernetics) was used to acquire droplet images and perform droplet sizing. Droplet formation at high temperature was characterized through the objectives and with low-resolution images.

7.2.3 Nanocrystal Synthesis

Reagents

Cadmium oxide powder (99.99+%), selenium powder (99.999%), oleic acid (90%), anhydrous isooctane (2,2,4-trimethylpentane, 99.8%), HPLC-grade acetone (99.9+%), 1-octadecene (>95%), and Fomblin Y 06/6 perfluorinated polyether were purchased from Sigma-Aldrich. Tri-n-octylphosphine (97+%) was purchased from Strem. Fomblin Y06/6 and all reaction solutions were degassed under vacuum to remove air and water and then stored in an argon-filled glovebox. Before synthesis, all solutions were degassed again to prevent bubble evolution and filtered with 0.45 μm syringe filters (Pall) to prevent clogging.

Stock solution preparation

60 mg of CdO, 1.0 g of oleic acid, and 1.90 g of octadecene (ODE) were heated to 200 °C under argon to form a clear yellow cadmium oleate stock solution that contained 132 mM cadmium with 7:1 oleic acid:Cd mole ratio. A 43 mM selenium stock solution was prepared by mixing 0.65 g of degassed octadecene with 0.034 g of a solution of tri-*n*-octylphosphine selenide (TOPSe) in tri-*n*-octylphosphine (TOP) that was 10% Se by weight. For some experiments, the Cd and Se stock solutions were diluted three-fold by adding additional octadecene.

Synthesis apparatus & procedure.

In a typical experiment, Harvard Apparatus Pump 11 Pico Plus syringe pumps injected separate streams of Cd and Se stock solution at equal rates into a PEEK tee. The combined 66 mM Cd, 22 mM Se solution, referred to here as the "ODE flow," was pumped into the reactant inlet of the chip. Fomblin Y 06/6 PFPE was pumped into the chip using a Harvard PHD2000 pump, with the ODE:PFPE flow rate ratio kept constant at 1:4 for all nanocrystal syntheses. Pumping and all other chip functions were computer-controlled through a master LabView virtual instrument (VI) (National Instruments).

The thin-film heater was powered by a programmable power supply (Instek) whose voltage was PID-controlled by the master LabView VI. Reactor set point temperatures ranged from 240 to 300°C and were measured by 36 gauge thermocouples (Omega) embedded at channel depth in drilled holes in the center of the heated region. Thermocouples placed near the edges of the heater measured a drop of approximately 50 °C from the center.

The droplet residence time at 1.25 μL/min total flow rate was measured by timing many individual droplets as they traveled through the reaction channel. Residence times for high flow rates were extrapolated from this value, and measurements at medium flow rates validated the accuracy of this method. Droplets of product solution were output into a capillary flow cell attached to a CCD spectrometer (Ocean Optics) for fluorescence detection (380 nm excitation). Reaction product was collected from the end of the capillary in a vial under nitrogen.

Cleaning & characterization

In a glovebox, the product mixture was centrifuged, and the top, colored ODE phase was separated, precipitated with acetone, and centrifuged again to form a clean pellet of nanocrystals. A minimum of 20 μl of nanocrystal solution (100 μl of raw product mixture) was necessary for adequate pellet formation. Cleaned nanocrystals were characterized with a Tecnai G^2 20 transmission electron microscope (FEI) at 200 KV beam acceleration. UV-visible absorption spectra on cleaned aliquots were recorded in quartz cuvettes on an Agilent 8453 spectrophotometer.

7.3 RESULTS & DISCUSSION

7.3.1 Droplet formation at ambient temperature.

Using a nanojet injector modified with a downstream step (Figure 7.1), our microreactor successfully generated steady, controlled streams of ODE droplets in PFPE carrier fluid. Figure 7.2 presents optical micrographs of small, spherical droplets and large, oblong droplets flowing through the main reactor channel without interacting with each other. The 53 μm-diameter, 78 pL droplets in Figure 7.2a were formed with 0.1:2 μL/min ODE:PFPE and the 300 μm-long, 135 μm-wide droplets in Figure 7.2c were formed with 1:2 μL/min ODE:PFPE.

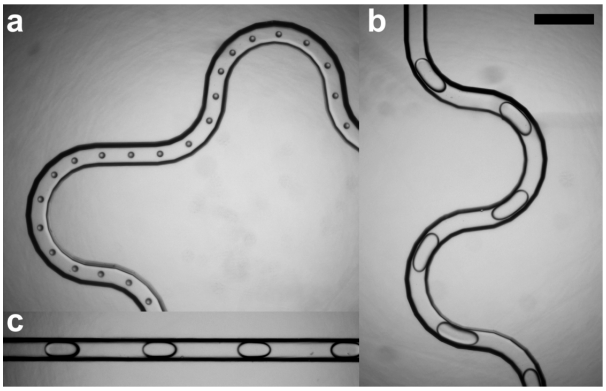

Figure 7.2. Droplet images in main channel at the following ODE:PFPE flow rates: (a) 0.1:2 μL/min, (b) & (c) 1:2 μL/min. Droplets were generated at capillary numbers of (a) 0.075, and (b) & (c) 0.11. Scale bar = 500 μm.

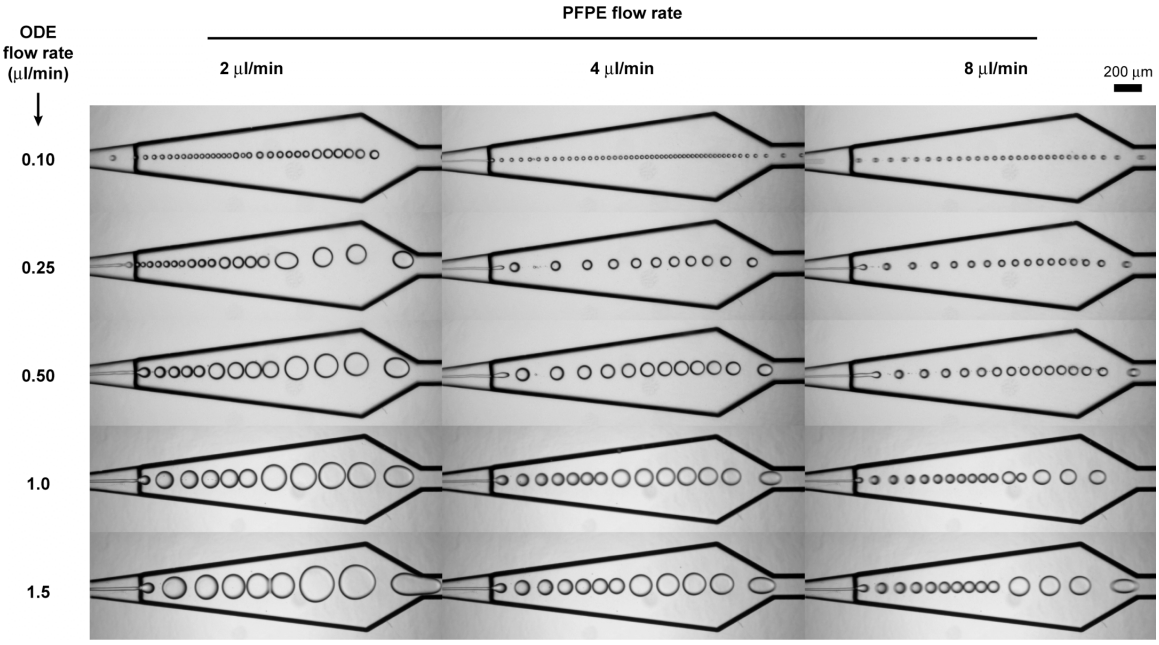

Figure 7.3. Optical micrographs of droplet formation at the indicated ODE and PFPE flow rates. The maximum Ca shown is 0.34 for 1.5:8 ODE:PFPE.

The expansion step in particular allowed the nanojet to generate droplets over a wide range of flow rates and capillary numbers (*Ca*). Figure 7.3 shows optical micrographs of droplets being generated in the nanojet nozzle at room temperature with ODE flow rates ranging from 0.1 to 1.5 μL/min and total PFPE flow rates from 2 to 8 μl /min. In these frames, the capillary number, which is proportional to total flow rate, ranges from *Ca* = 0.075 to 0.34. As illustrated in Figure 7.3, droplet size increases with increasing ODE flow rates and decreasing PFPE flow rates. In Figure 7.3, droplet diameters range from 37 μm (0.1:8 μL/min ODE:PFPE) to 284 μm (1.5:2 ODE:PFPE), corresponding to volumes of 27 pL to 5 nL, respectively.[39] When the total flow rate was kept constant, droplet size increased with the "ODE fraction" -- the ratio of the ODE volumetric flow rate to the total flow rate. When the ODE fraction was kept constant, the final droplet size exiting the nozzle did not

vary significantly with the total flow rate. Many frames in Figure 7.3 also show the consistent, sequential fusion of smaller droplets into larger droplets,[39] which enables the predictable formation of larger droplets without increasing the ODE fraction. Thus, by using this modified nanojet, we can tune the size of ODE droplets independently from flow rate, even at high capillary numbers.

As the ODE fraction and flow rate are increased, droplet generation passes through four distinct phases: (I) droplet separation before the step, (II) step-induced separation in the first half of the nozzle, (III) separation in the second half of the nozzle, and (IV) laminar flow. At the lowest ODE and PFPE flow rates (Phase I, e.g. 0.1:2 ODE:PFPE in Figure 7.3), droplets formed before the microfabricated step in the nanojet nozzle. At moderate flow rates and ODE fractions (Phase II, e.g. 1:2 ODE:PFPE), the ODE stream formed a thin filament that only broke off into droplets at the step. Occasionally, the filament extended slightly past the step, as shown with 0.5:8 ODE:PFPE. In these cases, the microfabricated step instigated long-wavelength undulations that eventually degenerated into droplets due to Rayleigh capillary instability.[40] At higher ODE fraction and flow rates (Phase III), laminar filaments broke off into droplets in the second half of the nozzle or at the head of the reaction channel. At the highest ODE fraction and total flow rates (Phase IV), filaments extended across the entire nozzle and through the entire length of the reaction channel.

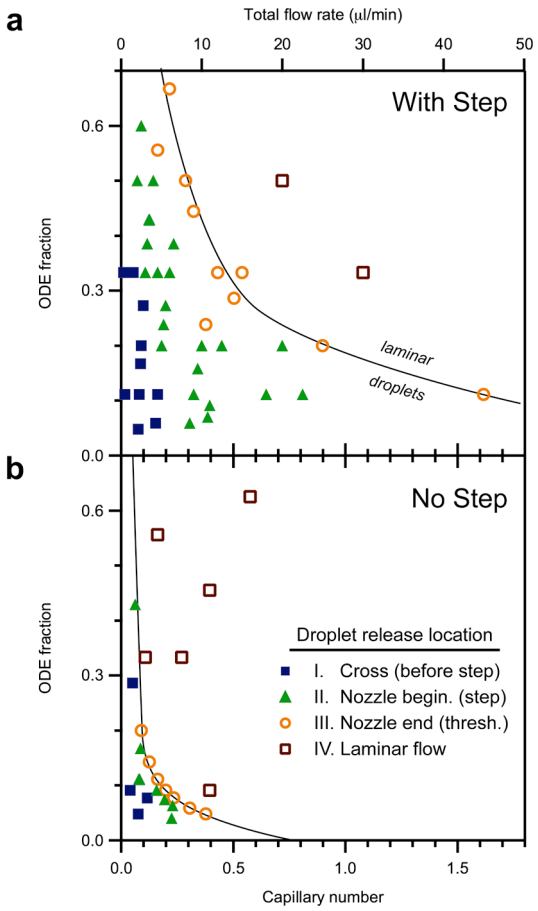

Figure 7.4. Phase diagrams showing the location of droplet separation for (a) a 90 μm-deep channel with a 45 μm step, and (b) an equivalent 45 μm-deep channel with no step. The line drawn through the threshold region (III) distinguishes the laminar flow regime (IV) from droplet regime (I & II).

The phase diagrams in Figure 7.4 summarize these four regimes as a function of ODE fraction and *Ca*. Here we consider Phases I and II to be clean droplet separation and Phase III to be the transition region before the laminar flow of Phase IV. Figure 7.4a clearly shows the regions of clean droplet separation at low ODE fraction or low *Ca*, as well as the regions of laminar flow at high ODE fraction and *Ca*. In comparison, using a 45 μm-deep microreactor without a step (Figure 7.4b), the same sequence of phases is observed, but the area of the phase diagram that cleanly generates droplets shrinks to a small fraction of the

analogous area in Figure 7.4a. With the step, reproducible droplet separation was observed at *Ca* up to 0.81 at ODE fraction = 0.11. At the same ODE fraction without the step, clean separation was only observed up to *Ca* = 0.08, and did not extend past *Ca* = 0.22 even at lower ODE fractions. With the step, droplet formation was observed at ODE fractions up to 0.6 at *Ca* = 0.13, compared to ODE fraction = 0.167 without the step. These dramatic differences explain why laminar flow was observed for most *Ca* when flowing ODE and PFPE in nanojet structures without the step modification. As intended, the step expands the available phase space for droplet formation, particularly along the *Ca* axis.

Our step-modified nanojet generated droplets at *Ca* (0.81), comparable to the highest values reported for other microfabricated devices, and at a significantly lower viscosity ratio. Zheng *et al.* observed droplet formation in viscous carrier fluids (λ =0.11) up to *Ca* = 0.11,[11] which is consistent with the maximum *Ca* = 0.08 that we observed at the same volume fraction without the step. Anna *et al.* demonstrated droplet formation up to *Ca* ~1.0,[9] but with a much less viscous carrier fluid (μ = 6 mPa·s) and a viscosity ratio (λ =0.17) five times higher than the λ for ODE/PFPE.

Clearly, the microfabricated step in our nanojet device plays an integral role in disrupting the laminar filaments observed at high *Ca*. The rapid expansion in channel height,[7] coupled with the sudden reduction in flow velocity and *Ca*,[41] forces the end of the filament to expand into a bulbous shape at the step. As observed by Stone *et al.*, the inhomogeneous Laplace pressure resulting from this bulbous end, along with the sharp corner of the step, generates a narrow "neck" that is a prerequisite for droplet formation.[41] The decreased flow velocity relative to the capillary relaxation velocity allows surface tension time to pinch off the neck and release droplets.

7.3.2 High temperature droplet formation.

Nanoliter droplets of ODE were also generated successfully in PFPE when the reaction channel was heated to temperatures up to 300 °C. Because surface tension and viscosity are temperature-dependent, the nanojet injector itself was not directly heated (Figure 7.1a) in order to maintain the droplet generation behavior previously observed at room temperature. As the droplets entered the heated reaction channel, thermocapillary effects[42] resulting from the temperature gradient caused small droplets to fuse. The resulting droplets filled the width of the channel, which had the beneficial effect of making the droplets flow closer to the average linear velocity in the channel. The aspect ratios of the resulting droplets were 1-2 under most conditions, but increased to 4 at extremely low flow rates (~1 μL/min). Outside of the regions of steeply increasing temperature, droplets did not combine again in the reaction channel. The perfluoroalkysilane coatings on the channel walls maintained their surface properties for approximately 5 hours, after which the ODE droplets began wetting the surface of the channel, resulting in irregular or laminar flow. Contact angle experiments on flat substrates confirmed that after heating for > 5 hours, the perfluoroalkylsilanes were almost completely removed in the presence of PFPE at high temperature.

7.3.3 High temperature nanocrystal synthesis.

After confirming that droplet flow remained stable at high temperatures and capillary numbers, we demonstrated the ability to synthesize CdSe nanocrystals at high temperature in nanoliter-scale droplets. Cd/Se precursor solutions formed stable, distinct, nanoliter droplets in PFPE, and the solutions reacted consistently when heated to produce faint orange or red droplets of nanocrystal solution. The PFPE did not dissolve or mix with any of the reagents in the high temperature microreactor and did not show the typical signs of thermal degradation,[43] such as vigorous bubbling.[44] The nanocrystal/ODE phase was easily separated from the clear PFPE phase for cleaning. The TEM micrographs of cleaned product in Figure 7.5 show nicely ordered arrays of 3.8 nm-diameter CdSe nanocrystals synthesized in ODE droplets for 10 s at 300 °C. A high-resolution image (Figure 7.5 inset) of a 3.4 nm-diameter nanoparticle grown at 260 °C displays the characteristic hexagonal symmetry of the wurtzite crystal phase typically found in CdSe nanocrystals synthesized at high temperature.

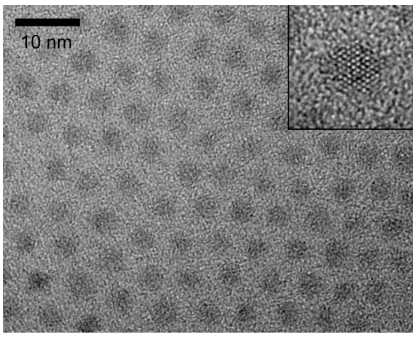

Figure 7.5. Transmission electron micrographs of CdSe nanocrystals synthesized in droplets of ODE in PFPE in a 290°C microreactor. Inset: high resolution image of a 3.4 nm-diameter nanocrystal.

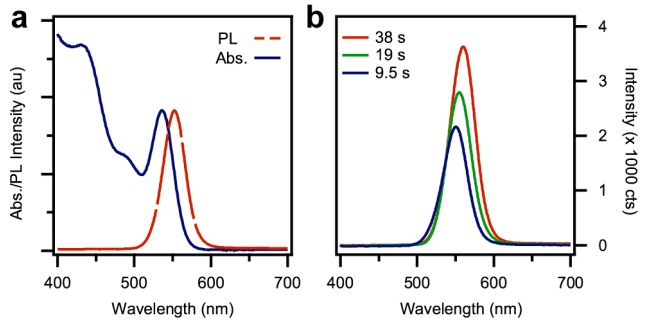

Figure 7.6. (a) On-line photoluminescence spectrum and off-line absorption spectrum of nanocrystals grown in droplets for 19 s at 280°C. (b) On-line photoluminescence spectra of nanocrystals grown at 290°C with three different flow rates and residence times.

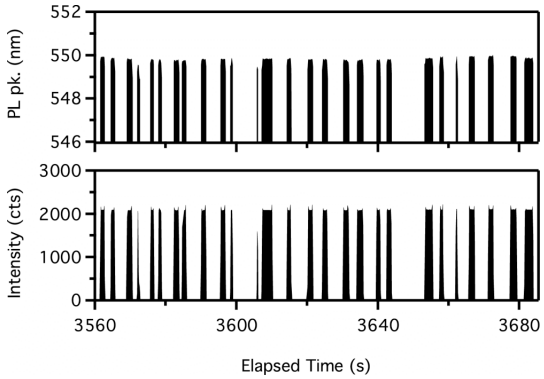

Figure 7.7. Photoluminescence time traces showing peak wavelength (top) and intensity (bottom) data as individual drops of synthesized nanocrystals pass through the flow cell. The flow rates were 0.25:0.25:2 μL/min Cd:Se:PFPE. Spectral data and conditions correspond to the 19 s run from Figure 7.6b.

Figure 7.6a shows absorption and photoluminescence (PL) spectra for nanocrystals synthesized in nanoliter-scale droplets for 19 s at 280 °C. To synthesize these nanocrystals, 132 mM Cd and 43 mM Se stock solutions were injected at 0.25 μL/min each, while the PFPE was pumped at 2 μL/min. The off-line absorption and on-line fluorescence spectra exhibit the sharp, distinctive peaks of fairly monodisperse nanocrystals. The PL full width at

half maximum (fwhm) of 34 nm is comparable to those seen with the analogous flask and continuous flow syntheses and demonstrates the superior optical properties of nanocrystals synthesized in high temperature microreactors, compared to those synthesized in low temperature chips.

Figure 7.6b shows on-line PL spectra for nanocrystals synthesized at 290 °C at three different residence times, which varied with total flow rate. The fluorescence spectra in Figure 7.6b show that, as the residence time increases, the peak intensity increases, and the emission peaks shift from 550 to 555 to 560 nm as the residence times are increased from 9.5 to 19 to 38 s, respectively. The relatively small shift in the emission peaks implies that the reaction is close to completion after only 9.5 s of growth. This agrees with our general observation that CdSe reactions involving Cd-oleate occur very rapidly due to the weak coordination of the oleic acid surfactant. In addition, the relatively high oleic acid:Cd ratios (7:1) used are believed to encourage Ostwald ripening,[28] which can explain why the PL peaks in this particular reaction system are not significantly narrower when using droplets.

The synthesis of CdSe nanocrystals in discrete, uniformly flowing, nanoliter-volume droplets theoretically allows for the precise characterization of such rapid growth on the single-drop level. The PL spectra in Figure 7.6b were recorded on-line as droplets of nanocrystal product flowed out of the microreactor. Spectra of droplets in the capillary flow cell were resolved at time resolutions down to 250 ms. Figure 7.7 shows the peak wavelength and intensity time traces for droplets of nanocrystals flowing at 0.5:2 μL/min ODE:PFPE at 290 °C, which corresponds to the 19 s spectrum in Figure 7.6b. The intermittent spikes in the peak wavelength and intensity traces show individual droplets as they passed through the detector. Over the course of the 120 s window shown in Figure 7.7, the PL intensity of each

droplet was very reproducible, and the peak wavelengths did not shift significantly -- the ±0.3 nm variation was comparable to the resolution of the spectrometer and precision of peak-fitting algorithm. The length of the droplets (~1 s) and the occasional variations in their periodicity are consistent with the observation that droplets from the microreactor combined on the order of 10 times outside of the reactor as they flowed through the 500 μm-wide exit via and the external capillary. Because this abrupt widening occurred at room temperature, this droplet fusion would not affect growth kinetics or broaden the PL peaks of the resulting drops under stable growth conditions. PL peaks for droplets of nanocrystals were observed to remain stable over several hours and hundreds of droplets. On-line spectroscopy is an invaluable diagnostic tool for microreactor synthesis, because the growth and PL spectra of nanocrystals are extremely sensitive to changes in channel conditions caused by bubble formation, channel obstruction, degrading surface properties, and most significantly, deposition of nanocrystals on channel walls. The stable traces confirm our visual observations that, over the span of four hours, none of these phenomena occurred in amounts significant enough to perturb high temperature droplet synthesis. In contrast, using analogous conditions in a continuous flow reactor, an opaque layer of nanocrystals forms after ~20 minutes at the head of the heated region, resulting in the shifting and broadening of the PL peak.

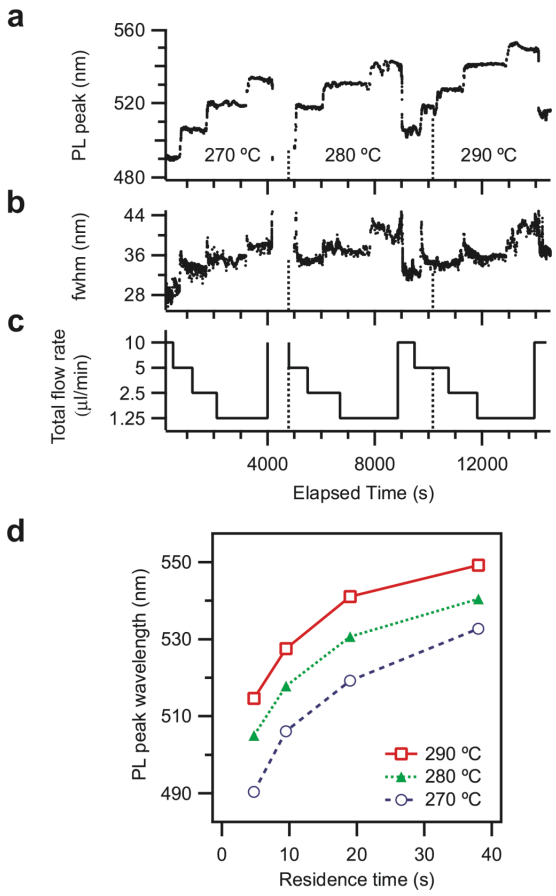

Figure 7.8. Photoluminescence time traces of nanocrystal drops demonstrate how (a) peak wavelength and (b) full width at half max vary with (c) total flow rate at three different temperatures. The discontinuity at 4000 s marks a break for syringe refilling. (d) Kinetic growth curves (peak wavelength vs. residence time) can be obtained for three temperatures using the data from (a) and (c).

Figure 7.8 shows that, with the stability of our droplet microreactor, we can test four different flow rates and three different temperatures in a single 4-hour experiment. In order to obtain a wider range of nanocrystal sizes, the concentrations of the Cd and Se stock solutions were diluted three-fold compared to the synthesis associated with Figure 7.6. Figure 7.8 shows that, as the total flow rates are halved sequentially from 10 to 1.25 µL/min and the temperature is increased in 10 °C increments from 270 to 290 °C, the nanocrystal

PL peak wavelength increases in distinct steps that represent increases in nanocrystal diameter. The steps in these time traces are much sharper and the ~2-3 min equilibration time is 4 times shorter than the ~10 min previously reported[13] with continuous flow reactors because there is significantly less dispersion when using droplets. The remaining equilibration and lag times are attributed to the time needed stabilize the pressure and droplet flow as well as the relatively large volume (20 μL) of the capillary connecting the chip outlet and the flow cell. The fwhm traces (Figure 7.8b) demonstrate that the size distribution increases as the residence time and nanocrystal size are increased. This behavior is consistent with the rapid Ostwald ripening we observe with oleic acid. The broadening could have been exacerbated by the fact that the least consistent droplet fusion occurred at the lowest flow rate (1.5 μL/min). The stable PL peak wavelength time traces at each condition, even after several hours of synthesis, are possible largely because the encapsulation of growing nanocrystals in droplets prevents them from interacting with the channel walls.

The spectral data recorded in the single run shown in Figure 7.8a can be plotted as a peak wavelength vs. residence time graph (Figure 7.8d) that shows kinetic data for nanocrystal growth at three different temperatures. The three temperatures display similar growth curves that flatten at increased residence time, but the higher temperatures shift the traces to higher wavelengths. These curves are similar to the kinetic data reported in previous high-temperature nanocrystal syntheses,[28] which validates our experimental methods. More significantly, Figure 7.8 demonstrates that such data can be collected rapidly and precisely in large part because our microfluidic droplet reactor offers the flexibility and stability to test a wide range of conditions. Capillary numbers reached up to $Ca = 0.36$ and temperatures reached up to 290 °C – conditions not readily accessible using other droplet

technologies. The isolation of nanocrystals in discrete droplets allowed growth kinetics to be observed at short time scales and allowed the reactor to be run continuously for four hours at high temperature without cleaning. Thus, our ability to generate droplets of precursor solution in PFPE at high *Ca* significantly improves our ability to synthesize nanocrystals in high-temperature microreactors with a number of temperatures, residence times, and different reaction schemes.

7.4 CONCLUSION

We have demonstrated high-temperature synthesis of nanocrystals in a liquid-liquid segmented flow nanojet microreactor. Because the pyrolytic synthesis of high-quality nanocrystals requires extreme conditions, several key developments are introduced to integrate the CdSe nanocrystal synthesis with droplet-flow microreactors. First, organic and perfluorinated solvents are used to produce two-phase flows in microfluidic devices. Second, in order to flow droplets over a wide range of flow rates, a nanojet injector with an expansion step is used to produce droplets at a low viscosity ratio ($\lambda = 0.035$) and at capillary numbers (0.81) comparable to the highest reported values. The ability to form droplets at high *Ca* with immiscible, high-boiling solvents allows our microfluidic devices to maintain reproducible droplet flow at high-temperature. All of these developments are essential for the synthesis of inorganic nanocrystals in nanoliter droplets of organic solvents in perfluorinated fluids.

While the nanocrystals used to demonstrate this novel droplet reactor are comparable in monodispersity to those made in flask or continuous flow reactors, future

optimization of precursor and surfactant systems, as well as the integration of on-chip mixing, should allow for the synthesis of more monodisperse particles. On-chip optical spectroscopy[17] will allow the low-latency analysis of single drops, which will facilitate high-throughput screening of nanocrystals and growth conditions. While gas-liquid and liquid-liquid segmented flow reactors are complementary techniques, the isolation of nanoliter droplets from channel walls makes droplet-based reactors more robust, more general, and more suitable for rapid reactions. The current durability of our droplet reactors determined by the ~5-hour lifetime of the fluoroalkylsilane coating, but stabilization of the unfluorinated C_1 and C_2 atoms on FDTS should allow for extended droplet experiments.

The successful use of PFPE as the carrier fluid for nanoliter droplets has implications for other chemical or biochemical syntheses. With the appropriate PFPE carrier fluid, many reactions in aqueous or organic solution can be encapsulated in nanoliter droplets and heated to the desired reaction temperatures in order to exploit the advantages of microfluidic reactors. These capabilities should be useful in studies of a wide variety of chemical and biochemical reactions where small reaction volumes and small numbers of reactant molecules, isolation from container walls and other reaction volumes, and fine control of temperature and other conditions are of critical importance.

7.5 REFERENCES

(1) Lopez-Quintela, M. A.; Tojo, C.; Blanco, M. C.; Rio, L. G.; Leis, J. R. *Curr. Opin. Colloid Interface Sci.* **2004,** *9*, 264-278.

(2) Jensen, K. F. *Chem. Eng. Sci.* **2001,** *56*, 293-303.

(3) Haswell, S. J.; Middleton, R. J.; O'Sullivan, B.; Skelton, V.; Watts, P.; Styring, P. *Chem. Commun.* **2001**, 391-398.

(4) Pennemann, H.; Watts, P.; Haswell, S. J.; Hessel, V.; Lowe, H. *Org. Process Res. Dev.* **2004,** *8*, 422-439.

(5) Burns, J. R.; Ramshaw, C. *Lab Chip* **2001,** *1*, 10-15.

(6) Lagally, E. T.; Emrich, C. A.; Mathies, R. A. *Lab on a Chip* **2001,** *1*, 102-107.

(7) Sugiura, S.; Nakajima, M.; Iwamoto, S.; Seki, M. *Langmuir* **2001,** *17*, 5562-5566.

(8) Thorsen, T.; Roberts, R. W.; Arnold, F. H.; Quake, S. R. *Phys. Rev. Lett.* **2001,** *86*, 4163-4166.

(9) Anna, S. L.; Bontoux, N.; Stone, H. A. *Appl. Phys. Lett.* **2003,** *82*, 364-366.

(10) Grodrian, A.; Metze, J.; Henkel, T.; Martin, K.; Roth, M.; Kohler, J. M. *Biosens. Bioelectron.* **2004,** *19*, 1421-1428.

(11) Zheng, B.; Tice, J. D.; Ismagilov, R. F. *Anal. Chem.* **2004,** *76*, 4977-4982.

(12) Shestopalov, I.; Tice, J. D.; Ismagilov, R. F. *Lab Chip* **2004,** *4*, 316-321.

(13) Chan, E. M.; Mathies, R. A.; Alivisatos, A. P. *Nano Lett.* **2003,** *3*, 199-201.

(14) DeMello, J.; DeMello, A. *Lab Chip* **2004,** *4*, 11N-15N.

(15) Yen, B. K. H.; Stott, N. E.; Jensen, K. F.; Bawendi, M. G. *Adv. Mater.* **2003,** *15*, 1858-1862.

(16) Nakamura, H.; Yamaguchi, Y.; Miyazaki, M.; Maeda, H.; Uehara, M.; Mulvaney, P. *Chem. Commun.* **2002**, 2844-2845.

(17) Krishnadasan, S.; Tovilla, J.; Vilar, R.; deMello, A. J.; deMello, J. C. *J. Mater. Chem.* **2004,** *14*, 2655-2660.

(18) Wang, H. Z.; Li, X. Y.; Uehara, M.; Yamaguchi, Y.; Nakamura, H.; Miyazaki, M. P.; Shimizu, H.; Maeda, H. *Chem. Commun.* **2004**, 48-49.

(19) Okuyama, K.; Lenggoro, I. W. *Chem. Eng. Sci.* **2003,** *58*, 537-547.

(20) Levenspiel, O., *The Chemical Reactor Omnibook*. OSU Book Stores: Corvallis, OR, 1979; pp. 64.1-64.20.

(21) Yen, B. K. H.; Gunther, A.; Thalmann, M.; Bawendi, M. G.; Jensen, K. F. *8th International Conference on MicroTAS,* Malmo, Sweden, 2004. Vol. 2, pp 126-129.

(22) Gunther, A.; Khan, S. A.; Thalmann, M.; Trachsel, F.; Jensen, K. F. *Lab Chip* **2004,** *4*, 278-286.

(23) Khan, S. A.; Gunther, A.; Schmidt, M. A.; Jensen, K. F. *Langmuir* **2004,** *20*, 8604-8611.

(24) Harries, N.; Burns, J. R.; Barrow, D. A.; Ramshaw, C. *Int. J. Heat Mass Transfer* **2003,** *46*, 3313-3322.

(25) Tice, J. D.; Song, H.; Lyon, A. D.; Ismagilov, R. F. *Langmuir* **2003,** *19*, 9127-9133.

(26) Tan, Y. C.; Collins, J.; Lee, A. P. *7th International Conference on MicroTAS,* Squaw Valley, CA, 2003. Vol. 2, pp 963-966.

(27) Hung, L. H.; Tseng, W. Y.; Choi, K.; Tan, Y. C.; Shea, K. J.; Lee, A. P. *8th International Conference on MicroTAS,* Malmo, Sweden, 2004. Vol. 2, pp 539-541.

(28) Bullen, C. R.; Mulvaney, P. *Nano Lett.* **2004,** *4*, 2303-2307.

(29) Yu, W. W.; Peng, X. *Angew. Chem. Int. Ed.* **2002,** *41*, 2368-2371.

(30) Tice, J. D.; Lyon, A. D.; Ismagilov, R. F. *Anal. Chim. Acta* **2004,** *507*, 73-77.

(31) Bentley, B. J.; Leal, L. G. *J. Fluid Mech.* **1986,** *167*, 241-283.

(32) Tan, Y. C.; Fisher, J. S.; Lee, A. I.; Cristini, V.; Lee, A. P. *Lab Chip* **2004,** *4*, 292-298.

(33) Song, H.; Tice, J. D.; Ismagilov, R. F. *Angew. Chem. Int. Ed.* **2003,** *42*, 768-772.

(34) Simpson, P. C.; Roach, D.; Woolley, A. T.; Thorsen, T.; Johnston, R.; Sensabaugh, G. F.; Mathies, R. A. *Proc. Natl. Acad. Sci. U. S. A.* **1998,** *95*, 2256-2261.

(35) Dreyfus, R.; Tabeling, P.; Willaime, H. *Phys. Rev. Lett.* **2003,** *90*.

(36) Srinivasan, U.; Houston, M. R.; Howe, R. T.; Maboudian, R. *J. Microelectromech. Syst.* **1998,** *7*, 252-260.

(37) Specified by manufacturer.

(38) Harkins, W. D.; Jordan, H. F. *J. Am. Chem. Soc.* **1930,** *52*, 1751-1772.

(39) The volume of the larger droplets was calculated assuming that they were cylindrical disks of channel height. The smaller droplets were observed to be spherical. Area measurements of combining drops confirmed these droplet shapes, as well as the fact that droplets combine most often in pairs and, under certain conditions, in groups of three.

(40) Rayleigh, L. *Proc. R. Soc. London* **1879,** *29*, 71-97.

(41) Stone, H. A.; Bentley, B. J.; Leal, L. G. *J. Fluid Mech.* **1986,** *173*, 131-158.

(42) Sammarco, T. S.; Burns, M. A. *AIChE J.* **1999,** *45*, 350-366.

(43) While the metal oxides of hard Lewis acids (Al^{3+}, Fe^{3+}) have been shown to heterogeneously catalyze the thermal degradation of certain PFPE's after an hour-long induction period, Fomblin Y is stable under such conditions. Furthermore, it is unlikely that the Cd-oleate complexes or nanocrystals in solution would catalyze the PFPE degradation due to the (1) soft Lewis acidity of

Cd^{2+}, (2) the low Cd surface concentration at the ODE/PFPE interface, and (3) the short (<40 s) PFPE residence times. See Ref. 44 for details.

(44) Kasai, P. H.; Tang, W. T.; Wheeler, P. *Appl. Surf. Sci.* **1991,** *51*, 201-211.

Chapter 8 Millisecond Kinetics of Nanocrystal Cation Exchange Using Microfluidic X-Ray Absorption Spectroscopy

8.1 INTRODUCTION

Microfluidic devices are invaluable for measuring the time-dependent behavior of rapid reactions due to their precise control, rapid mixing, and ability to transpose the reaction time onto spatial coordinates.[1] For fast reactions involving multiple reagents, rapid mixing is essential for distinguishing diffusion effects from reaction kinetics. Due to small diffusion lengths, millisecond mixing is possible in microfluidic devices and has been demonstrated in T-junctions,[2] hydrodynamically-focused jet mixers,[3] and in flowing plugs.[4] Since reaction time is proportional to the distance traveled, microfluidic reactors allow the time resolution to be decoupled from the acquisition time, which is significant for the detection of rare phenomena such as X-ray scattering or absorption.

Using a flow-focusing micromixer, Knight *et al.* monitored the fast kinetics of protein folding with small-angle X-ray scattering (SAXS),[5] demonstrating the utility of *in situ* X-ray characterization in microfluidic devices.[6-8] Similar microfluidic X-ray techniques should be useful for monitoring rapid nanoparticle reactions, such as the microfluidic synthesis of semiconductor quantum dots that we have previously demonstrated.[9,10] To demonstrate the potential of microfluidic X-ray techniques for monitoring structural evolution in rapid nanoscale reactions, we describe the use of flow-focusing microreactors and X-ray

absorption spectroscopy to probe the cation exchange of semiconductor nanocrystals on the millisecond time scale.

Recently, Son *et al.*[11] reported a reaction in which silver(I) ions added to a solution of cadmium selenide nanocrystals in toluene replace the cadmium ions in the selenium lattice, resulting in silver(I) selenide nanocrystals in the following reaction:

$$(CdSe)_n\ (\textit{nanocrystal}) + 2n\ Ag^+ \rightarrow (Ag_2Se)_n\ (\textit{nanocrystal}) + n\ Cd^{2+}$$

Despite this complete cation exchange and the rearrangement of the crystal lattice, this reaction has been observed to conserve the shape and approximate number of atoms in each nanoparticle. More significantly, this wholesale transformation, which proceeds extremely slowly (>1 hr) in bulk crystals,[12] proceeds extremely rapidly (<<1 s) at room temperature in the nanoscale regime.[11]

Explaining these fast kinetics requires knowledge of the internal composition of the nanocrystals as they react. While optical absorption could be used to obtain the general kinetics of this reaction, X-ray techniques such as Wide-Angle X-Ray Scattering (WAXS) and X-ray Absorption Spectroscopy (XAS) offer direct insight into the bond and crystal structure inside reacting nanoparticles. In particular, XAS techniques such as Extended X-ray Absorption Fine Structure (EXAFS) are useful for studying the cation exchange reaction because they can reveal information about an absorbing atom's coordinating environment, including bond lengths and local order, even in the absence of a crystalline lattice.[13]

Unfortunately, even with the high flux of synchrotron radiation, traditional XAS techniques are limited to acquisition times of ~1 to 1000 s per spectrum.[13] A handful of

energy-dispersive EXAFS (ED-EXAFS) apparatuses with stopped-flow instrumentation have demonstrated resolutions as low as 5 ms,[14] but only at large concentrations (>0.1 M) and sample volumes, which are undesirable for many nanoscale chemical and biological reactions. Thus, the typical mM concentrations and millisecond reaction times of the CdSe/Ag_2Se cation exchange reaction have discouraged *in situ* structural measurements for this unique nanoscale phenomenon.

In this study, we use a microfluidic reactor to rapidly mix reagents and perform nanocrystal cation exchange in a steady-state continuous flow scheme that enables the reaction to be probed *in situ* with X-ray Absorption Spectroscopy. Cadmium selenide nanocrystals are mixed with silver(I) ions using a hydrodynamic focusing scheme based on that of Knight *et al.*[3] The smaller silver(I) ions rapidly diffuse from the outer edges of a microchannel into a central nanocrystal stream to initiate the reaction, while the larger nanocrystals remain in the center of the microchannel due to laminar flow. The reaction is probed through a thin, X-ray-transparent silicon nitride window over the reaction channel using micro-XAS (μXAS) acquired at the Se K-edge (12.66 KeV). By acquiring spectra at different points along the channel, we are able to observe the cation exchange kinetics *in situ* down to 4 ms resolution. At 1.4 mM CdSe molecular concentration, the reaction was observed to occur on the time scale of 100 ms, and we did not detect the presence of any intermediates that had significantly different spectra than the CdSe reactant or Ag_2Se product. Although signal limitations in this particular study prevented the collection of more revealing EXAFS spectra, this study illustrates the feasibility of *in situ* microfluidic X-ray synchrotron techniques for studying the millisecond structural transformations of nanoscale materials.

8.2 EXPERIMENTAL

8.2.1 Device Design & Usage

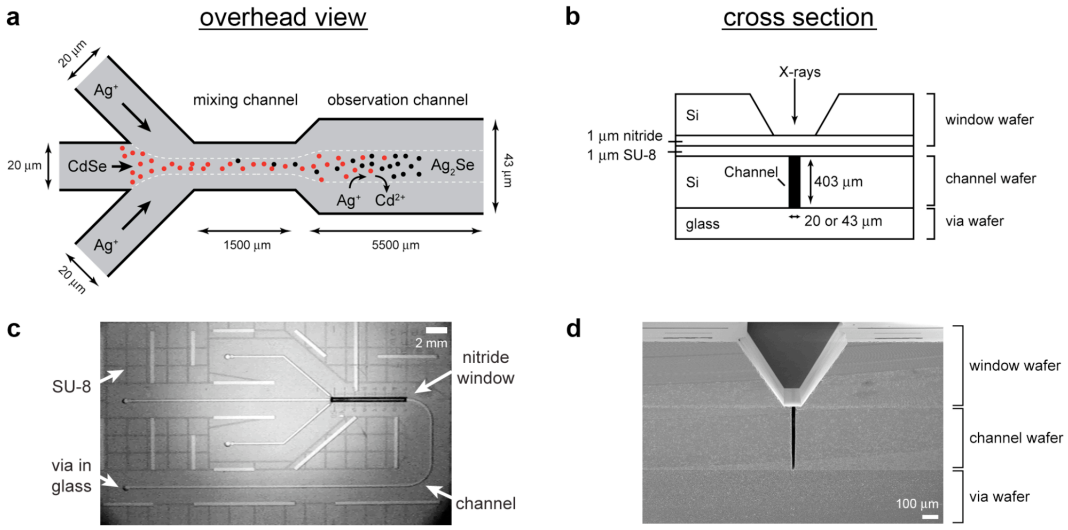

Figure 8.1. (a) Channel schematic of the XAS microreactor chip. Ag^+ ions diffuse into the focused stream of CdSe nanocrystals and react to form Ag_2Se nanocrystals. Chip cross section (b) and overhead infrared image (c) showing the nitride membrane on the top window wafer, the SU-8 adhesion layer, the middle channel layer, and the bottom glass via layer. (d) SEM cross-section of the mixing channel.

A schematic of the 110 nL, silicon-based microreactor is shown in Figure 8.1a. CdSe nanocrystal solution is injected via syringe pump into the center inlet, while Ag^+ solution is injected into the two side inlets. After the three, 20 µm-wide inlet channels intersect, the nanocrystal stream is hydrodynamically focused as it enters the 20 µm-wide, 1.5 mm-long "mixing channel," where the Ag^+ ions diffuse rapidly into the ~7 µm-wide CdSe stream. After mixing, the channel widens into a 43 µm-wide by 403-µm deep by 5.5 mm-long "observation channel" so that the 14 µm-wide center nanocrystal stream can be more readily

probed with a 16 × 7 μm (horizontal × vertical) X-ray spot through the 100 μm-wide nitride window aligned over the channel.

With typical flow rates of 12 μl/min at each inlet (36 μl/min total), the velocity in the center of the observation channel is $1.5v_{avg}$ = 52 μm/ms, where v_{avg} is the average linear velocity.[15]

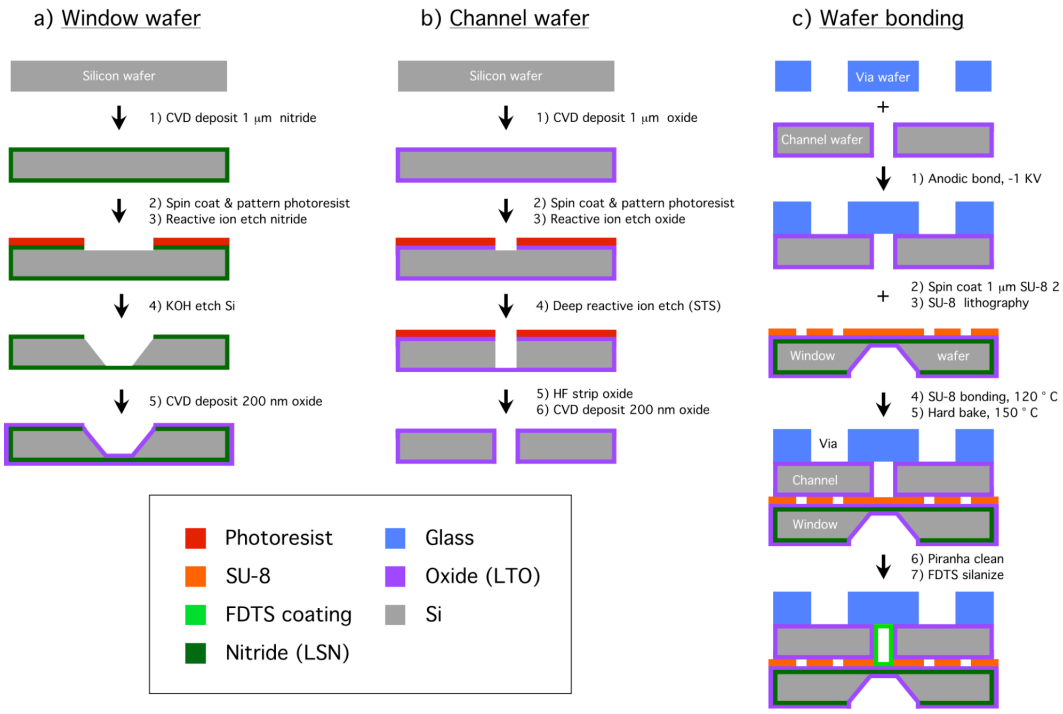

Figure 8.2. Chip fabrication process flow for (a) the window wafer, (b) channel wafer, and (c) wafer bonding.

8.2.2 Fabrication

The microfluidic XAS device, whose cross-section is shown in Figure 8.1b, is fabricated as three separate layers: (1) a top, silicon "window" wafer, (2) a middle, silicon "channel" wafer, and (3) a bottom, glass "via" wafer. The fabrication process (Figure 8.2) is detailed below.

The window wafer is fabricated with 1 μm-thick silicon nitride windows that allow the sample to be probed with μXAS with negligible window absorption (Figure 8.2a). Silicon (100) (430-μm thick, 100-mm diameter) wafers are coated with 1 μm-thick low-stress (silicon-rich) silicon nitride via chemical vapor deposition (CVD). Reactive ion etching (RIE) is used to remove the nitride corresponding to the window mask pattern, which is aligned to the wafer's (110) planes. The exposed silicon is anisotropically etched with KOH through to the nitride on the back of the wafer. These resulting nitride membranes are protected with 200 nm of low-temperature CVD oxide (LTO) on each side.

The channel wafer contains etched channels for flowing the reaction solutions. Flow channels (43-μm wide) are lithographically etched completely through 403 μm-thick, double side-polished (DSP) silicon wafers using deep reactive ion etching (DRIE) and then passivated with 200 nm of CVD oxide (Figure 8.2b). These channels are designed to be very narrow to facilitate rapid diffusion and to be very tall to maximize X-ray absorption. In addition, for fluid flowing in the lateral center of the channel, the high aspect ratio (>9:1 height:width) results in a flat fluid velocity profile over 75% of the channel's vertical axis, reducing the residence time distribution and improving time resolution.

The via wafer, made from 575 μm-thick borofloat glass, contains drilled holes for fluidic access to the channel layer. Glass is used opposite the nitride window in order to prevent diffraction of the incident X-rays.

8.2.3 Bonding

The fluidic channels are enclosed by sealing the channel wafer between the window wafer and via wafer (Figure 8.2c). The glass via wafer is first anodically bonded to the bottom of the Si channel wafer. The nitride window wafer is then bonded to the top of the channel wafer using 1 μm-thick SU-8 photoresist. The epoxy resin-based SU-8 (Microchem) is chemically and mechanically robust when cured. Other bonding methods are avoided due to fragile nature of the nitride membranes. To perform the SU-8 bonding, standard procedures (1 min bake cycles, 93 mJ/cm^2 I-line dose, 30 s development) are used to lithographically pattern SU-8 2 on the membrane side of the window wafer. After rinsing with isopropyl alcohol and gentle drying, the SU-8 is baked on a 70 °C hot plate for 1 min and then at 90 °C for 5 min in order to remove volatile solvents. Using a Karl Suss BA6 wafer aligner, the window wafer is then aligned to the channel-via wafer assembly. Finally, the aligned wafers are bonded by pressing the SU-8 layer onto the exposed surface of the channel wafer. The bond is facilitated by placing the three-wafer stack on a 120 °C hot plate and rolling a cylindrical metal weight over the stack with manual pressure for ~5 min. This rolling action, in addition to the channels in the SU-8, helps to eliminate voids in the softened photoresist. The SU-8 is hard baked in an 150 °C oven for 1 hr, after which the bonding is robust enough to survive dicing of the devices. Infrared images (Figure 8.1c) of

the final devices show the SU-8 bonding to be relatively void-free, and scanning electron micrographs of chip cross-sections (Figure 8.1d) clearly depict the tight seal generated by the bonding between the three layers.

8.2.4 Passivation

In order to prevent nanoparticle deposition on channel walls during the reaction, the oxide-coated walls are silanized with 1H,1H,2H,2H-perfluorodecyltrichlorosilane (FDTS) from solution.[10] A room-temperature piranha-cleaning step prior to silanization strips the SU-8 in the channel but not the SU-8 sandwiched between the wafers, demonstrating the chemical resistance of the bond. The robust FDTS/oxide passivation, coupled with the use of dodecylamine surfactant, prevented nanoparticle deposition and enabled individual devices to be run nearly continuously for >44 hours.

8.2.5 Reagents/Solutions

All CdSe and Ag^+ solutions are prepared with a 5% wt/wt (232 mM) solution of dodecylamine (DDA) in toluene in order to solubilize the Ag_2Se nanocrystals. Immediately prior to their use, solutions are filtered with 0.45 μm PTFE syringe filters and sparged with helium to prevent bubble formation in the channel.

CdSe nanocrystal solutions are prepared by dissolving tri-*n*-octylphosphine oxide-capped CdSe nanocrystals (diameter = 3.6 ± 0.4 nm) in the DDA solution at a typical Cd^{2+} concentration of 1.4 mM.[16] The $[Cd^{2+}]$ of the stock CdSe solution is verified by inductively

coupled plasma optical emission spectroscopy (ICP-OES). "CdSe" concentrations always refer to the concentration of individual Cd^{2+} or Se^{2-} ions, and unless specified, reagent concentrations will refer to the values before mixing.

Ag^{+} solutions are prepared by dissolving anhydrous $AgClO_4$ in DDA stock solution for a typical Ag^{+} concentration of 5 mM. [*Safety note*: *silver perchlorate is a potentially explosive compound, especially when dissolved in organic solvents and subsequently dried. The solutions used in this experiment were always dilute and used in small volumes. Silver perchlorate can be replaced by silver(I) triflate, although the kinetics of cation exchange may be different.*]

8.2.6 X-ray absorption spectroscopy

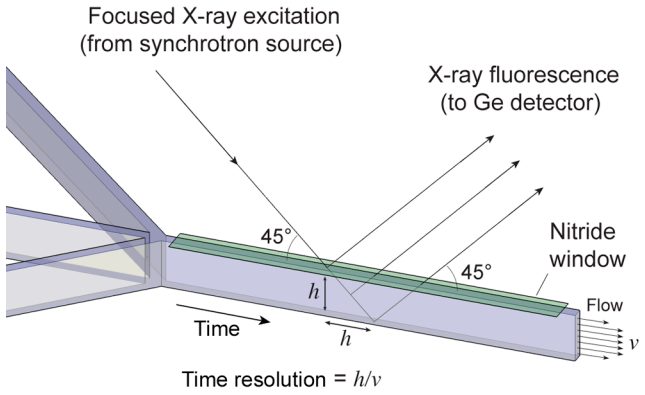

Figure 8.3. X-ray beam paths through the microreactor channel. Monochromated X-rays are focused through the window wafer's nitride membrane and into the observation channel of the channel wafer at a 45° angle to the direction of flow. X-ray fluorescence is monitored at a 90° angle to the incident radiation. Due to the 45° angle of incidence, a channel with height h and linear particle velocity v has a time resolution of h/v.

X-ray synchrotron experiments were performed at Beamline 10.3.2 at the Advanced Light Source (ALS).[17] The microreactor chip is mounted in a custom-machined aluminum manifold on an x-y translation stage that allows time-resolved spectra to be recorded at various points along the channel. Elemental mapping of the X-ray fluorescence is used to determine the location of probe with respect to the reagent streams. As shown in Figure 8.3, a monochromated 16 × 7 μm (horizontal × vertical) X-ray spot is focused through the nitride membrane onto the center of the CdSe stream at a 45° angle to the direction of fluid flow. X-ray fluorescence at the Se K-edge is measured with a 7-element germanium detector at a 90° angle with respect to the incident beam. Fluorescence is measured rather than transmission because the emission intensity has better signal-to-noise ratio and should be linear with absorption at the short path lengths and dilute concentrations used in this experiment. XAS spectra are collected by scanning the incident energy from 12.50 to 12.86 KeV and recording the Se K-edge fluorescence integrated between 10.93 and 11.33 KeV. Spectra of CdSe and Ag_2Se standard solutions were recorded in 1.5 mm-diameter borosilicate glass capillaries with 10 um-thick walls.

Data points at each energy of a spectrum are normalized to the incident flux, and all spectra are background subtracted and normalized according to their average post-edge intensities. Four normalized sample spectra are averaged for each kinetic time point. The relative fractions of reactants and products for each time point are determined by fitting the averaged spectrum as a linear combination of the CdSe and Ag_2Se standard spectra using least-squares regression routines in Igor Pro software.

The reaction time corresponding to each spectrum is $t_{rxn} = t_{mix} + \Delta y_{obs}/v_{center}$, where t_{mix} is the residence time for fluid flowing in the center of the mixing channel, Δy_{obs} is the distance of the X-ray spot from start of the observation channel, and v_{center} is the linear flow velocity in

the center of the observation channel. Because the incident X-ray radiation passes through the channel at a 45° angle with respect to the flow axis, the length of channel excited by the incident beam is equal to *h*, the channel height (Figure 8.3). The time resolution is therefore h/v_{center}, or ~8 ms at v_{center} = 52 μm/ms (36 μL/min). We can also record spectra at v_{center} = 104 μm/ms, which improves the resolution to <4 ms, but high flow rates prevent the acquisition of longer residence times due to the finite length of the 5.5 mm-long observation channel.

8.2.7 Stopped-flow absorption experiments

Time-resolved optical absorption measurements are recorded in an Applied Photophysics stopped flow apparatus. CdSe and $AgClO_4$ solutions are injected in a 1:1 volumetric ratio through a 10 mm-path length cell. Absorption is measured at 600 nm (A_{600}), which is slightly below the absorption edge of 3.6 nm CdSe nanocrystals but above that of the low-band gap Ag_2Se. The percent conversion is defined as $Abs_{600}(t)/Abs_{600}(t\rightarrow\infty)$.

8.3 RESULTS & DISCUSSION

Using our flow-focusing microfluidic device, we obtained time-resolved μXAS spectra of CdSe nanocrystals as their Cd^{2+} cations were exchanged with Ag^+ ions to form Ag_2Se nanocrystals. Figure 8.4 shows a spectral time series of such a cation exchange reaction performed in our microreactor using initial solutions of 1.4 mM CdSe and 5 mM $AgClO_4$ in 5% wt/wt dodecylamine (DDA) in toluene. As the reaction proceeds over time, the Se K-edge spectra change from resembling the CdSe nanocrystal reference spectrum at short reaction times (16 ms) to resembling the Ag_2Se nanocrystal reference at long reaction

times (104 ms). Although CdSe and Ag_2Se have starkly different chemical and crystal structures, the two reference standards have remarkably similar XAS spectra. The major difference is the extra peak at 12.673 KeV in the CdSe spectrum. As shown in Figure 8.4, this CdSe peak clearly disappears over the course of 100 ms.

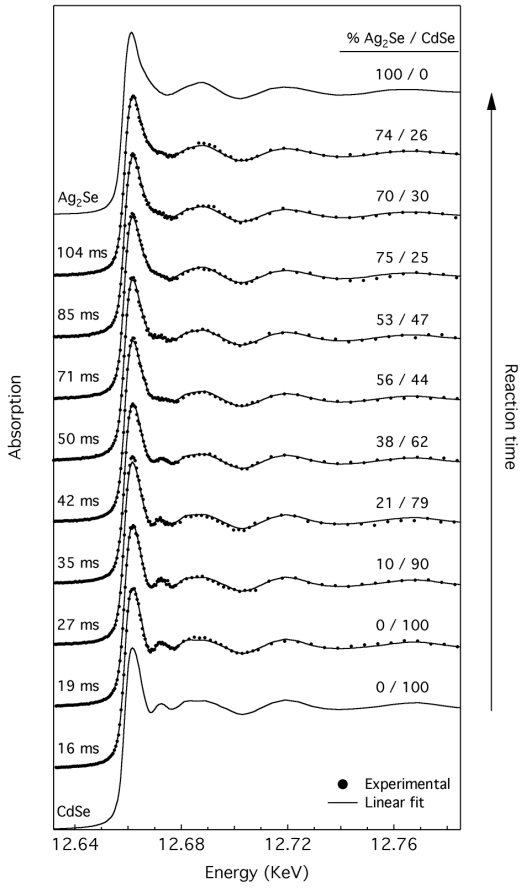

Figure 8.4. Time-resolved Se K-edge XAS spectra acquired *in situ* during the CdSe→Ag_2Se nanocrystal cation exchange reaction using 1.4 mM CdSe and 5 mM $AgClO_4$ solutions. Each reaction time corresponds to a different position along the reactor channel. Ag_2Se and CdSe compositions were extracted from fits performed using linear combinations of the Ag_2Se and CdSe reference spectra (top and bottom).

To quantify the progress of the cation exchange reaction over time, we fit each spectrum as a linear combination of the normalized CdSe and Ag_2Se standards according the equation:

$$\mu_{unknown}(E) = f_{CdSe} \cdot \mu_{CdSe}(E) + f_{Ag_2Se} \cdot \mu_{Ag_2Se}(E)$$

where $\mu(E)$ is the X-ray absorption of Se atoms in the given species as a function of the energy E, and f is the fraction of Se atoms in the form of CdSe or Ag_2Se, where $f_{CdSe} + f_{Ag_2Se} = 1$. As shown in Figure 8.4, the linear fits match the aforementioned μXAS spectra within the noise of the spectra and with no systematic residual. The excellent fits suggest that, within the temporal resolution (~8 ms) and precision ($f_{Ag_2Se} \sim \pm 5\%$) of our procedure, there is no evidence for any significant population of intermediates that have appreciably different spectra from the standards. Principal Component Analysis (PCA)[18] confirms that the set of spectra in Figure 8.4 can be described sufficiently as the weighted sums of just two independent components, whose contributions are strongly correlated to those of the Ag_2Se and CdSe reference spectra. A third primary component considered for completeness did not substantially improve the linear fits, and its fractional contribution over time did not exhibit any coherent trend.

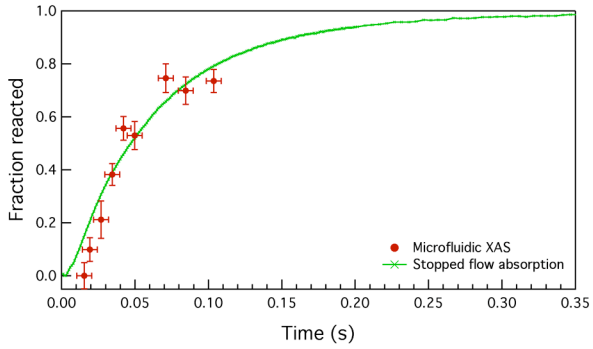

Figure 8.5. Fractional conversion vs. time using fit parameters extracted from XAS fits (1.4 mM CdSe, 5 mM $AgClO_4$, red dots) and stopped flow experiments (1.4 mM CdSe, 6.67 mM $AgClO_4$ at 1:1 volumetric ratio, green line). Error bars show 95% confidence limits.

Since f_{Ag_2Se} describes the progress of the cation exchange reaction, we can generate kinetic curves by plotting f_{Ag_2Se} vs. time. Figure 8.5 presents the kinetic curve for the fit parameters extracted from the spectra in Figure 8.4 (1.4 mM CdSe/5 mM $AgClO_4$). No reaction was observed prior to 14 ms, the residence time of the nanocrystals in the 20 μm-wide mixing channel. f_{Ag_2Se} rises smoothly and approximately linearly from 16 to 50 ms, after which the curve gradually flattens as reagents are depleted. At the flow rate of 36 μl/min (52 μm/ms), the longest residence time that could be measured in the 5.5 mm-long observation channel was 104 ms. The spectrum at 104 ms appears very similar to that of fully reacted Ag_2Se nanocrystals, but the linear fits indicate that the nanocrystals were only 74% Ag_2Se. Although the flattening of the μXAS kinetic curve might suggest that the reaction was near equilibrium at f_{Ag_2Se} = 74%, powder X-ray diffraction patterns (Figure 8.6) of Ag_2Se nanocrystals collected from the chip minutes after mixing exhibit none of the original wurtzite CdSe peaks and exhibit only peaks assigned to fully-exchanged tetragonal Ag_2Se nanocrystals by Son *et al.*[11]

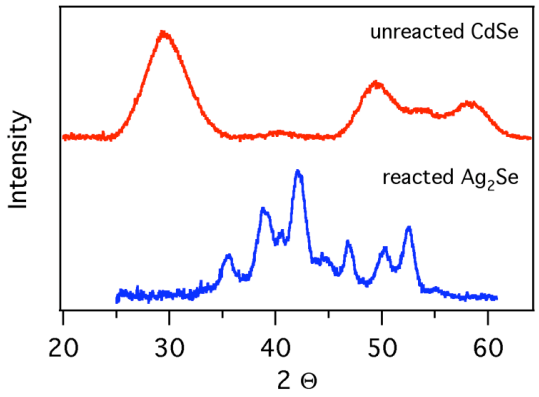

Figure 8.6. Powder X-ray (Co Kα) diffraction patterns of unreacted and chip-reacted nanocrystals. The original CdSe nanocrystals (top) exhibit characteristic wurtzite CdSe peaks, while the product nanocrystals (bottom), reacted in the chip using 2.8 mM CdSe and 5 mM $AgClO_4$, exhibit only the peaks of tetragonal Ag_2Se.

The stopped flow kinetic curve in Figure 8.5 suggests that cation exchange does in fact continue to completion past 100 ms. The stopped flow trace overlaps with the microfluidic XAS data between 35 and 104 ms, which indicates that there is qualitative agreement between the two techniques during the period over which most of the structural transformation takes place. We can then extrapolate that, since the stopped flow curve asymptotically approaches 100% Ag_2Se at long reaction times, the microfluidic XAS kinetic curve would similarly observe f_{Ag_2Se} >74% at t > 104 ms.

The discrepancy between the microfluidic and stopped flow curves at short reaction times may be due to differences in the mixing behavior of the two techniques. Due to intrinsic differences in their volumetric mixing ratios, the stopped flow and microfluidic methods must use different initial reagent concentrations to achieve equivalent "average" concentrations over time and space. The brief, turbulent mixing of the stopped flow cell compared to the continuous diffusive mixing of the laminar flow microreactor, however, still results in discrepancies in the reagent concentrations over time. At early times, the stopped

flow solutions are turbulently mixed after a dead time of several ms, while the diffusive mixing of the flow-focusing micromixer is several times slower because the Ag^+ ions must diffuse into center CdSe stream while simultaneously being consumed by the reaction.

At short distances from the mixing point in the microreactor, the Ag^+ ions may not have enough time to diffuse to the center of the CdSe stream, which may explain why no Ag_2Se is observed in the μXAS curve at times < 19 ms in Figure 8.5. ESI CFD-ACE+ finite element simulations, however, indicate that we should still observe 5-10% Ag_2Se at 16 ms, indicating that reaction-diffusion effects cannot completely account for the absence of Ag_2Se signal. Such low Ag_2Se fractions, however, are poorly resolved due to the sensitivity limits of our setup. Due to the small sample size, the noise of the XAS spectra is 0.5% root mean square (rms), while the difference between the remarkably similar Ag_2Se and CdSe Se K-edge XAS spectra is only ~5% rms. Therefore, the real resolution is effectively f_{Ag_2Se} = 10% when using least-squares regression, which explains our inability to detect the <10% fraction of Ag_2Se predicted by simulation. This analysis suggests that more precise data can be obtained with a higher quality signal or by using a reference system with greater contrast.

Despite these resolution issues, the similar qualitative shapes of the XAS and stopped flow kinetic curves imply that the microfluidic XAS technique has fairly accurately captured the ~100 ms ($1/e$ = 66 ms) time scale as well as the structural evolution of the nanoscale cation exchange reaction. Since the time scale of this nanocrystal cation exchange reaction has not been measured previously, it is useful to discuss its physical context. We can use Smoluchowski diffusion theory[19] for bimolecular reactions to estimate[20] that, at 3.33 mM Ag^+, ~4×10^7 Ag^+ ions will collide with one 3.6-nm nanocrystal each second. Assuming the reaction to be "complete" after 200 ms (f_{Ag_2Se} = 0.95), it takes ~10^7 collisions to react an entire nanocrystal, or ~10^4 collisions to exchange one of the ~460 Cd^{2+} cations inside a 3.6

nm nanocrystal. This implies that, on average, one out of every 10^4 Ag^+ collisions actually contributes to the cation exchange at room temperature. In comparison, typical reactions require 10^{10}-10^{11} collisions for a single reaction event.[21] Such cation exchange efficiency is surprisingly high, given that the underlying process is a solid state reaction that involves ions diffusing in a crystal lattice at room temperature. This efficiency may suggest that charge-charge or charge-dipole interactions increase the frequency of ion-nanocrystal collisions, and the rapid rate is almost certainly related to the above average mobility of Ag^+ in Ag_2Se, although the diffusion rate is much slower than in the superionic cubic phase of Ag_2Se.[22] The high efficiency may also be related to the high symmetry of the interacting species. Assuming that every collision with kinetic energy greater than the activation barrier reacts, the 10^{-4} collision efficiency puts a ceiling on the activation energy at ~5 kcal/mol, which is approximately the strength of a hydrogen bond. Such low activation energy and high collision efficiency values, consistent with the fast reaction time, highlight the unique nature of this nanoscale cation exchange reaction.

In order to gauge the nanoscale size effect of this reaction, we can compare our results with literature values for bulk reactions. Leung *et al.* found that exposing (001) CdSe substrates to 5 mM $AgNO_3(aq)$ for 5 min resulted in a Ag profile with 50% of the maximum $[Ag^+]$ at 28 nm below the surface. If we assume an effective diffusion constant, D_{eff}, that describes the one-dimensional diffusion[23,24] of the reaction zone into the crystal with constant surface concentration, $D_{eff,bulk} = 3 \times 10^{-14}$ cm^2/s, which is reasonable compared to other literature values of solid state ionic diffusion. Using the analogous equations for diffusion into a sphere,[25,26] we calculate that a 3.6 nm-diameter sphere would have 63% (1-1/*e*) of its final Ag_2Se occupation at 63 ms, which is comparable to the 66 ms measured by μXAS and stopped flow absorption.

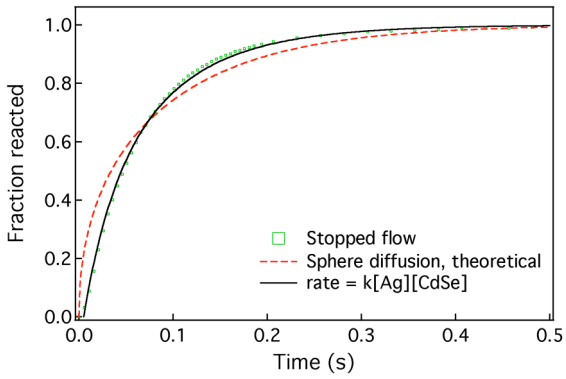

Figure 8.7. Comparison of the stopped flow kinetic curve (green squares) with theoretical diffusion (dashed red line) and 2nd order kinetics curves (solid black line). Stopped flow was performed with 1.4 mM CdSe, 6.66 mM $AgClO_4$. The diffusion curve was calculated for a 3.6 nm-diameter sphere with Ag^+ diffusion constant of $3x10^{14}$ cm^2/s. The 2nd order kinetics curve using the rate equation shown above was fit to the stopped flow data, with a start time of 5 ms and k = 6 x 10^3 M^{-1} s^{-1}.

The shape of the theoretical diffusion curve in Figure 8.7, however, does not resemble that of the kinetic traces, indicating that nanoscale cation exchange reaction is less diffusion-controlled than its bulk analog. The reaction kinetics inside the nanocrystal are more rate-determining than the diffusion because the diffusion rate is rapid in small volumes with high surface area. In fact, the stopped flow trace shown in Figure 8.5 can be fit to the relevant integrated rate equation[27] for the overall second-order rate equation, $d[Ag_2Se]/dt = k[Ag^+][CdSe]$, where the rate constant k = 6 x 10^3 M^{-1} s^{-1} and the concentrations are the overall molecular concentrations. While the assumption of 2nd order kinetics is supported by the pseudo-1st order kinetics observed at large excesses of each reagent, some stopped flow traces with different conditions do not fit well to these simple 2nd order kinetics, indicating that the reaction kinetics are convoluted sometimes by transport effects. The sensitivity of the kinetics to reagent concentrations, surfactant weight percentage, and nanoparticle size, suggests that the diffusion-determined width of the reaction zone is comparable to the 1.8 nm radius of the particles. Evidence for a similar reaction zone width was observed by Son *et*

al. We are currently simulating the internal reaction and transport with finite element methods to generate a more general and quantitative model of the cation exchange reaction.

If the kinetics of nanocrystal cation exchange could be explained by diffusion and kinetic behavior that adhere to bulk scaling laws, then there would be no evidence for an anomalous nanoscale size effect. The ~100 ms time scale measured for nanocrystal cation exchange, however, is much slower than expected. The reaction time for the original cation exchange experiments with CdSe nanocrystals had been estimated to be ~1 ms,[28,29] which is two orders of magnitude faster than our observation. The protocol detailed by Son *et al.*,[11] however, used silver(I) nitrate solvated with methanol, while this experiment avoided the use of methanol to prevent precipitation of Ag_2Se nanocrystals. In fact, Son *et al.* hypothesized that the four-fold more exothermic enthalpy of solvation of Cd^{2+} by methanol with respect to Ag^+ was the driving force behind the rapid kinetics.[11,30] To test whether the lack of methanol was the reason for the slow cation exchange kinetics observed, we added methanol in 5 and 10% vol/vol amounts to the $AgClO_4$/dodecylamine/toluene solutions. As shown in Figure 8.8, the addition of methanol appears to increase the kinetics slightly, but not enough to change the ~100 ms time scale of the reaction dramatically. Increasing the concentration of methanol does tend to increase the fractional conversion, especially when the 0% MeOH trace is observed to plateau. This suggests that solvation enthalpy, a thermodynamic property, may not adequately explain the kinetics in our particular experiment.

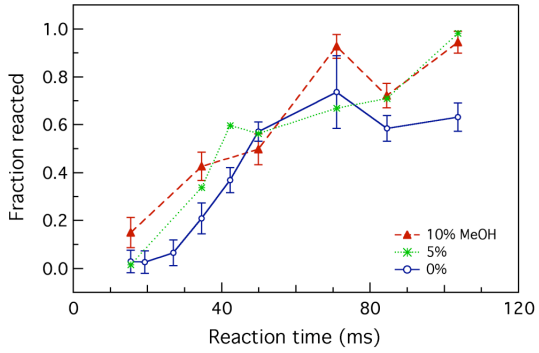

Figure 8.8. Fraction reacted vs. time with the indicated volume fractions of methanol at 2.8 mM CdSe, 5 mM $AgClO_4$.

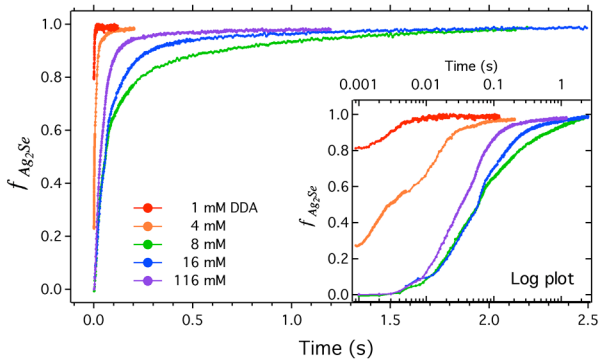

Figure 8.9. Stopped flow absorption curves at various dodecylamine (DDA) concentrations and 1.4 mM CdSe, 5 mM $AgClO_4$. Inset: log plot of the same data.

Another explanation for the slower kinetics could be that the high concentration of dodecylamine, necessary to keep the Ag_2Se nanoparticles from precipitating on the microchannel walls, slows down the reaction. Stopped flow experiments with 1.4 mM CdSe and 5 mM $AgClO_4$ at different concentrations of dodecylamine (Figure 8.9) definitively show that at very low (1 mM) DDA concentrations, the reaction is 90% complete at 3 ms, although the full curve was too fast to be resolved by stopped flow. Increasing the [DDA] to 8 mM slows down the 90% conversion point to 660 ms, at which point further addition of DDA actually decreases 90% conversion time to ~120 ms. The fact that the kinetic effect of DDA reverses suddenly around DDA:Ag^+ = 4 (10 mM [DDA], 2.5 mM $[Ag^+]_{final}$) suggests that the dodecylamine hinders cation exchange primarily by forming tetrahedral complexes with Ag^+. At [DDA] > 10 mM, all Ag^+ species are fully coordinated. Increasing the [DDA] further increases the population of free DDA, which can stabilize the Cd^{2+} product and increases the polarity of the solvent, which may increase the reaction rate by stabilizing a polar or charged transition state. The fact that the nanoscale cation exchange reaction is accelerated at lower amine concentrations could suggest that the water in the experiment of Leung *et al.* is playing a similar role as DDA, or it could suggest that there may still be a size-dependent kinetic effect for cation exchange.

Clearly, more experiments need to be performed before the actual mechanism behind the nanoscale cation exchange reaction is elucidated. Stopped flow absorption experiments may be more practical for gathering single-wavelength kinetic data for determining rate orders and rate constants, but *in situ* μXAS is far more valuable for investigating the time-dependent nature of the nanocrystals' structural transformation. Due

to time and signal constraints, the spectra collected for this experiment were too noisy and narrow in energy range to perform rigorous EXAFS analysis. Our work does reveal means for improvement in collection efficiency, however, and at a beamline with improved flux, spectra should be clean enough to extract bond orders and geometries. The current time resolution is comparable to those of energy-dispersive EXAFS (ED-EXAFS)[13], but our technique is applicable to solutions too dilute to be detected in transmission mode, as ED-EXAFS requires. The decoupling of acquisition time and time resolution in microreactors should give future microfluidic XAS studies the advantages of traditional EXAFS at millisecond time-resolution.

8.4 CONCLUSION

We have successfully fabricated a flow-focusing microreactor to observe the ~100 ms evolution of the CdSe→Ag_2Se nanocrystal cation exchange reaction using micro X-ray absorption spectroscopy. The small dimensions of the reactor enable rapid mixing and *in situ* observation of the millisecond reaction with μXAS even with acquisition times of hundreds of seconds. XAS spectra clearly show the structural progression of CdSe nanocrystals to Ag_2Se without the presence of long-lived intermediates, and kinetic curves can be generated by fitting the spectra with linear combinations of the reactant and product data. The time scale of the reaction, confirmed with stopped flow absorption experiments, is surprisingly slower than expected, most likely due to high concentrations of amines used to solubilize the product nanocrystals. Further refinements to the microfluidic device to optimize signal and energy range should enable the acquisition of full EXAFS spectra at various edges and even the collection of wide- and small-angle X-ray scattering data. The

robust nature of this device also should allow the use of a wider range of chemicals and temperatures than polymer-based microdevices, making microfluidic XAS an indispensable tool for determining the mechanism of nanocrystal cation exchange and other structural transformations that can be induced by diffusive mixing.

8.5 REFERENCES

(1) deMello, A. J. *Nature* **2006**, *442*, 394.

(2) Kamholz, A. E.; Weigl, B. H.; Finlayson, B. A.; Yager, P. *Anal. Chem.* **1999**, *71*, 5340.

(3) Knight, J. B.; Vishwanath, A.; Brody, J. P.; Austin, R. H. *Phys. Rev. Lett.* **1998**, *80*, 3863.

(4) Song, H.; Tice, J. D.; Ismagilov, R. F. *Angew. Chem. Int. Ed.* **2003**, *42*, 768.

(5) Pollack, L.; Tate, M. W.; Finnefrock, A. C.; Kalidas, C.; Trotter, S.; Darnton, N. C.; Lurio, L.; Austin, R. H.; Batt, C. A.; Gruner, S. M.; Mochrie, S. G. J. *Phys. Rev. Lett.* **2001**, *86*, 4962.

(6) Akiyama, S.; Takahashi, S.; Kimura, T.; Ishimori, K.; Morishima, I.; Nishikawa, Y.; Fujisawa, T. *Proc. Natl. Acad. Sci. U. S. A.* **2002**, *99*, 1329.

(7) Barrett, R.; Faucon, M.; Lopez, J.; Cristobal, G.; Destremaut, F.; Dodge, A.; Guillot, P.; Laval, P.; Masselon, C.; Salmon, J. B. *Lab Chip* **2006**, *6*, 494.

(8) Greaves, E. D.; Manz, A. *Lab Chip* **2005**, *5*, 382.

(9) Chan, E. M.; Mathies, R. A.; Alivisatos, A. P. *Nano Lett.* **2003**, *3*, 199.

(10) Chan, E. M.; Alivisatos, A. P.; Mathies, R. A. *J. Am. Chem. Soc.* **2005**, *127*, 13854.

(11) Son, D. H.; Hughes, S. M.; Yin, Y. D.; Alivisatos, A. P. *Science* **2004**, *306*, 1009.

(12) Leung, L. K.; Komplin, N. J.; Ellis, A. B.; Tabatabaie, N. *J. Phys. Chem.* **1991**, *95*, 5918.

(13) Newton, M. A.; Dent, A. J.; Evans, J. *Chem. Soc. Rev.* **2002**, *31*, 83.

(14) Yoshida, N.; Matsushita, T.; Saigo, S.; Oyanagi, H.; Hashimoto, H.; Fujimoto, M. *J. Chem. Soc.-Chem. Commun.* **1990**, 354.

(15) $v_{center} = 1.5v_{avg}$ assuming two-dimensional laminar slot flow, which is valid at high channel aspect ratios.

(16) Murray, C. B.; Norris, D. J.; Bawendi, M. G. *J. Am. Chem. Soc.* **1993**, *115*, 8706.

(17) Marcus, M. A.; MacDowell, A. A.; Celestre, R.; Manceau, A.; Miller, T.; Padmore, H. A.; Sublett, R. E. *J. Synchrotron Rad.* **2004**, *11*, 239.

(18) Manceau, A.; Marcus, M. A.; Tamura, N. Quantitative speciation of heavy metals in soils and sediments by synchrotron X-ray techniques. In *Applications of Synchrotron Radiation in Low-Temperature Geochemistry and Environmental Sciences*, 2002; Vol. 49; pp 341.

(19) North, A. M. *The Collision Theory of Chemical Reactions in Liquids*; Wiley: New York, 1964; Vol. vii.

(20) Collision frequency $z = 4\pi(R_{Ag+} + R_{CdSe})(D_{Ag+} + D_{CdSe})[Ag^+]$, where R is the radius and D is the Stokes-Einstein diffusion constant. Both species were assumed to be coordinated with dodecylamine. For a 3.6 nm-diameter nanocrystal with DDA, R_{CdSe} was calculated to be 3.4 nm. R_{Ag+} was estimated to be a maximum of 1.7 nm.

(21) Katakis, D.; Gordon, G. *Mechanisms of Inorganic Reactions*; Wiley: New York, 1987.

(22) Sitte, W. *Solid State Ionics* **1997**, *94*, 85.

(23) For the 1D diffusion of a species with diffusion constant D and constant surface concentration c_s, the concentration c at a depth x at time t is:

$$c = c_s \cdot erfc\left(x/2\sqrt{Dt}\right).$$

(24) Welty, J. R.; Wicks, C. E.; Wilson, R. E. *Fundamentals of Momentum, Heat, and Mass Transfer*, 3rd ed.; Wiley: New York, 1984.

(25) For the average concentration c_{avg} inside a sphere with constant surface concentration c_∞, $c_{avg}/c_\infty = \left(6/\sqrt{\pi}\right)\sqrt{\lambda t} - 3(\lambda t) + 12\sqrt{\lambda t}\sum_{n=1}^{\infty} ierfc\left(n/\sqrt{\lambda t}\right)$, where $\lambda = D/a^2$, D is the diffusion constant in the sphere, a is the sphere radius, and $ierfc(x) = \pi^{-1/2}e^{-x^2} - x \cdot erfc(x)$, according to Ref. 26.

(26) Carslaw, H. S.; Jaeger, J. C. *Conduction of Heat in Solids*, 2nd ed.; Oxford University Press: London, 1959.

(27) The overall 2nd order differential rate equation with 2:1 Ag^+:CdSe stoichiometry can be integrated to derive the expression: $f_{Ag_2Se} = \left(1 - (M-1)/\left(M \cdot \exp\left[2(M-1)[CdSe]_o kt\right] - 1\right)\right)$, where $[CdSe]_o$ is the initial CdSe concentration, $M = [Ag^+]_o/[CdSe]_o$, and k is the 2nd order rate constant.

(28) The reaction time estimate was extracted from the size distribution of the reacted nanocrystals via Smoluchowski coagulation theory. Our estimated 1 ms reaction time agrees with similar estimates by Son *et al.*

(29) Smoluchowski, M. *Z. Phys. Chem.* **1917**, *92*, 129.

(30) Burgess, J. *Metal Ions in Solution*; Wiley: New York, 1978.

Chapter 9 Summary & Outlook

9.1 SUMMARY OF RESEARCH

I have designed and demonstrated the use of microfluidic reactors for controlling nanocrystal reaction parameters and reproducibly synthesizing semiconductor nanocrystals at high temperature. Using continuous flow microreactors, the size of CdSe nanocrystals was controlled by tuning the temperature, flow rate, concentration, and precursor ratio. Microfluidic reactors were also used to synthesize nanocrystals of various materials, including CdSe, CdTe, and cobalt sulfide in the shape of rods, tetrapods, and hollow spheres. I developed microfluidic devices that generated droplets at high capillary number, low viscosity ratios, and high temperature, and such droplets were used in liquid-liquid segmented flow reactors to reduce particle deposition and residence times during the synthesis of CdSe spheres. In addition to synthesizing nanocrystals, microfluidic devices were used to perform cation exchange reactions on existing CdSe nanocrystals and measure the millisecond kinetics using X-ray absorption spectroscopy. These results demonstrate the utility of both performing and characterizing rapid nanoscale reactions in microfluidic reactors. Furthermore, the control and characterization of inorganic materials under harsh conditions demonstrates that glass and silicon microfluidic reactors can be applied to other reactions that involve flowing particles, high temperatures, aggressive reagents, or air-sensitive precursors.

9.2 PERSPECTIVE

To put these accomplishments in perspective, one must consider that there were no published reports on the synthesis or reaction of nanoparticles in microfluidic reactors when this dissertation research began in late 2000. In the following six years, a handful of groups around the world have developed such nanoparticle microfluidics into a small but growing niche that has piqued wide interest in both the materials and microfluidics communities. To date, over two dozen publications report the use of silicon, glass, and polymer microchips as well as glass and metal microcapillaries for the microfluidic synthesis of nanoparticles made from metals such as gold,[1,2] silver,[2,3] cobalt,[4] palladium,[5] and copper;[6] oxides such as ZnO,[7] TiO_2,[8-10] and SiO_2[11]; and semiconductors such as CdS[12-14] and CdSe,[15-21] including CdS/CdSe[13] and CdSe/ZnS[22,23] core/shell heterostructures.

A temporary dip in publications in 2005 reflects the realization that the advantages of continuous flow reactors were being muted by the ubiquitous problems of particle deposition and residence time distribution. Several groups, including this Alivisatos-Mathies collaboration, simultaneously addressed these issues through the use of liquid-liquid[13,14,20] and gas-liquid segmented flow reactors.[11,21]

Interest outside this small community has been demonstrated by the numerous citations of these nanoparticle microreactor papers, as well as through reviews, news articles, and highlights in publications such as *Nature*,[24,25] *Analytical Chemistry*,[26] and *Lab on a Chip*.[27,28] In addition to synthesis, the general application, manipulation, or integration of nanoparticles in microfluidics has also received widespread interest, with over 100 publications on this topic since 2001.

9.3 REALIZING THE UNFULFILLED POTENTIAL OF NANOPARTICLE MICROREACTORS

Despite the great strides in this research in the past six years, the promise of nanoparticle microreactors has yet to be fulfilled. Nanoparticle reactors still have not demonstrated a "killer application" – such as DNA sequencing in bioanalytical devices – that compellingly justifies their use over reactions in bulk solutions. Although microfluidic devices offer many general advantages over macroscale reactions, few microfluidic experiments have utilized these advantages to significantly improve existing nanocrystal syntheses, develop novel nanostructures, or provide new insight to nanoparticle reactions. The following sections discuss several of these unrealized goals, the issues that impede them, and possible solutions for the future.

9.3.1 Improving existing syntheses and developing novel structures.

Although microreactors have demonstrated greater reproducibility and control over reaction conditions, there are very few instances in which microfluidic syntheses have substantially improved size distributions, the ability to control the shape or composition, or the ability to synthesize novel materials that cannot be synthesized in flasks. Initial efforts have been, by necessity, proof of concept experiments that have reproduced model reactions previously optimized in bulk solutions. Transferring such syntheses to microreactors required substantial re-engineering of basic microfluidic technology and required the substantial modification of precursor and surfactant solutions, often degrading the quality of syntheses. Now that we have developed protocols and microreactors that can produce

nanocrystals comparable to those made in flask reactions, unique and interesting experiments are becoming possible.

For example, use of segmented flows to reduce residence time distribution should allow for the precise investigation of rapid CdTe tetrapod nucleation arm growth at reaction times < 1 s. Preliminary results for such droplet-based CdTe growth, shown in Figure 9.1, demonstrate the ability to resolve the diffraction patterns and shapes of pyramidal zinc-blende nuclei grown for a reactions time <10 s at 250 °C.

Performing and characterizing nanocrystals efficiently in droplets will require the continued development of microfluidic droplet technology to enable essential procedures such as accurately measuring droplet velocities, identifying drops by composition, splitting and fusing drops for sample manipulation, and sorting drops by size or sample. As a demonstration of such technology, I fabricated a device that can divide each droplet into small, medium, and large drops by shearing a droplet stream with a second carrier fluid stream in a pinched channel, as shown in Figure 9.2. Because centers of mass of the larger drops are excluded from the outer streamlines of the narrow channel, the drops can be sorted continuously by size by splitting the streamlines into separate channels. Such technology could be useful for controlling drop size distributions and for producing small drops that cannot be made using traditional flow-focusing methods.

While the continuous flow of laminar streams and droplets is simple and convenient, revolutionary advances in nanoparticle growth and assembly will most likely require active actuation in order to precisely shuttle and confine small volumes of fluid in a logical and scalable manner. The development of heat- and chemical-resistant valves from fluoropolymers or silicon could enable more integrated and complex processes, such as the cyclic deposition of precursors, small molecules, or other particles, on target nanostructures.

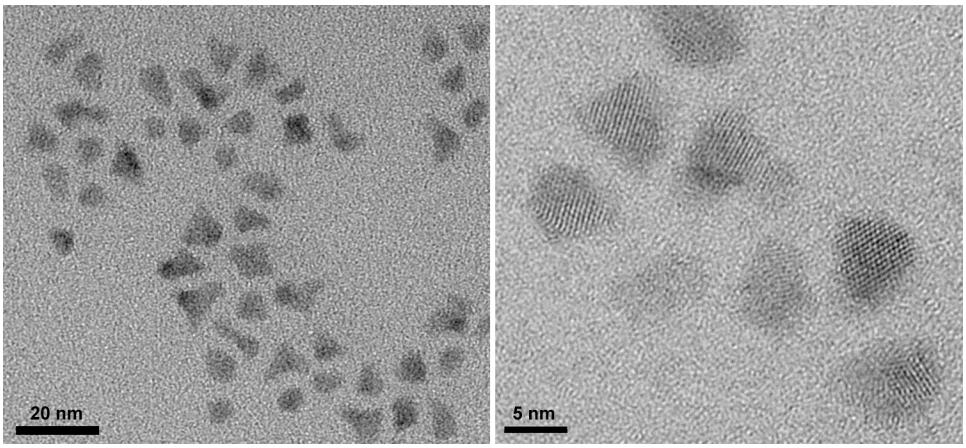

Figure 9.1. CdTe tetrapod cores synthesized in oleic acid/octadecene droplets in Fomblin Y 06/6 for <10 s at 250 °C. Images are from the same batch but at different resolutions.

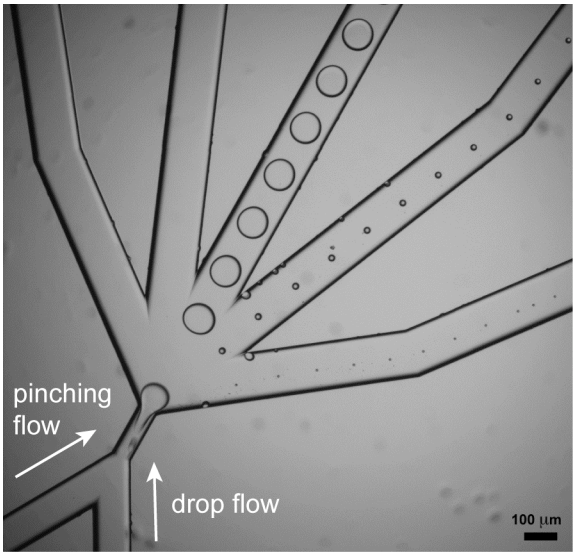

Figure 9.2. Pinched-flow fission and sorting of three sizes of octadecene droplets in Fomblin Y06/6. The pinching channel width is 75 μm.

9.3.2 Rapid screening, optimization, and characterization of nanocrystal reactions

While microreactors have demonstrated the ability to survey multiple reaction conditions and fine tune the size of particles, there are few cases in which new syntheses have been optimized or characterized more efficiently or more effectively than in flask reactions. One reason is that the screening of large areas of phase space and the identification of interesting reaction phenomena are currently limited by the narrow range of reagents that are compatible with microfluidic reactors. Microreactors are incompatible with solid surfactants, insoluble complexes, and chemicals that precipitate, outgas, or boil at high temperature. Insoluble precursors and solid surfactants, however, are mainly problems when pumping room temperature solutions from syringes. Pumping solutions from heated, on-chip reservoirs should allow the use of less soluble precursors and more traditional, high-melting surfactants, such as tri-*n*-octylphosphine oxide, that more effectively solubilize nanoparticles and precursors. Such pumping could be performed using pneumatic actuation or via robust on-chip pumps and valves.

The rapid characterization of nanocrystal products in microfluidic devices is hindered by the difficulty of probing reactions *in situ* at high temperature. While the rapid sizing of CdSe spheres can be performed via on-line fluorescence or absorption, other characterization techniques are difficult to integrate on chip, and many structural properties and materials cannot be probed optically. Typical nanocrystal characterization methods, such as transmission electron microscopy (TEM) and X-ray diffraction (XRD), often require

high vacuum, long acquisition times (~10 min), or lengthy purification steps, making the actual reaction the least rate-determining step when screening multiple reaction conditions.

Because it is unlikely that most of these materials characterization techniques can be integrated on chip, a more efficient strategy would be use more accessible methods, such as optical spectroscopy, as the first level of screening to reduce the number of targets that require off-chip characterization. While on-line fluorescence could be used, on-chip absorption and Raman spectroscopy have better signal at high temperatures, although peak-broadening is still an issue for any structural probe. Other groups[19] have cooled portions of devices in order reduce broadening and enhance fluorescence quantum yields. Although such techniques are not *in situ*, the reduced dead volumes resulting from on-chip detection make such measurement more relevant and efficient.

After spectroscopic screening, particles often need to be purified before off-chip characterization. Purifying particles is particularly difficult to integrate on-chip since the macroscopic procedure is an art form that typically involves mL sample volumes and the careful precipitation, centrifugation, and resuspension of nanocrystal pellets. Development of on-chip particle purification methods akin to the capture-based purification of biomolecules[29] would drastically reduce the sample and time required for screening synthesis conditions. Particle sorting methods, such the microfluidic Brownian ratchets developed by Huang *et al*,[30] could allow surfactants and precursors to diffuse out of focused nanoparticle streams while also separating particles by size and shape.

A diffusion-based cleaning procedure that does not dilute the particles is the two-phase counter-flow extractor, demonstrated for aqueous/organic extractions by Kitamori *et al.* [31] As shown in Figure 9.3, a nanoparticle/surfactant/octadecene solution flows in the top half of a channel, while an immiscible stream of pure methanol flows in the opposite

direction in the bottom half of a channel. Because the surfactants and precursors have much higher solubilities in methanol than the hydrophobic nanocrystals do, the surfactants and unreacted precursors partition themselves between the two phases, while the nanocrystals remain in the octadecene phase. The counter-flow setup mimics an extensive series of extractions to ensure high extraction efficiencies. Although the interface is stabilized by selective silanization on each layer, fabricating a permeable membrane in between the two layers may produce better results over large interfaces.

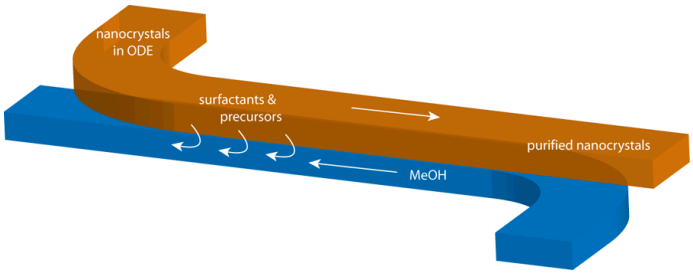

Figure 9.3. Two-phase counter-flow extractor for cleaning nanoparticles from synthesis solutions. Nanoparticles in octadecene (ODE) flow through the top channel, while pure methanol solution, which is immiscible with ODE, flows through the bottom channel in the opposite direction. Surfactants such as phosphonic acids and reagents such as Cd-oleate will partition into the MeOH stream efficiently due to the counter flow and leave the nanocrystals inside the purified ODE solution.

9.3.3 Parallel synthesis and scale-out of nanocrystal reactions

The industrial scale-out of mass-produced microreactors is also cited frequently as an advantage of microfluidic reactors, but there is not a single report in which more than one nanoparticle reactor on a chip is run simultaneously. The multiplexing of macroscopic elements such as pumps and the high maintenance of microreactor channels, such as clog

prevention, filtering, and silanization, are serious obstacles in scaling this technology out for mass production. Even temperature control is not trivial, since maintaining uniform ~300 °C temperatures across large-diameter insulating wafers is difficult without resorting to multiple, independent power supplies.

Unlike electrokinetic transport, pressure-driven flow is not easily multiplexed. While a single pressure source can be used for parallel lines, variations in pressure in one channel – due to clogging for example – affect the flow rates in other channels. Complex control schemes such as flow control transducers could be developed to maintain constant pressure in individual channels, but they also must be scalable and easily integrated into microdevices. Multi-rack syringe pumps are an option, but expensive gastight syringes also scale poorly. Microfabricated pumps that tap on-chip chemical reservoirs would be advantageous, because they would also enable the use of high-melting precursors and surfactants, but non-pulsatile on-chip pumping methods must be developed first.

9.4 THE IDEAL NANOCRYSTAL MICROREACTOR

Using the technological advances proposed in the previous section, what would the ideal nanoparticle microfluidic reactor look like? If nanoparticle microfluidics follow the current trend in bioanalytical microdevices, such microreactors will integrate as many processes on a single chip to reduce sample size, processing time, and expense while being highly scalable and sensitive.

An integrated nanoparticle reactor would likely be based on segmented flows in order to reduce particle deposition and cross contamination and to enable rapid, serial screening. Precursor, surfactant, and solvent solutions would be stored in individual

reservoirs and transported via microfabricated pumps into a droplet generation tee. Droplets could be routed selectively by valves and switches into one of many parallel reactors, in which different reaction parameters such as temperature, magnetic field, or reaction time could be varied while the particles are characterized in situ with X-ray or optical spectroscopy. For high-temperature growth, the reactor could be cooled at the ends of these channels to facilitate optical characterization, which could provide feedback to a series of switches that could tailor processing to the properties of each particle. Such processing could include further reaction cycles, the separation of the dispersed phase from the carrier phase, cleaning samples in in-line counter-flow extractors, or separation by size, shape, or quality. The output of this chip could be linked to an automated sample preparation system that could deposit samples on TEM grids or spot samples onto an X-ray diffraction plate. Such a reactor would be run in parallel an automated fashion would be straightforward to clean and maintain, possibly through the easy disassembly and assembly of modular components.

9.5 FUTURE NANOCRYSTAL RESEARCH IN MICROFLUIDIC DEVICES

Even without the ideal microreactor and even with the limitations of current devices, there are many exciting avenues left for nanoparticle microfluidics to pursue. A prudent strategy would be to focus on research in which microfluidic reactors have a competitive advantage over flask reactions. These advantages include the ability to encapsulate particles in reproducible, nL-pL droplet flows, the ability to characterize reactions with X-ray and optical spectroscopy with millisecond resolution, and the ability to rapidly alter reaction parameters.

9.5.1 Droplet-based experiments

A natural extension of my droplet research would be to synthesize various nanocrystal shapes and characterize their reaction kinetics in droplet-based reactors, which should eliminate the issue of particle deposition. Optimization of surfactant:Cd ratios should allow a larger size range of tetrapods to be synthesized. Other droplet-based studies include synthesizing nanocrystals without passivating surfactants, investigating the growth or interaction of small numbers of particles, and investigating nanorod liquid crystal phenomena in drops.

9.5.2 Microfluidic X-ray characterization of nanoparticles

Millisecond kinetic X-ray studies have proven to be useful for the spectroscopic analysis of cation exchange reactions, and technical improvements should allow future

devices to extract more enlightening information about such reactions. For X-ray fluorescence detection, the right-angle geometry chip shown in Figure 9.4 could be used to dramatically increase signal, decrease acquisition times, and increase the energy range compared to previous experiments. Collection efficiencies through the large window should be much higher than for the device described in Chapter 8, and time resolutions <1 ms can be achieved by exciting the chip at a 90° angle with respect to the flow axis, rather than the 45° angle described previously. After fabrication and preliminary testing of such devices, we found that the excitation and fluorescence windows must be much thinner to limit X-ray absorption, that extremely flat windows are necessary for beam stability, and that precise angular alignment of the excitation beam is critical.

Extended X-ray Absorption Fine Structure (EXAFS) on the silver absorption edge would give more insightful information about the time-dependent coordination of silver ions as they exchange the cations in CdSe. Although the sensitivity of our previous beamline to silver was low, the resolution of the fractional conversion of silver may be higher since changes in coordination and oxidation number are expected produce more drastic shifts in the spectra. Larger energy ranges would allow for coordination numbers and radial distributions to be calculated from the fine structure, which would suggest how the lattice evolves during the cation exchange.

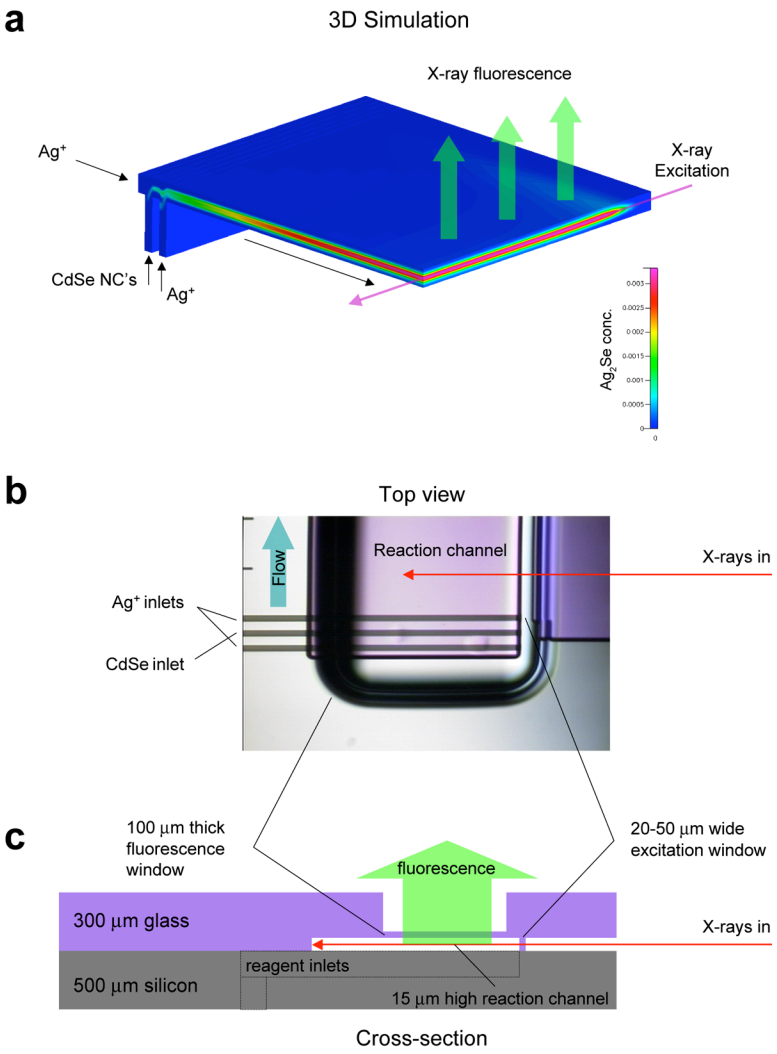

Figure 9.4. Horizontal sheath microreactor for millisecond X-ray fluorescence studies. (a) 3D simulation and schematic, showing the Ag_2Se concentration profile over the length of the reactor. Model is shown split in half for visibility. (b) Micrograph showing an overhead view of the 1 mm-wide reaction channel. Monochromated X-rays are focused through the narrow excitation window on the side, while the fluorescence is detected through the 100 μm-thick fluorescence window over the reaction channel, as shown in the cross-sectional schematic in (c).

This lattice evolution also could be detected with microfluidic X-ray scattering in double-window chips. Since such chips may be difficult to fabricate, alternatives include performing the reaction in all-polymer chips that are more X-ray transparent.[32] Rapid-mixing segmented flows could also be generated in Teflon capillary tubing, which is much easier to assemble and has higher collection efficiency that planar chip methods. Preliminary experiments showed that X-ray scattering in dilute droplet solutions is limited by the low signal at our μXAS-dedicated beamline, but more intense radiation at another beamline could alleviate this problem. X-ray absorption experiments with droplet flows also exhibited extremely noisy spectra even at high droplet frequencies, although curiously, the noise in the fluorescence signal could not be attributed entirely to low signal.

9.5.3 Environmental manipulation and stimulation of nanoscale reactions

Because microchannels have small volumes, microfluidic reactions can be uniformly manipulated via environmental stimuli such as light, electric fields, and magnetic fields. Optical experiments could include initiating rapid nanoscale reactions via laser pulses that would produce reactive precursors or burst sequestering micelles. The effect of linearly or circularly polarized on the growth of anisotropic particles in solution could be studied. Other experiments include the growth of magnetic nanoparticles and assemblies under intense magnetic fields, or activating synthesis reactions using ultrasonic vibrations and

microwave radiation. All of these experiments could be combined with X-ray synchrotron characterization to link structural evolution with the corresponding stimulus over time.

The ease of rapidly altering concentrations and temperatures in microfluidic devices could be used to overcome thermodynamic restrictions via concentration or kinetic control. The growth of core-shell particles is limited by the lattice mismatch between different materials, although studies have shown that making graded shells allows the growth of high core-shell heterostructures that normally feature excessive strain.[33] Finely tuned chemical gradients in microfluidic devices could be used to produce even more highly strained shells and shells of alternating compositions. Rapid thermal or concentration jumps could theoretically trap particles into thermodynamically unfavorable heterostructures. Other studies have shown that the identity of materials and their order of growth in multi-component materials determine the branching morphology of the heterostructures.[34] The thermal, temporal, positional, and concentration control of microfluidic devices could be used to investigate ways to overcome these rules and branch traditionally linear structures or elongate typically isotropic structures.

9.6 CONCLUSION

This dissertation has discussed the progress of nanocrystal microreactor research from its nascent roots to its current state of broad opportunity. The process of solving the initial challenges of reacting nanoparticles in confined channels has revealed not only the limitations of current microreactors, but also the technologies that still need to be developed and the specific research questions that nanoparticle microreactors can best address. For

example, the modification and characterization of existing nanoparticles in microfluidic devices, rather than pyrolytic synthesis, may ultimately be more useful and enlightening to nanocrystal research due to its relative lack of restrictions and wealth of promising applications. Whatever reactions these devices are used for, microfluidic reactors will be best served as a compliment to flask syntheses, since solving problems in nanoscience is a multidisciplinary approach that requires many different techniques. Microfluidic reactors have specific advantages that, in concert with off-chip techniques, will be used to shed light on questions that currently escape the capabilities of current macroscale technology. The continued development and creative application of microfluidic reactors will lead to new insight that will benefit nanoscale reactions in all fluid size regimes.

9.7 REFERENCES

(1) Wagner, J.; Kohler, J. M. *Nano Lett.* **2005**, *5*, 685.

(2) Boleininger, J.; Kurz, A.; Reuss, V.; Sonnichsen, C. *Phys. Chem. Chem. Phys.* **2006**, *8*, 3824.

(3) Xue, Z. L.; Terepka, A. D.; Hong, Y. *Nano Lett.* **2004**, *4*, 2227.

(4) Song, Y. J.; Modrow, H.; Henry, L. L.; Saw, C. K.; Doomes, E. E.; Palshin, V.; Hormes, J.; Kumar, C. *Chem. Mater.* **2006**, *18*, 2817.

(5) Song, Y. J.; Kumar, C.; Hormes, J. *J. Nanosci. Nanotechnol.* **2004**, *4*, 788.

(6) Song, Y. J.; Doomes, E. E.; Prindle, J.; Tittsworth, R.; Hormes, J.; Kumar, C. *J. Phys. Chem. B* **2005**, *109*, 9330.

(7) Sue, K.; Kimura, K.; Arai, K. *Mater. Lett.* **2004**, *58*, 3229.

(8) Park, K. Y.; Ullmann, M.; Suh, Y. J.; Friedlander, S. K. *J. Nanopart. Res.* **2001**, *3*, 309.

(9) Wang, H. Z.; Nakamura, H.; Uehara, M.; Miyazaki, M.; Maeda, H. *Chem. Commun.* **2002**, 1462.

(10) Takagi, M.; Maki, T.; Miyahara, M.; Mae, K. *Chem. Eng. J.* **2004**, *101*, 269.

(11) Khan, S. A.; Gunther, A.; Schmidt, M. A.; Jensen, K. F. *Langmuir* **2004**, *20*, 8604.

(12) Edel, J. B.; Fortt, R.; deMello, J. C.; deMello, A. J. *Chem. Commun.* **2002**, 1136.

(13) Shestopalov, I.; Tice, J. D.; Ismagilov, R. F. *Lab Chip* **2004**, *4*, 316.

(14) Hung, L. H.; Choi, K. M.; Tseng, W. Y.; Tan, Y. C.; Shea, K. J.; Lee, A. P. *Lab Chip* **2006**, *6*, 174.

(15) Nakamura, H.; Yamaguchi, Y.; Miyazaki, M.; Maeda, H.; Uehara, M.; Mulvaney, P. *Chem. Commun.* **2002**, 2844.

(16) Chan, E. M.; Mathies, R. A.; Alivisatos, A. P. *Nano Lett.* **2003**, *3*, 199.

(17) Yen, B. K. H.; Stott, N. E.; Jensen, K. F.; Bawendi, M. G. *Adv. Mater.* **2003**, *15*, 1858.

(18) Nakamura, H.; Tashiro, A.; Yamaguchi, Y.; Miyazaki, M.; Watari, T.; Shimizu, H.; Maeda, H. *Lab Chip* **2004**, *4*, 237.

(19) Krishnadasan, S.; Tovilla, J.; Vilar, R.; deMello, A. J.; deMello, J. C. *J. Mater. Chem.* **2004**, *14*, 2655.

(20) Chan, E. M.; Alivisatos, A. P.; Mathies, R. A. *J. Am. Chem. Soc.* **2005**, *127*, 13854.

(21) Yen, B. K. H.; Gunther, A.; Schmidt, M. A.; Jensen, K. F.; Bawendi, M. G. *Angew. Chem. Int. Ed.* **2005**, *44*, 5447.

(22) Wang, H. Z.; Li, X. Y.; Uehara, M.; Yamaguchi, Y.; Nakamura, H.; Miyazaki, M. P.; Shimizu, H.; Maeda, H. *Chem. Commun.* **2004**, 48.

(23) Wang, H. Z.; Nakamura, H.; Uehara, M.; Yamaguchi, Y.; Miyazaki, M.; Maeda, H. *Adv. Funct. Mater.* **2005**, *15*, 603.

(24) *Nature* **2005**, *437*, 792.

(25) deMello, A. J. *Nature* **2006**, *442*, 394.

(26) Zubritsky, E. *Anal. Chem.* **2004**, *76*, 12A.

(27) deMello, J.; deMello, A. *Lab Chip* **2004**, *4*, 11N.

(28) deMello, A. J. *Lab Chip* **2005**, *5*, 1199.

(29) Paegel, B. M.; Yeung, S. H. I.; Mathies, R. A. *Anal. Chem.* **2002**, *74*, 5092.

(30) Huang, L. R.; Cox, E. C.; Austin, R. H.; Sturm, J. C. *Science* **2004**, *304*, 987.

(31) Hibara, A.; Nonaka, M.; Hisamoto, H.; Uchiyama, K.; Kikutani, Y.; Tokeshi, M.; Kitamori, T. *Anal. Chem.* **2002**, *74*, 1724.

(32) Lee, L. P.; Berger, S. A.; Liepmann, D.; Pruitt, L. *Sens. Actuators A-Phys.* **1998**, *71*, 144.

(33) Manna, L.; Scher, E. C.; Li, L. S.; Alivisatos, A. P. *J. Am. Chem. Soc.* **2002**, *124*, 7136.

(34) Milliron, D. J.; Hughes, S. M.; Cui, Y.; Manna, L.; Li, J. B.; Wang, L. W.; Alivisatos, A. P. *Nature* **2004**, *430*, 190.